PARTICULATE COMPOSITE MATERIAL INTERNAL DEFORMATION MEASUREMENTS USING X-RAY MICROTOMOGRAPHY AND DIGITAL VOLUME CORRELATION

BY

MANUE MARTINEZ

THESIS

Submitted in partial fulfillment of the requirements
for the degree of Master of Science in Aerospace Engineering
in the Graduate College of the
University of Illinois at Urbana Champaign, 2017

Urbana, Illinois

Advisor:

Professor John Lambros

ABSTRACT

Typical particulate composites used in engineering applications consist of complex microstructures with a range of particulate sizes and often high particulate volume fractions (65%-95%). Examples of these are, explosives and rocket propellants for defense and aerospace applications, asphalt concrete materials civil engineering applications and ceramic/ceramic thermal barrier coatings for turbine engines. In the past, X-ray microtomography (X-ray microCT) has been used to study the internal structure of such complex microstructures. The combination of the Digital Volume Correlation (DVC) method and the three-dimensional (3D) imaging X-ray microCT technique is becoming a powerful tool in the mechanics community that provides 3D internal metrology in addition to 3D imaging.

In this work, we employ an in-house DVC algorithm to measure deformations within a model composite material – a controlled number of one or a small finite number hard particles in a complaint polymer matrix. *In-situ* compression experiments are performed inside an X-ray microCT scanner on samples containing different microstructure configurations. To quantitatively and qualitatively study the internal deformations and evolution of failure in 3D, we use a model composite material (cylindrical 15 mm in height and 10 mm in diameter) with a series of different well-controlled microstructure configurations. A simple microstructure arrangement consisted of precisely positioned spherical ceramic inclusion(s) (at most two). A more complex microstructure contained a larger number (20) of randomly positioned spherical alumina inclusions. The final configuration studied contained a precisely positioned irregularly shaped inclusion. The model material consisted of a reinforced polymer matrix, PDMS with 35 μm glass marker particles which were appropriately distributed to serve as the internal speckle pattern required for DVC.

Specifically, we studied the 3D displacement and strain fields resulting within the polymer particulate composites with different microstructure arrangements. In addition, we resolved the resolution and accuracy of the DVC analysis technique by successfully comparing the measured results to known elastic solutions (before the occurrence of failure). The second part of this work focused on studying internal flaws and failure evolution as a function of loading. Interfacial debonding was the only failure mode seen in these model composites and was studied quantitatively and qualitatively for the simpler microstructure configurations of a single embedded spherical inclusion or two inclusions one above each other. We also attempted to delay interfacial failure by increasing the surface roughness of a single alumina inclusion sample. Although, in the simpler case of the single and double inclusions the opening(s) was precisely measured, in the more complex interfacial failure patterns of the multiple spheres or the irregularly shaped inclusions, debonding was only qualitatively studied using volumetric 3D renderings.

To my family,

ACKNOWLEDGEMENTS

I would like to thank my advisor Professor John Lambros for his guidance, support and granting me the opportunity to conduct research with him. Our research group: Robert Waymel, Renato Bichara Vieira, David Foering and Arthur Ding for our interesting lunch conversations. Leilei Yin at the Beckman institute for his assistance in using the 3D imaging equipment in the microscopy suite. Dr. Mark Gates for developing the 3D algorithm. Finally, Dr. Joe Gonzalez for his mentoring and with initially helping me with the 3D analysis techniques and methods used in this work. I am deeply indebted to my family, friends and mentors who have encouraged me through my studies.

TABLE OF CONTENTS

CHAPTER 1: INTRODUCTION

1.1 BACKGROUND

The two-dimensional digital image correlation (2D-DIC) technique has been used over the past 35 years to obtain in-plane displacement and strain surface measurements in materials and structures for a variety of applications (Sutton et al. 1983, Chu et al. 1985, Bruck et al. 1989). In recent years, an internal 3D measurement extension of the 2D-DIC technique called digital volume correlation (DVC) has been gaining more exposure in various studies of materials (Bay et al. 1999, Liu et al. 2007, Lenoir et al.2007, Roux et al. 2008, Frank et al. 2007, Jiroušek et al. 2011). The integration of DVC with X-ray microcomputed tomography (microCT) allows the measurement of full *internal* 3D displacement and strain fields throughout the interior of a material while under deformation. Like DIC, in DVC the material of interest must possess an internal random "speckle" pattern of features detectable by the imaging equipment. The internal pattern can either be naturally existing in the material, e.g., bone (Bay et al. 1999, Liu et al. 2007) and foam (Roux et al. 2008), or be embedded during manufacturing (Frank et al. 2007). The DVC technique was first introduced by Bay et al. (1999) in a study resolving the 3D displacement and strain fields throughout the interior of a trabecular bone sample under compression. Bay et al. (1999) used only three translational degrees-of-freedom (DOF) *u, v, w* only to correlate the internal images before and after loading obtained by microCT of the bone sample. They computed 5,500 correlation points in 7 seconds for each 61^3 volumetric subset in a 580 x 580 x 520 voxel image. Since then, DVC has emerged as a technique to measure internal displacement fields on materials with complex microstructure such as bone, foam, rock, polymers, metals, etc. These complex-microstructure materials all inherit natural internal

patterns precisely because of their microstructure allowing DVC to be used. However, it is clear that DVC forms a powerful experimental tool that for the first time can non-destructively provide internal 3D deformation measurements of deforming solids thus overcoming a significant limitation of experimental mechanics' full-field metrology that was generally limited to surface measurements prior to the advent of DVC. Note that DVC has also been successfully used with other 3D imaging techniques such as confocal microscopy (e.g., Frank et al. 2007). More details on the DVC method are discussed in Chapter 2.

1.2 Motivation and Objectives

With complex microstructure materials being increasingly used, it is vital to gain an understanding of microstructural effects on their mechanical response, which at the microstructural level has been seen to be highly inhomogeneous. One such category of material where local mechanical inhomogeneity can be instrumental in determining overall response are particulate composites. Particulate composites are widely used in a number of applications such as composite-composite coatings for aerospace alloy turbine components, asphalt concrete for infrastructure applications, and highly energetic materials, which can either be used destructively (e.g., explosives in mining, defense, etc.) or constructively (e.g., solid rocket propellants). These polymeric particle-reinforced composites (e.g., asphalt, propellants and explosives) commonly consist of high volume fractions (65%-95% particles) with hard particles in a compliant matrix. We begin here by investigating the strain concentration around a simple microstructural configuration (a single inclusion) and then move to more complicated configurations. While imaging, we isolate the microstructural features of hard ceramic particles in a soft matrix and measure the deformation in 3D under uniaxial compressive loading using DVC. To do this we used a "model" particulate composites rather than actual ones so that we can employ DVC.

An in-house DVC algorithm developed by Gates *et al*. (2011) is used to capture the internal deformations within a particulate polymer matrix composite (PPMC) under loading. *In-situ* compression experiments are performed in an X-ray microCT for different microstructure configurations of the hard particle(s) in a soft matrix. In order to track the deformations, a speckle pattern is embedded during the manufacturing process of the composites. At a 4x magnification, the optimal pattern to use with the tomographic equipment at the Beckman Institute consisted of 35 μm silica glass (SiO_2) beads (Comco Inc.) as marker particles with 15%vol. (35μm-15%vol.), in a reinforced elastomer matrix. The optimal pattern was determined through a parametric study of different percent volume and sizes of the embedded particles, which determined the combination that resulted in the best resolution when integrating X-ray tomography with DVC (Gonzalez and Lambros 2016. The steps for manufacturing the polymer reinforced composite (i.e., PDMS with 15% vol. SiO_2 35μm marker particles) with and without inclusions is described in Chapter 2.

The work presented here aims to characterize the deformations and failure evolution in a PPMC with a microstructural configuration involving one or a small number of hard particles (alumina or rock) in a soft (PDMS) matrix in several configurations which we term: single inclusion (SI), double inclusion (DI), randomly distributed inclusions (RDI), rounded irregular inclusion (RII) and vertical irregular inclusion (VII)). The simpler configurations are the SI and DI, while the more complex ones are the RDI, RII and VII. The specific objectives of the effort are the following:

- Demonstrate the feasibility of using DVC in situ in a polymer matrix particle composite system under loading

- Experimentally resolve the resolution and validate the accuracy of the DVC analysis technique by comparing the measured results to known solutions.
- Study the strain development resulting within a polymer particulate composite with different microstructure configurations.
- Investigate both qualitatively and quantitatively the particle debonding failure in 3D.

1.3 Overview of the Document

To address the question mentioned in the previous section, Chapter 2 of this thesis starts by detailing the experimental set up and techniques used in the *in-situ* loading, polymer particulate composite manufacturing and imaging. Moreover, the X-ray microCT scanning and reconstruction procedure is covered there. The image data sets were analyzed, using ImageJ and Amira, and imported into MATLAB. Chapter 3 discusses the preprocessing done on the image data sets (such as removing rigid body motion via affine transformation, cropping, file conversion, etc.), the creation of custom correlation grids for various microstructural configurations, the DVC-measured deformation within a polymer composite, and the two-dimensional qualitative perspective of failure, i.e., particle debonding. Chapter 4 first validates the accuracy of the DVC method by comparing measured deformations around a single alumina inclusion in a finite medium with the analytical solution, formulated by Gooder (1933), which describes the displacement field around a rigid inclusion within an infinite medium under uniaxial tension. In addition, Chapter 4 quantitatively and qualitatively presents results for evolution of the debonded region around one (SI) and two inclusion (SI) relative to the applied strain. In contrast, the more complex failure responses exhibited in the RDI, RII and VII,

samples were only qualitatively visualized and analyzed. Chapter 5 provides a summary of the major conclusions of the effort and suggests directions for future research.

CHAPTER 2: EXPERIMENTAL TECHNIQUES

2.1 PARTICULATE COMPOSITE MANUFACTURING

A composite material consists of a reinforcement phase (*e.g* fibers, particulates etc.), a matrix phase (*e.g* metal, polymer or ceramic matrix), and on many occasions an interphase region that typically forms between the two depending on the manufacturing process and the individual components. If the *interphase* length scale is much smaller than the reinforcement size, then the connection between reinforcement and matrix can be thought of as an *interface* having negligible thickness. However, even though of negligible thickness, an interface can still have a distinct mechanical response which would consequently need to be independently studied. Particulate composites consist of particles of various sizes and shapes either randomly or orderly dispersed within the matrix. When distributed randomly, the spatial randomness of the particle distribution allows these composites to be regarded as quasi-homogeneous and quasi-isotropic on a length scale much larger than the particle size and spacing. PPMCs offer advantages of being inexpensive and easy to process and having low density, despite their lower strength and stiffness when compared to metals of ceramics. PPMCs can be tailored to form thermoset, thermoplastic or elastomer composites. Elastomers are a class of polymers that have some degree of cross linking and can recover large strains. An example of an elastomer used in industry is nanoparticle reinforced rubber used in all commercial tires.

2.1.1 POLYMER MATRIX WITH MARKER PARTICLES

In the present work, which concentrates on model PPMCs, the composite samples were based on a commonly used polymer, Polydimethylsiloxane (PDMS), with embedded marker

particles for the purposes of DVC. PDMS preparation was done using the Sylgard 184 silicone elastomer kit. The combination of PDMS and 35 μm silica glass beads (Comco Inc.) created the base model composite sample used for DVC studies. Gonzalez and Lambros (2016) conducted a parametric study of different percent volume and sizes of the embedded particles to determine which combination resulted in the best resolution when used in X-ray tomography and DVC. The parametric study investigated the best internal material patters applicable to the DVC method at different resolution and length scales. They concluded the following; when using 10x magnification resulting in a resolution 2 μm/voxel or less, 5 μm marker particles making up 10%vol of the sample should be used. When using a 4x magnification, resolution of 4μm/voxel, it is best to use 35μm marker particles consisting of 15% vol. For the 0.5x magnification, 10μm/voxel resolution, the best marker particles size is 50 μm where the particles consist of 20%vol. Hence, they found that the best pattern for use with the tomographic equipment at the Beckman Institute (which will also be used in this work) consisted of 35 μm SiO_2 marker particles with 15%vol. (35μm-15%vol.) in a PDMS matrix. The same composition of the base PPMC material will therefore also be followed throughout in this study.

The steps for manufacturing the polymer reinforced composite (i.e., PDMS with 15% vol. SiO_2 35μm marker particles) are shown in **Figure 2.1**. The PDMS 700-800 cSt viscosity base and the linker, PDMS (PSI-021) were added, at a 10:1, to a plastic container and measured, followed by the appropriate mass of silica beads to achieve 15% vol, that was determined by the expression below,

$$m_{particles} = \left(\frac{P_{vol}}{100} * \frac{m_{linker} + m_{base}}{\rho_{matrix}}\right) * \left[\frac{1}{\rho_{particles}} * \left(1 - \frac{P_{vol}}{100}\right)\right]^{-1}, \qquad (2.1)$$

$$m_{linker} = \frac{m_{base}}{10}, \tag{2.2}$$

where $m_{particles}$, is the mass of the particles, P_{vol}, is the percent volume, m_{base}, is the mass of the base, m_{linker}, is the mass of the linker, $\rho_{particles}$, is the density of the particles and ρ_{matrix}, is the density of the matrix (step 1). Then, the base, linker and beads were mixed (step 2) and placed in a vacuum for 20 minutes to eliminate any air bubbles (step 3). Prior to pouring the samples into an aluminum mold (step 4), lubricant (WD40) was applied around the walls to ease the process of extracting the composites. Once the mixture was degassed, it was slowly poured into the mold and placed in a convection oven at 150°C for 15 minutes (step 5). The mold was then placed in the refrigerator to cool down for 15 minutes. Finally, the bottom plate was removed and the samples were individually released. The end result was a uniform PDMS reinforced composite sample with 15% vol. of silica beads (PDMS35μm15%vol.). In order to study responses that arise from different microstructure configurations, a macro-size inclusion was precisely placed at the center of the cylindrical polymer composite, the PDMS cylinder with marker particles being shown in **Figure 2.2**. The procedure of positioning an inclusion is detailed below.

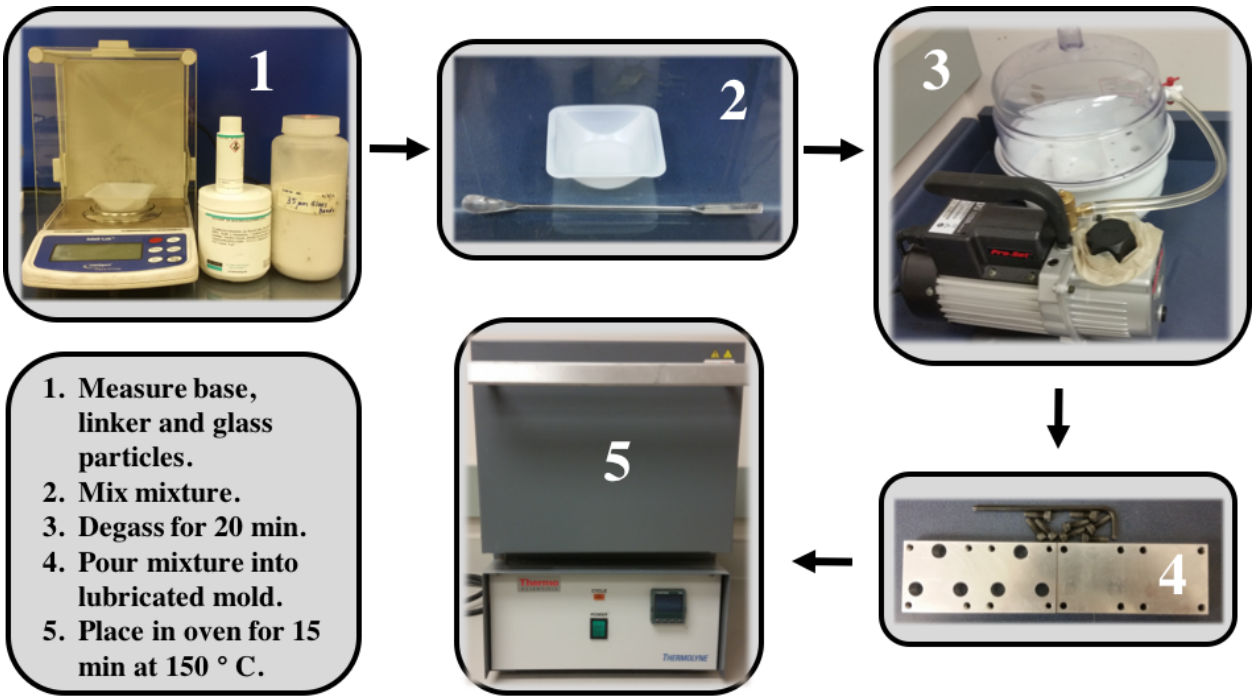

Figure 2.1 Polymer reinforced composite manufacturing process. First the base, linker and marker particles are measured (1) and mixed (2). Next, the mixtures are degassed (3), placed into the aluminum mold (4) and cured in a convection oven (5).

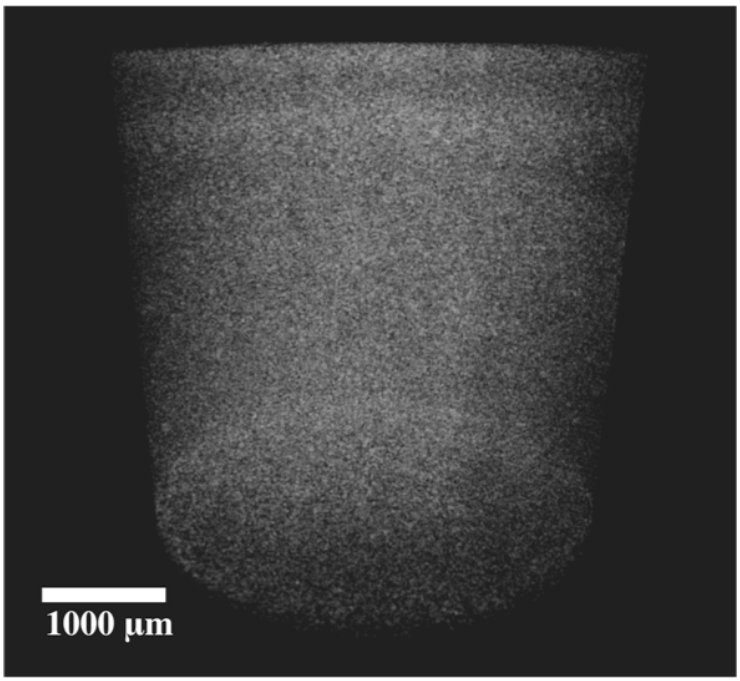

Figure 2.2 Volume rendering of PDMS reinforced composite. The reinforced polymer composite is manufactured by the process detailed above.

2.1.2 Microstructure Configurations: Single, Double, Randomly Distributed, Irregular

To qualitatively and quantitatively investigate the resultant internal deformations under loading within the model material with different microstructure configurations, different types of PPMCs were manufactured. Note, the microstructural reinforcements (consisting either of alumina ceramic beads or small rocks) had macro-size features since they must be at least an order of magnitude larger than the DVC marker particles embedded in the matrix for metrology purposes (although the marker particles themselves also provide reinforcement to the matrix). Hence, inclusions with length scales of 500 μm and larger are used. A simple microstructure was introduced by precisely positioning one or two alumina inclusions at given locations. A more complex microstructure was developed by increasing the number of ceramic beads or by precisely positioning single, but irregularly shaped, inclusions. The single inclusion (SI) composite was made starting from PDMS with embedded markers prepared following the aforementioned procedure. The appropriate amount of marker particles to maintain the 15% vol. once the inclusion had been added was determined by the following,

$$m_{particles} = \left(\frac{\rho_{particles}}{1 - \frac{P_{vol}}{100}}\right) * \left(\frac{P_{vol}}{100}\right) * \left(\frac{m_{linker} + m_{base}}{\rho_{matrix}} + \frac{m_{inclusion}}{\rho_{inclusion}}\right), \qquad (2.3)$$

where $\rho_{inclusion}$ is the density of the inclusion, and $m_{inclusion}$ is the mass of the inclusion. Samples were mixed in the appropriate proportions, degassed for 20 min, poured in a mold, and cured in the oven at 150 °C for 15 min. The initial mixture was poured into the aluminum mold to produce cylindrical samples 10 mm in diameter and 10 mm in height. After curing, the cylindrical sample (PDMS with markers) was removed, placed in a cylindrical sample holder, and cut at the ~7.5 mm height mark, using a sharp razor blade. The sample holder, designed

specifically for the cutting process, along with a sample is shown in **Figure 2.3**. After cleaning and lubricating the walls of the mold, the cut material was placed back into the mold, and a single alumina spherical inclusion with a diameter (D) of 1 mm was placed onto the surface of the cured half-cylinder, while being held in place with a glass microtube with a diameter of 0.25 mm and length of 20 mm. With the tube still in place, additional mixture of PDMS with marker particles was then added to fill up the mold to a total height of 15 mm, after which the microtube was slowly removed. Lastly, the same curing process was followed for another 15 min and the final result was a 10 mm diameter 15 mm long cylinder with a 1 mm diameter alumina spherical inclusion embedded in the center with 35μm-15%vol marker particles surrounding it.

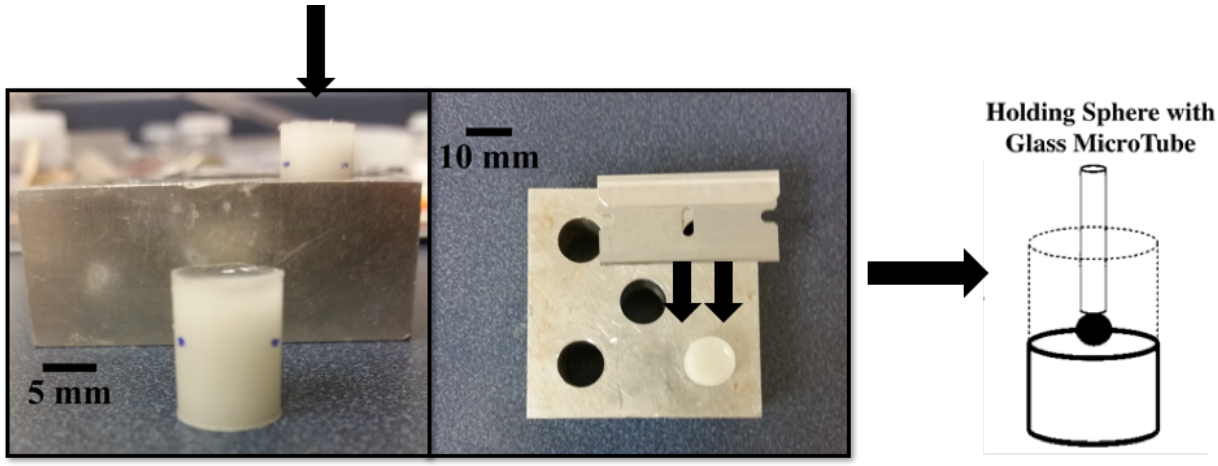

Figure 2.3 Sample holder (left), cutting process (middle) and inclusion placement (right). The reinforced elastomer is inserted into the sample holder, until the marking is covered (left). Next, a razor blade is used to cut the cylindrical specimen (middle). A small glass tube is used to precisely position one alumina inclusion (right).

The microtube served as an important tool to ensure the alumina sphere remained near the center of the cylindrical sample after curing. Without this microtube approach it would be very difficult to control the precise positioning of the alumina inclusions. A 2D radiograph, shown in **Figure 2.4 (a)**, was obtained from an X-ray microCT machine as discussed the proceeding section. The dark dots around the black sphere represent the embedded markers used

to track deformation through DVC. Note a boundary line, indicated by red arrows in **Figure 2.4 (a)** and **(d)**, developed from the two-step curing process. The internal pattern remained visually unaffected and baseline experiments with no inclusion showed no effect of the two-step cure on either DVC (since DVC correlations use horizontal slices) or the material response. The 2D radiographs were processed and analyzed to obtain a volume rendering of the data. Now the *white* speckle pattern visible in the figure below are the embedded marker particles, while the remaining light gray volume is the PDMS matrix, **Figure 2.4 (b)**. A transparent volume rendered image is shown in **Figure 2.4 (c)**, with one cross-sectional slice (*x*-*y* plane). This is especially important for the double inclusion samples described below.

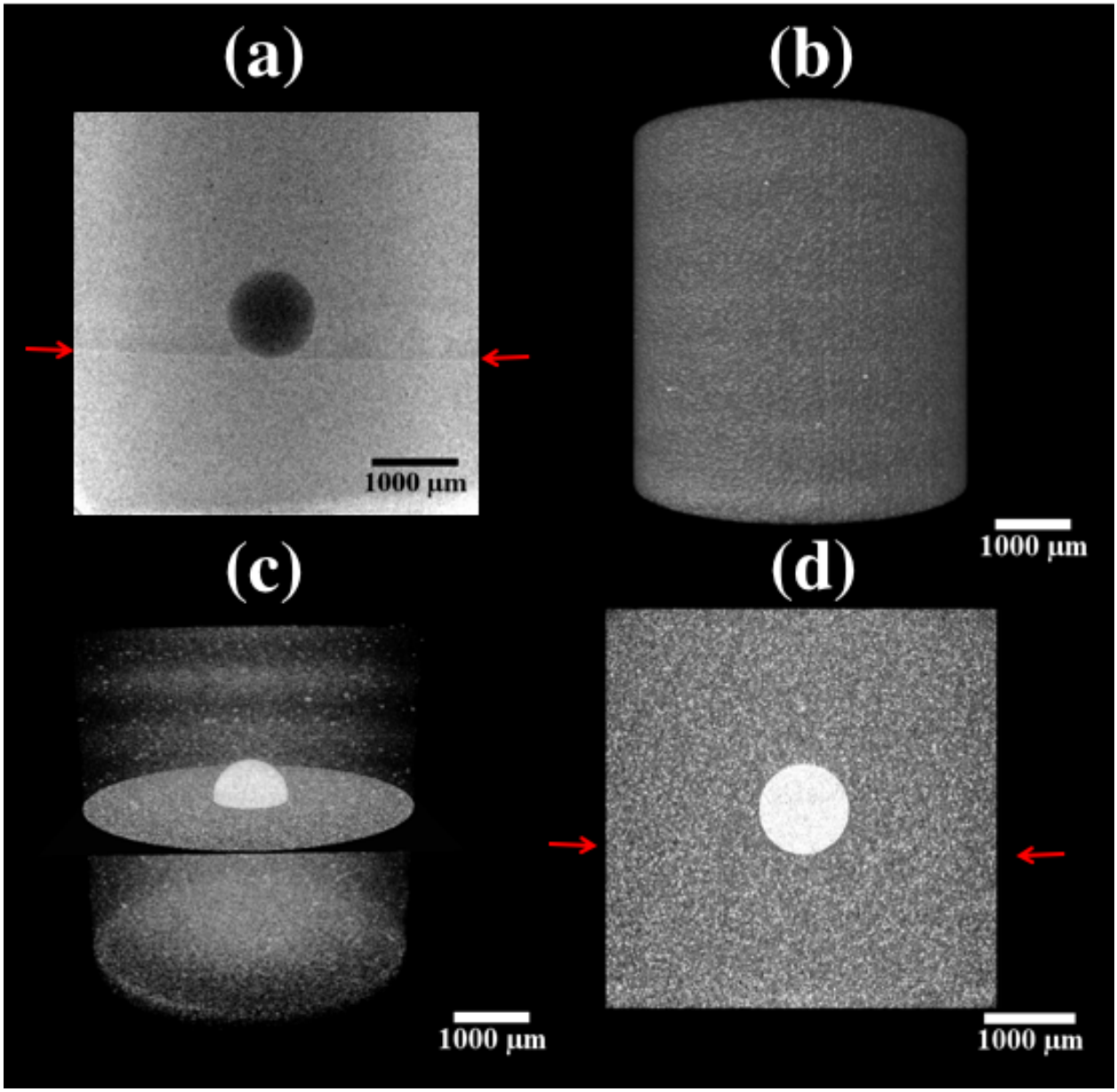

Figure 2.4 Single inclusion (SI) composite illustrated as **(a)** 2D radiograph, **(b)** volume rendered image of entire scanned volume, **(c)** partially transparent volume rendered image with cross-sectional slice (*x-y* plane) and **(d)** 2D slice in *x-z* plane. Red arrows show the boundary line from the two-step curing process. The inclusion, with a 1.0 mm diameter, was held in place before cure with a glass microtube.

In order to study, the interaction between two macro-sized particulates, two alumina spheres where placed at a desired distance apart. The manufacturing process for a single inclusion (SI) was repeated twice, to construct a double inclusion (DI) specimen. After preparing

a single inclusion specimen as described above and allowing it cool to room temperature, it was then cut above the first incision at a desired distance (typically ~2D-3D) and placed back into the mold and a second inclusion was added in the same fashion. In the case shown in **Figure 2.5 (a)** the equatorial planes of the two inclusions were approximately ~2.27 mm (~2.27D) apart. Notice there are now two boundary lines, which are indicated by red arrows in **(a)** and **(d)**. The two boundary lines resulted from the three-step curing process. Prior to inserting the cut SI, the walls of the aluminum mold were lubricated again. Like before, an alumina inclusion was then placed and held with a glass microtube on the surface and then the remaining half of the sample cured on top. The manufacturing process detailed above gives an illustration of how to make polymer composites with precisely positioned inclusions. However, this method of embedding a microstructure becomes difficult to scale up if we want to increase the number of spherical inclusion in the microstructure. A different curing process is described below which enables us to randomly disperse a finite number of inclusions within the cylindrical polymer matrix, albeit with far less control of their final position.

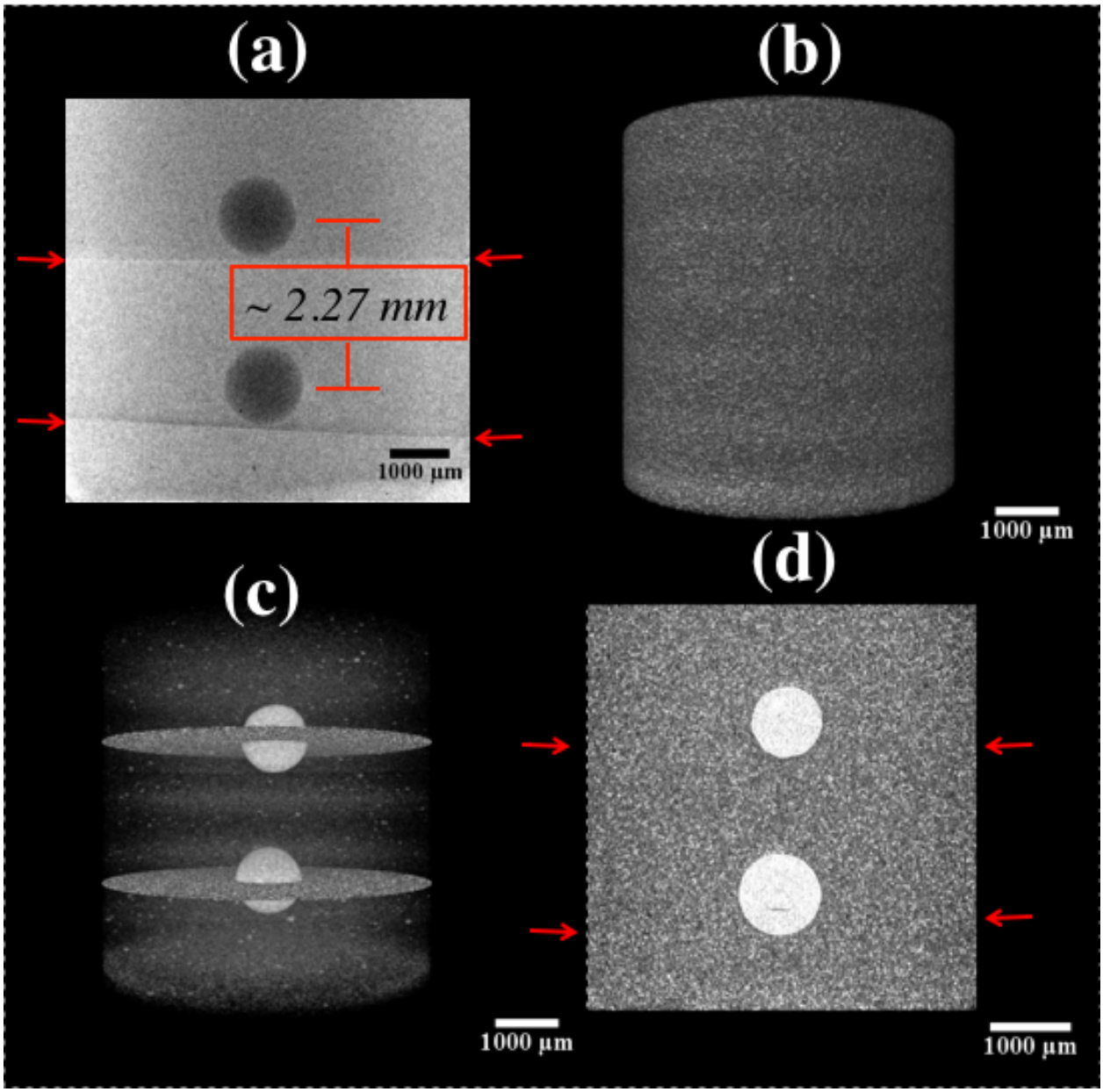

Figure 2.5 Double inclusion (DI) composite demonstrated as **(a)** 2D radiograph, **(b)** volume rendered image of entire scanned volume, **(c)** partial transparent volume rendered image with cross-sectional slice (*x-y* plane) and **(d)** 2D slice in *x-z* plane. Red arrows show the boundary lines from the three-step curing process. Both inclusion are 1.0 mm in diameter and their centers are ~2.27 mm apart.

Manufacturing a polymer composite with more than two randomly distributed inclusions (RDI) was performed using either a "Hot Plate Technique" or a resin transfer molding technique, the latter being similar to the technique used for the SI and DI samples. The difference between

the Hot Plate Technique and the aforementioned procedure is that samples were cured on a hot plate as oppose to in a convection oven. Curing on the hot plate was done to get the PDMS with marker particles mixture in a solid but still viscous state. If the mixture were too viscous (i.e., almost solidified) the inclusion would sit on the top surface; if it were not viscous enough the inclusion would quickly settle to the bottom. The appropriate state of viscosity was found by trial and error. Similar to before, samples were mixed at appropriate proportions, degassed for 20 min, poured into the lubricated aluminum mold and then placed on a hot plate at 150 °C for ~6 ½ min. The mold was then removed from the hot plate; placed aside, and alumina inclusions were either dropped or gently placed on the top surface. The addition of inclusions had to be done within at most 2 ½ min (after 2 ½ min the top surface would solidify and not allow the inclusion to sink). After the placement of inclusions, the mold was placed back on the hot plate for an additional 8 ½ min to complete curing, and cooled in the refrigerator for 15 min. The product was a 10 mm diameter 15 mm long cylinder with a random distribution of alumina inclusions, shown in **Figure 2.6 (a)**, in this case illustrating 20 alumina inclusions of 0.5 mm diameter each. The darker regions signify high absorption and material density. The red dashed box represents the scanned area using 4x magnification lens. The different curing process, used to construct a polymer composite with randomly distributed inclusions (RDI), resulted in a more compliant material response, in contrast to SI and DI. The material behavior of a reinforced elastomer with and without an alumina inclusion are presented in the next section.

The irregular inclusion samples were constructed using the SI procedure described earlier. Instead of embedded spherical beads, a single granular macro-sized rock material was precisely positioned at the center of the reinforced elastomer. In this case, a rounded irregular inclusion (RII) and a vertical irregular inclusion (VII) which are shown in **Figure 2.6 (b)** and (**c**),

respectively. Notice the boundary line in RII and VII from the two-step curing process. Lastly, to compensate for the size of the vertical inclusion, the PDMS with marker particles was cut below the center around ~5 mm as opposed to the center i.e., 7.5 mm.

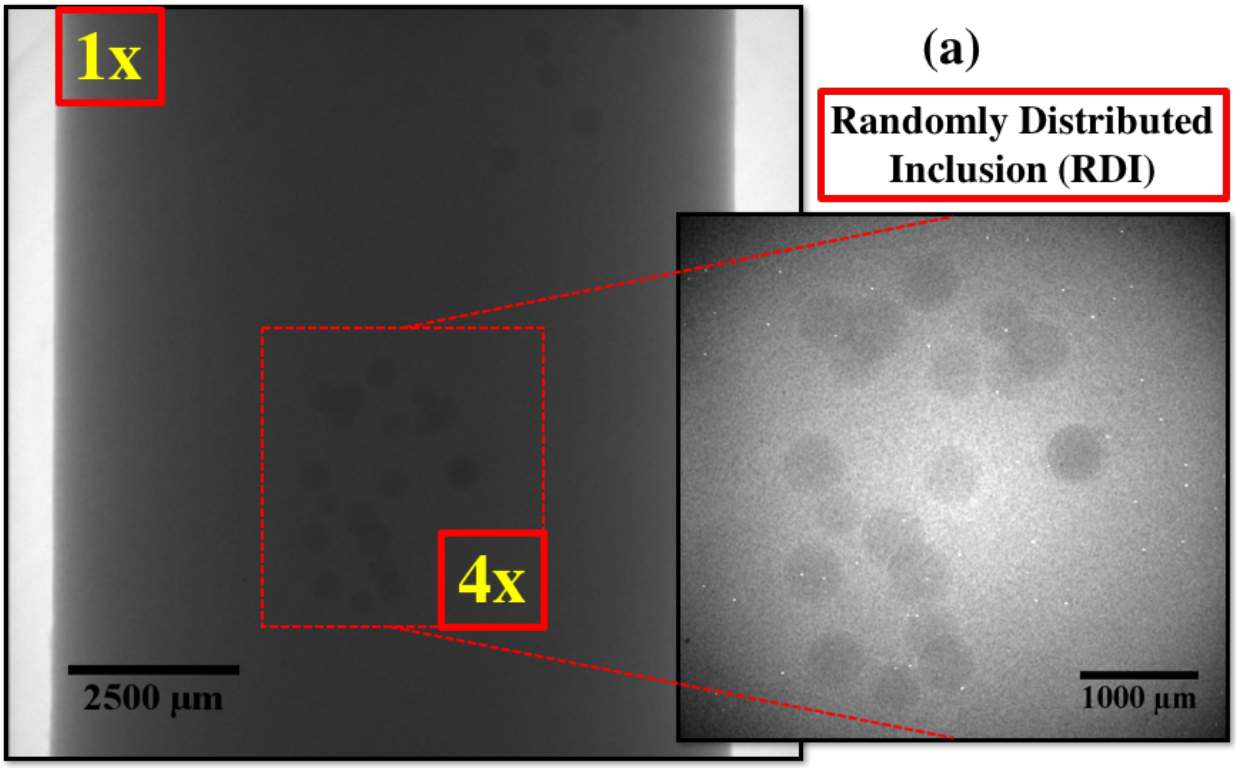

Figure 2.6 Complex microstructure configurations shown as 2D radiographs with 1x magnification. A random distribution of 20 inclusions is shown in a 4x radiograph (**a**). A volume rendering, from a 4x scan, of a rounded irregular inclusion (**b**) and a vertical irregular inclusion (**c**) are shown in *VolrenGlow* and *Temperature* colormap, respectively.

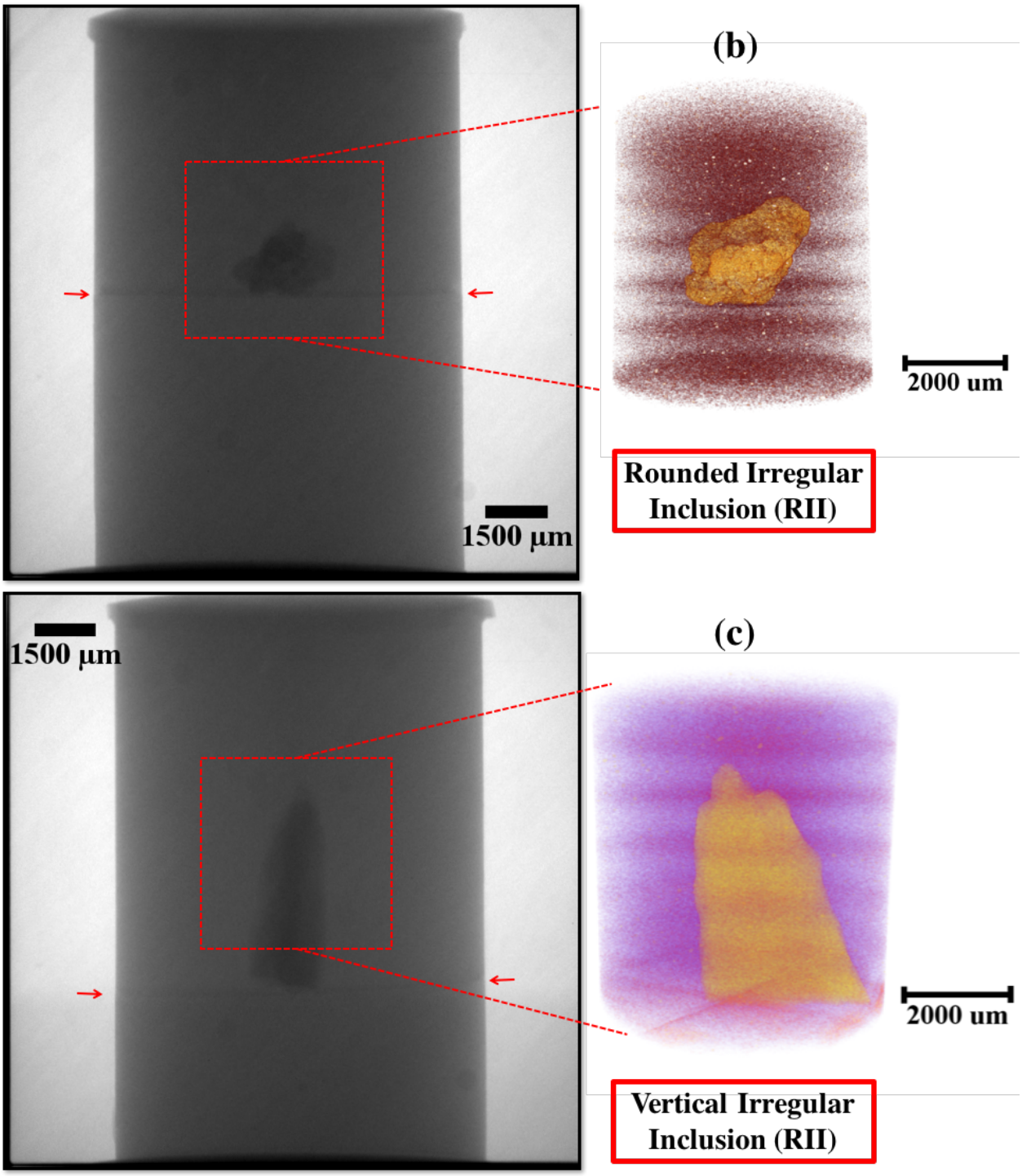

Figure 2.6 (cont.)

2.1.3 Altering Interfacial Properties

The interface acts to connect the reinforcement and matrix phases, and transmits mechanical information from one to the other. Despite the small length scale of the interface (or interphase) relative to the reinforcement and matrix, many mechanical problems can arise at the interface, such as delamination, damage, and debonding. The quality of the interface directly affects a composite's failure and mechanical properties. The methodology described above embedded the as-received alumina spheres into the PDMS and marker particle matrix resulting in a specific set of interfacial mechanical and failure properties. In this study, in order to enhance the interfacial properties beyond those produced by the bond of PDMS with the as-received alumina sphere we used a mechanical approach. To alter the interfacial properties the surface of an as-received alumina inclusion, with a diameter of 1mm, was roughened using a 180-grid sandpaper. The procedure for roughening the surface, which necessitated the in-house design of a polishing jig, is illustrated in **Figure 2.7**.

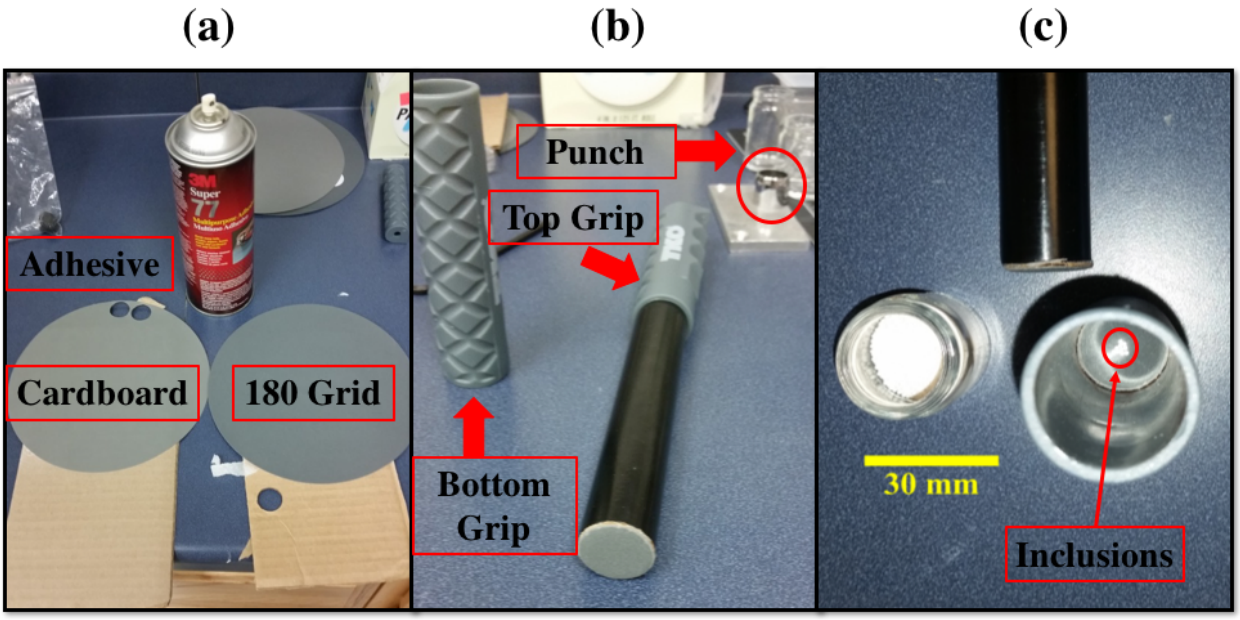

Figure 2.7 Surface roughening technique outline: **(a)** 180-grid sandpaper was attached to a piece of cardboard by spraying both surfaces with 3M 77 Adhesive spray, **(b)** circular punch (circled in red) was used to cut circular cardboard and sandpaper pads and **(c)** a sand pad were then glued to

Figure 2.7 (cont.) the tube. An as-received alumina spheres were then dropped into the bottom grip, and then the tube was slowly inserted. Bottom grip remains stationary while the top grip was used to apply a manual torque.

First, the 180-grid sandpaper was attached to a piece of cardboard by spraying both surfaces with 3M 77 Adhesive spray, the materials are shown in **Figure 2.7 (a)**. Next, a circular punch (circled in red in **Figure 2.7 (b)**) was used to cut circular cardboard and sandpaper pads, approximately 25 mm in diameter. Two cardboard pads and one sandpaper pad were then inserted into the bottom grip of the holder device. Another sandpaper pad was then glued, using the same adhesion spray as before, to the tube. An as-received alumina sphere was then dropped into the bottom grip, as shown in **Figure 2.7 (c)**, and then the tube was slowly inserted. The top grip was finally placed on the tube and then a manual torque was applied, while keeping the bottom grip stationary. The circular motion was performed for 1 ½ min and then the inclusion was extracted. A confocal microscope was used to obtain the surface profile of both an as-received alumina sphere and a roughened sphere. The resulting texture maps from a 20x scan, are shown in **Figure 2.8 (a)** and **(b)**, clearly illustrates the variations on the surface among an as-received and the roughened surface. **Figure 2.8 (c)**, shows the roughness profile along the surface of both cases. The curves convey that the roughened inclusion is approximately two times rougher than the as-received inclusion. The roughened inclusion (gray) and as-received (orange) have a maximum surface roughness of ~43 μm and ~25 μm, respectively. Chapters 3 and 4 compare the resultant deformations and failure evolution from each circumstance, respectively.

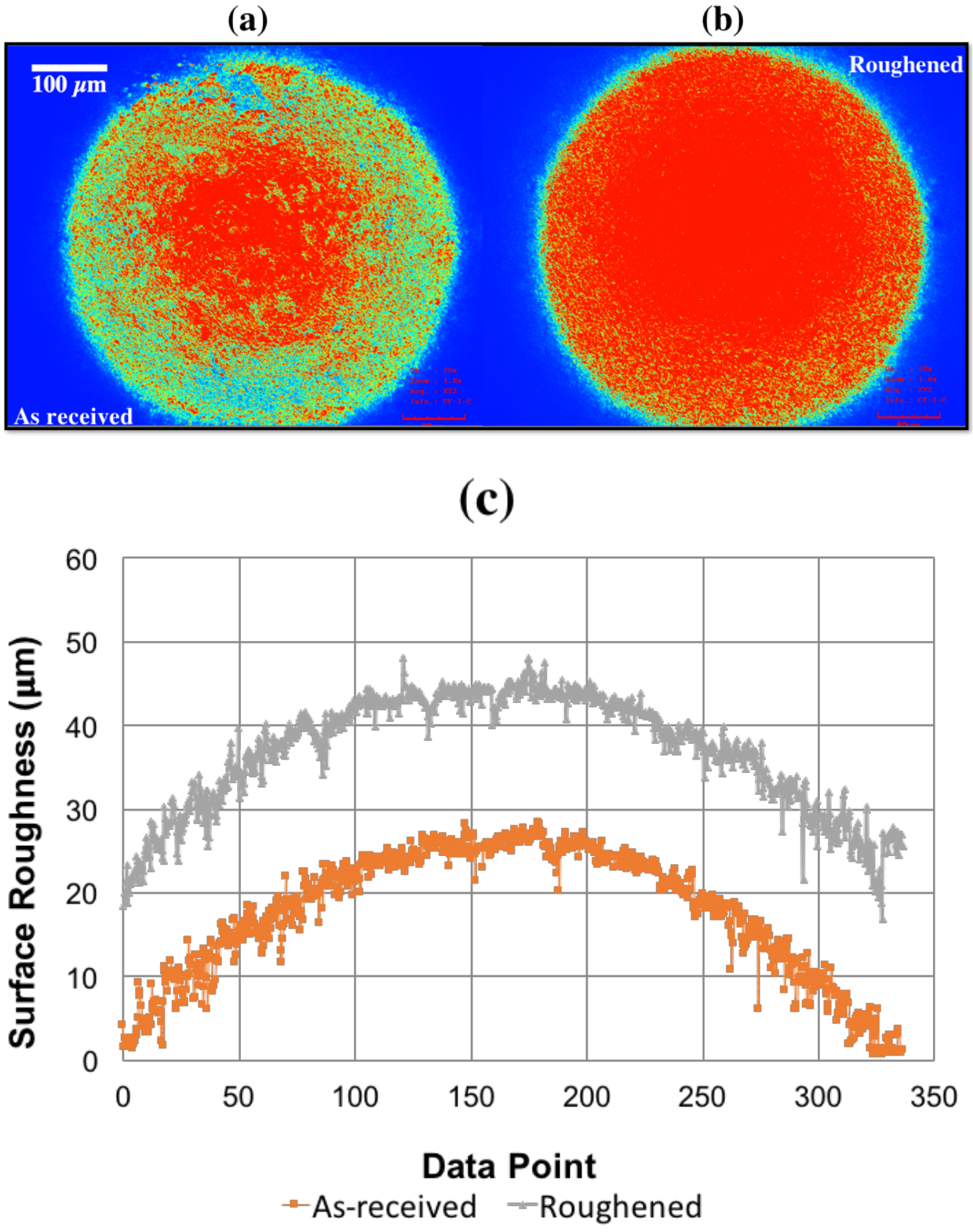

Figure 2.8 Surface texture maps of as-received (orange) and roughened (gray) inclusion from a 20x scan are shown in **(a)** and **(b)**. The surface roughness profile of the both cases are shown in **(c)**.

2.2 Experimental Set Up

2.2.1 *In Situ* Mechanical Testing

In situ compression experiments were performed on the polymer composites inside an X-ray tomography machine and scanned at a magnification of 1x and/or 4x (imaging described in the next section). Using the Deben CT500 *in situ* compression stage, load was applied in displacement control while the sample was inside the tomograph. The screw driven CT500 compression stage is shown in the right hand of **Figure 2.9** where the loading is applied in the direction of the black arrow (positive z-axis) and the sample is shown by the yellow arrow. A displacement rate of 0.5 mm/min was used, and to prevent shearing a lubricant was placed on the top and bottom of the sample. The polymer tube, or casing of the loading device, is made of polyetherimide (ULTEM) allowing a transparent support for X-rays to penetrate the 1.5 mm wall thickness tube. Compressive load was measured by a 500 N load cell within the base of the Deben stage and processed using software called Microtest.

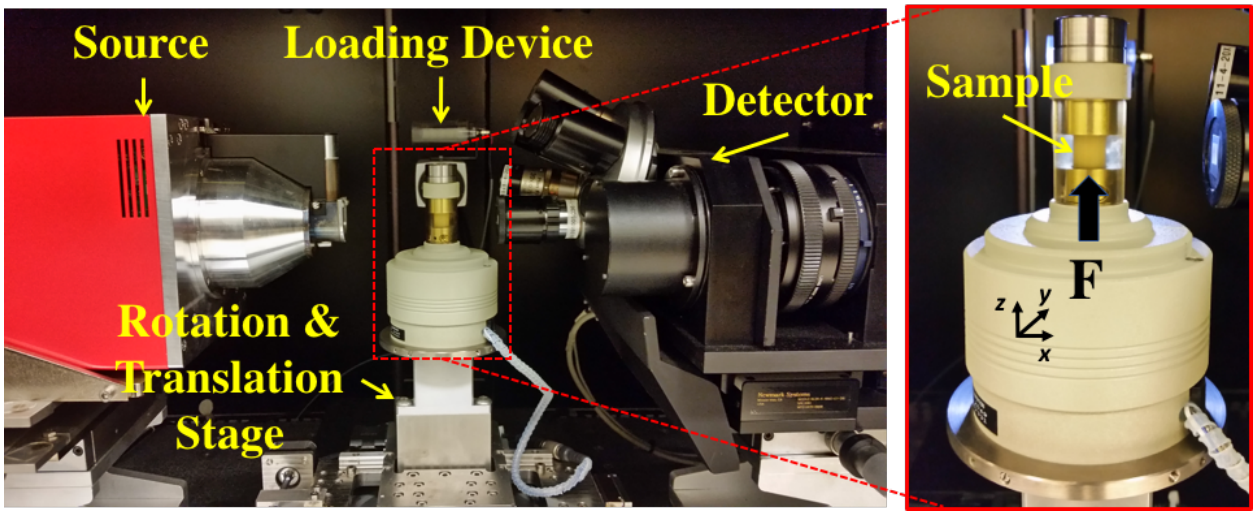

Figure 2.9 Experimental set up. The source and detector enabled three-dimensional visualization of the polymer composites. The *in-situ* compression stage (enclosed in red) was used to compress the specimens, in the + *z*-direction and indicated by the black arrow.

To determine the constitutive behavior of the baseline polymer composite (i.e., PDMS with 15% vol. 35 μm SiO_2 particles) and the additional effect of embedding a macro-size alumina particle (0.5 mm or 1 mm), several PDMS35μm15%vol and SI samples were manufactured and mechanically tested. All samples were loaded at a displacement rate of 0.5 mm/min up to a total applied displacement of 4 mm. **Figure 2.10 (a)** and **(b)** illustrate the stress vs. strain curves of a number of PDMS35μm15%vol samples. It is evident, from **Figure 2.10 (a)** that the constitutive behavior of the composites shows scatter. Hence, an average response curve was determined and is shown in **Figure 2.10 (c)**. The same scatter also carries over to the (macroscale) stress-strain response of the SI samples whose individual response is shown in **Figure 2.10 (b)** and average response in **Figure 2.10 (c)** as well. For completeness, **Figure 2.10 (c)** also shows the average curve of pure PDMS obtained in the same way described above. The average curves show that there is a stiffening effect of the pure PDMS with the addition of the 35 μm SiO_2 marker particles, and a further stiffening beyond that with the addition of the alumina inclusion.

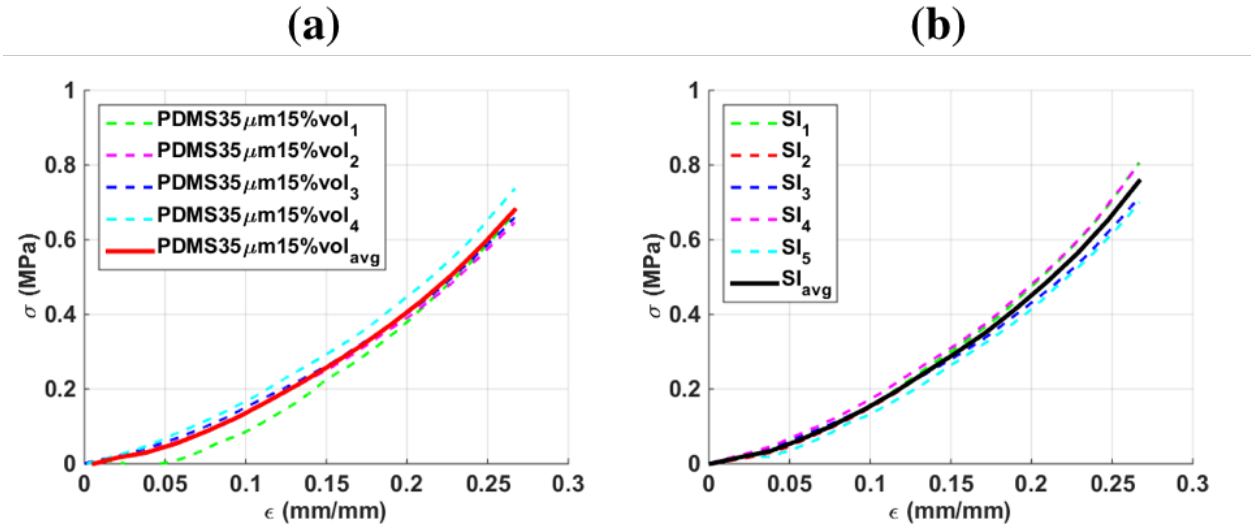

Figure 2.10 Stress vs. Strain curves of **(a)** PDMS with embedded particles, **(b)** SI samples, and **(c)** average curves, including for pure PDMS.

(c)

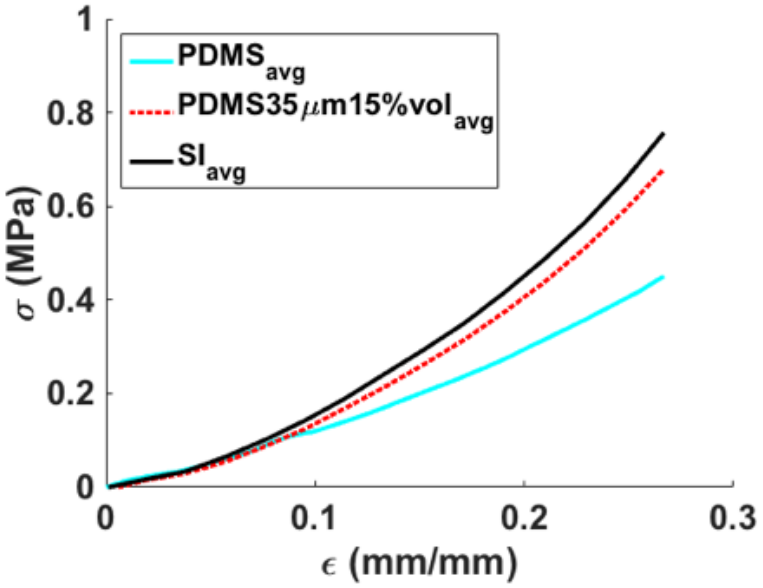

Figure 2.10 (cont.)

2.2.2 X-RAY MICRO-COMPUTED TOMOGRAPHY

To analyze the response of the composite material and to quantitatively study internal flaws and damage evolution, three-dimensional (3D) imaging data was acquired using an Xradia MicroXCT-400 located in the Microscopy Suite at Beckman Institute. The equipment can accommodate *in situ* or *ex situ* imaging capabilities with sub-1 μm pixel resolution. The MicroXCT-400 is able to contain sample sizes up to 200 mm in diameter and 2.2 lbs in weight. The MicroXCT-400 has an electrical potential energy range of 20-90 keV, which is suited for low density materials such as a polymer composite. **Figure 2.11** shows the X-ray microCT machine that was used in conjunction with the built-in software for acquiring 2D radiographs data and reconstructing it to obtain 3D data (XMController and XMReconstructor described in the next section). The key components within the microCT, X-ray source, detector and rotation/translation stage are shown on the right schematic, in the figure below.

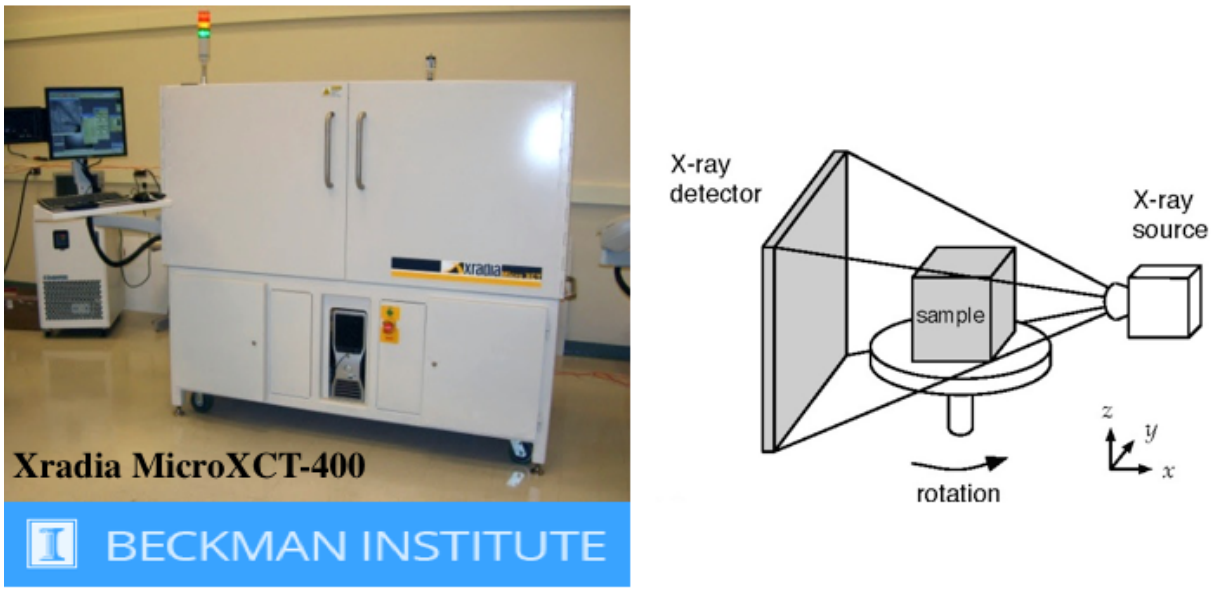

Figure 2.11 Xradia MicroXCT 400, in the Microscopy Suite in Beckman Institute, used to conduct 3D imaging.

2.2.3 Scanning and Data Reconstruction

Commercial software, XMController, was used to create a recipe file that established the parameters for a scan. The essential sections of the recipe file are: acquisition, camera, source, magnification, and tomography locations. Important settings such as total number of images, exposure time, camera binning, source voltage, source power, magnification, and source/detector distance were determined in their corresponding section. In order for consistency among the data sets, necessary for not only imaging but also the performance of quantitative metrology (DVC described below), successive scans were done using the original recipe file settings. This will allow direct image comparison between successive scans of the same experiment, as required by DVC. Radiographs images were taken at 1° increments for 360° rotation with 2-4 images being taken and averaged at each increment to reduce noise. The X-ray source potential electrical

energy and power were selected based on the polymer composite to ensure the detector's absorption percentage of the X-ray was greater than 30%.

All composites were imaged using 4x magnification with the following conditions: 42 keV (energy), 8 W (power), and 5 seconds of exposure time. The reconstructed tomographic scans produced cross-sectional slices with thickness (height) equivalent to the pixel size. Hence, the resulting 3D voxels are cubic, making the spatial units universal in all three orthogonal directions. (A voxel is defined as a volumetric pixel, 1 voxel = 1 pixel x 1 pixel x 1 pixel.) The 3D volumetric data contained approximately 500 million pixels and required ~ 90 – 120 minutes to generated, depending on the scan specs. The volume size of the 3D data was usually 1016 pixels x 1016 pixels x 996 pixels, resulting in a ~1.5 GB scan file (*. txrm). Reconstruction of the scan file yielded another 2 GB file (*.txm) which was then used to obtain a 6 GB 3D viewing file (*.txm-exm-ooc). Typically, an experiment required a total storage of 110 GBs: 16 GBs for scan files, 24 GBs for reconstruction files, 60 GBs for 3D visualization files (Amira) and an additional ~10 GBs storage for image exportation (*.tif). X-ray microCT parameters used in this work are shown in **Table 2.1**.

Table 2.1 X-ray microCT settings used for particulate composites.

Sample	Detector-Sample Distance (mm)	Source-Sample Distance (mm)	Resolution (µm/pixel)
SI	32	50	7.98
DI	25	90	5.25
RDI	44	90	1.77
RII	28	90	5.12
VII	21	90	5.44

The radiographs obtained from running a recipe file were reconstructed, using the commercial software XMReconstructor, to develop 3D volumetric data showing the distribution

of linear X-ray attenuation coefficients μ of the sample. Reconstruction of the radiographs, accounted for the cone angle of the lab-based source, by the implementation of a standard Feldkamp filtered back projection algorithm (Feldkamp et al. 1984). The value of μ depends on the X-ray photon energy, the material density, and the atomic number so that the contrast in CT images was usually given by differences in absorption between attenuation phases with different compositions or densities (Limodin et al. 2010). The relevant parameters within the Reconstruction Settings window are "center of shift" and the "min" and "max byte scale" values. The rest of the settings were disregarded in order to minimize the alteration of the raw data. The center of shift determined the amount, in pixels, that the axis of rotation is offset from the center column of the detector. **Figure 2.12** depicts a good center of shift (middle), which produced images that are focused and clear, and a bad center of shift (left and right), which resulted in blurry and fuzzy images. The center of shift was manually selected, for each reconstruction, and depended upon the image quality.

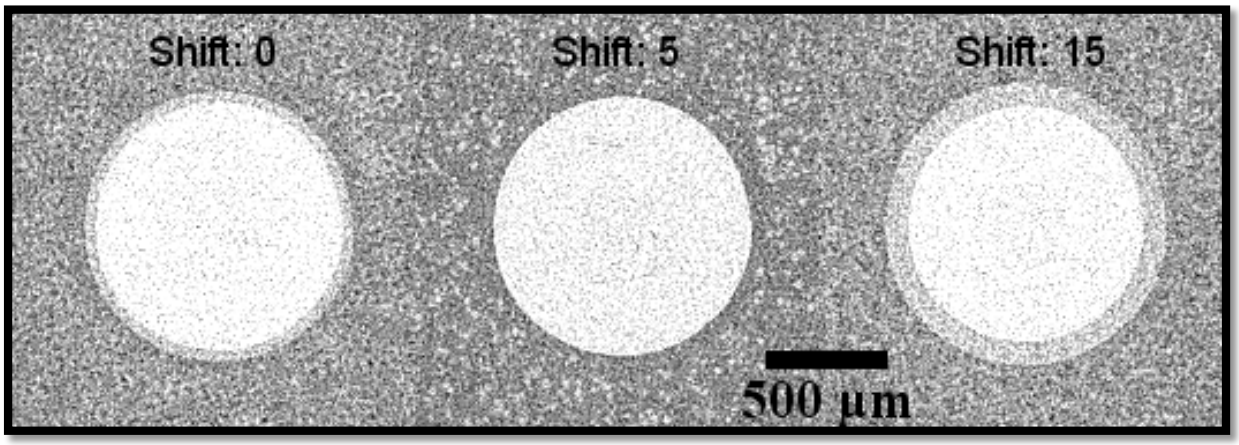

Figure 2.12 Center of shift determination example. A shift of 0 and 15 pixels creates an out of focus image (left and right) while a shift by 5 pixels develops a clear image (middle).

After reconstruction of the first scan, the volume viewer file (*.txm) was uploaded to XMController to acquire the global minimum and maximum byte scale values. This was done by

accessing the image control panel, and enabling the reconstruction parameters in the Info tab. The byte scale values were required to reconstruct successive scans on the same intensity scale as the original scan. It should be noted that byte scaling consecutive scans was only possible when the scan settings were identical to the original scan. Applying the CT byte scaling feature in the XMRecontructor program was necessary for visualizing and analyzing the image datasets, through a variety of programs such as Amira, ImageJ and MATLAB.

2.2.4 Data Visualization and Extraction

The final step in the imaging process was to upload the reconstructed file (*.txm) to another commercial software, Xradia 3DViewer. The file was uploaded using the "out-of-core" feature to obtain a new file with a format readable by Amira (*.txm-exm-ooc). The out-of-core tool allows for loading and visualization of large data sets greater than the amount of RAM available on the computer. Consequently, the Amira file (*.txm-exm-occ) was uploaded, using "Read complete volume into memory" as the loading policy, into Amira for visualization of orthoslices, volume renderings, image and material segmentation, 3D surface renderings, analysis, extraction of 2D slices and mesh generation. Under the Object Pool Editor, the orthoslice module tool in Amira allowed for the visualization and extraction of x-y, x-z, and y-z plane slices of the volume. The Volren module tool developed volume renderings of the scanned object that were mapped to a colormap. A volume rendering and orthoslice of the fracture surface from a carbon fiber tensile sample, illustrate an example of data visualization and extraction done within Amira, is shown in **Figure 2.13**.

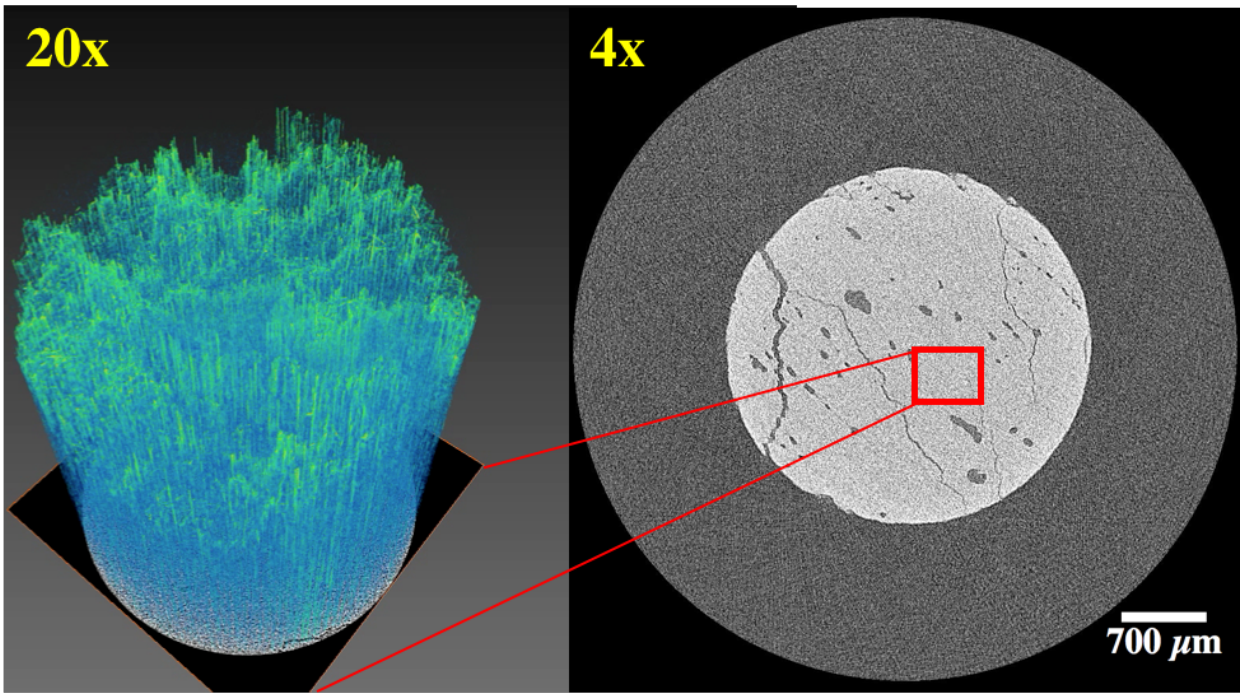

Figure 2.13 Example of data visualization and extraction in Amira. Using a 20x and 4x magnification a fracture surface of a tensile carbon fiber specimen was scanned and analyzed. A volume rendering and orthoslice, in *x-y* plane, of the fracture surface and are shown.

2.3 Digital Volume Correlation Algorithm and Implementation

The metrology used to quantitatively study the internal deformation, flaws, and damage evolution in the PPMCs is Digital Volume Correlation (DVC). The three-dimensional advancement of two-dimensional digital image correlation (DIC), referred to as DVC, enables full-field internal strain and displacement measurements resulting from an externally applied load. Like DIC, in DVC the material must contain an internal "speckle" pattern that is observable by the imaging technique. The internal pattern can either be a natural characteristic of the material, *e.g.* bone and foam (Bay et al. 1999, Liu et al. 2007, Lenoir et al.2007, Roux et al. 2008, Frank et al. 2007) or it can be artificially created during manufacturing (Germaneau et al. 2007, 2008, Gates et al. 2010). Here the 35 μm SiO_2 particles which were introduced in the PDMS matrix as described earlier serve as the marker particles. In this work, the DVC algorithm

developed by Gates *et al*. (2011) was used in junction with Illinois Taub Campus Cluster. A batch file was used to submit jobs, while a config file was used to define correlation settings. The inputs, which are discussed in Chapter 3, include subset size, correlation grid, step size, correlation function, minimization method, and a *c-target-coarse* value. Within the DVC algorithm, parallel computing is used to analyze large-scale data sets with hundreds of thousandths of correlation points. The computation time is comparable to the scan times. A short description of DVC is given below; for more details the reader is referred to Sutton et al. (1999).

A simple example of the 3D DVC metrology is shown in **Figure 2.14** on a polymer composite, PDMS with embedded silica glass beads of 35 μm with 15%vol (from Gonzalez et al. 2016). A reference 3D volumetric data set is shown as a series of tomography-extracted horizontal slices (x-y plane) through the z-axis. The 3D data represent intensity values (based on absorption and attenuation coefficients mentioned in the previous sections) at voxel locations on a 3D correlation grid (red dashed bounding box). **Figure 2.14 (a)** displays four slices out of a total of 996 in the reference configuration. The internal pattern, used to track deformations, is visible in each slide as the small white dots. A representative volumetric subset, shown in yellow, is present in both the reference and deformed state. The cross-sectional slices of the deformed sample are shown in **Figure 2.14 (b)**. For this illustration, the polymer composite was deformed by applying a rigid body rotation in the x-y plane. Using the defined 3D correlation grid and volumetric subset, DVC computes the displacements that map the subset in the reference to the deformed state, for each correlation point. The resultant displacement field, superimposed on the reference state in **Figure 2.14 (c)**, is obtained from applying a rigid body rotation of 2°.

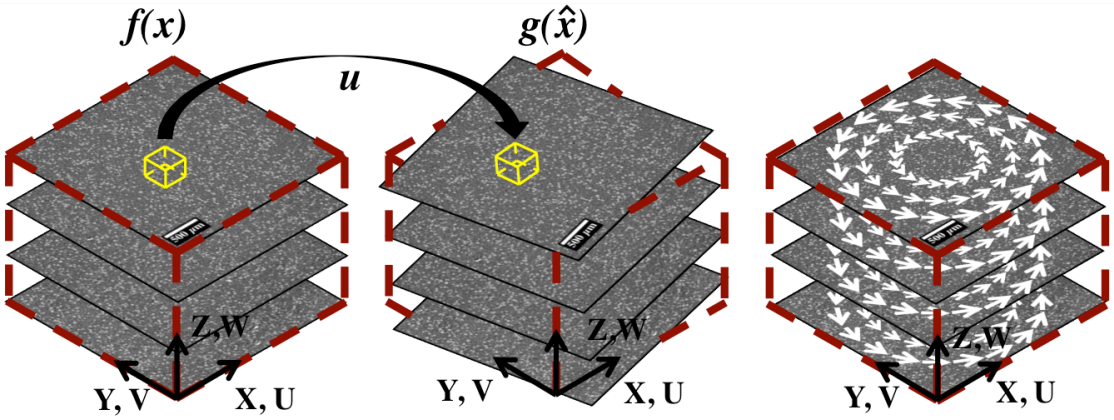

(a) Reference Slices **(b) Deformed Slices** **(c) Resultant Field**

Figure 2.14 DVC illustration, rigid body rotation of 2° is applied on 996 slices (4 shown). Volumetric subset in yellow of the **(a)** reference state is mapped to the subset in the **(b)** deformed state. The **(c)** resulting displacement field is represented on the reference state.

The mapping between the reference and deformed configurations is either linear or quadratic. The shape function dictates how the volumetric subset is allowed to deformed, and the degrees of freedom (DOFs) computed at each correlation point. A linear shape function in 3D contains 12 DOFs, that consist of the displacements and their first derivatives in each direction (x, y, z),

$$\mathbf{u} = \left[u \ \frac{\partial u}{\partial x} \ \frac{\partial u}{\partial y} \ \frac{\partial u}{\partial z} \ v \ \frac{\partial v}{\partial x} \ \frac{\partial v}{\partial y} \ \frac{\partial v}{\partial z} \ w \ \frac{\partial w}{\partial x} \ \frac{\partial w}{\partial y} \ \frac{\partial w}{\partial z}\right]^T. \tag{2.1}$$

The linear shape function maps the reference subset, $f(x)$, centered at the correlation point, $p = \{p_x, p_y, p_z\}$, to the deformed subset, $g(\hat{x})$. Using the following affine linear shape function, a voxel point, $x = \{x, y, z\}$, in the reference subset is related to a point, $\hat{x}$, in the deformed subset,

$$\hat{\boldsymbol{x}}(\boldsymbol{u}) = \begin{bmatrix} \hat{x}(u) \\ \hat{y}(u) \\ \hat{z}(u) \end{bmatrix} = \begin{bmatrix} x + u + \frac{\partial u}{\partial x}x + \frac{\partial u}{\partial y}y + \frac{\partial u}{\partial y}z \\ y + v + \frac{\partial v}{\partial y}x + \frac{\partial v}{\partial y}y + \frac{\partial v}{\partial z}z \\ z + w + \frac{\partial w}{\partial x}x + \frac{\partial w}{\partial y}y + \frac{\partial w}{\partial z}z \end{bmatrix}, \tag{2.2}$$

where (x, y, z) are the local subset coordinates and (u, v, w) are the displacements and their corresponding first derivatives. **Figure 2.15** shows the linear mapping for subset displacements utilized in the DVC algorithm.

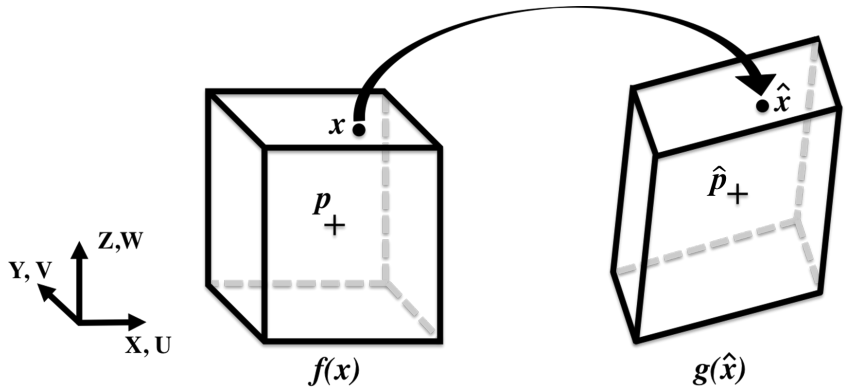

Figure 2.15 Linear shape function mapping of representative DVC reference subset f with correlation point p and deformed subset g with correlation point $\hat{p}$

Computing the displacements in DVC requires the minimization of a correlation function, $c(u)$ that measures the difference between reference and deformed subset. Two conventional correlation functions used in DVC are the least-squares correlation function (Sutton et al. 1983)

$$c(u) = \frac{\sum_x (f(x)-g(\hat{x}))^2}{\sum_x f(x)^2} = \frac{\| f-g \|^2}{\| f \|^2} \tag{2.4}$$

and the normalized cross-correlation function (Sutton et al. 1983, 2009),

$$c(u) = 1 - \frac{\sum_x f(x)g(\hat{x})}{(\sum_x f(x)^2)^{0.5}(\sum_x g(\hat{x})^2)^{0.5}} = 1 - \frac{\langle f, g \rangle}{\| f \| \cdot \| g \|} \tag{2.5}$$

The correlation functions are defined by a summation of all the voxels in a subset and output non-negative values.

CHAPTER 3: DATA ANALYSIS AND RESULTS

The global and local analyses of the data sets were conducted using Amira, ImageJ, and MATLAB. Amira was used for analysis, complex visualization and construction of meshed surfaces of volumetric features. ImageJ was used for visualization, file conversion, and measurements (scale bar, length, width, distance, etc.) of the data sets. MATLAB algorithms were developed to process image stacks (*.png) (cropping, removal of rigid body motion), to construct different correlation grids for DVC and to analyze the DVC output file (final-23.csv). Depending on the type of inclusion shape, i.e., spherical or irregular, different image processing techniques were utilized to remove the rigid body motion and to create a correlation grid. After, creating the correlation grid, it was saved as a text file (*.txt) to upload onto the Taub Campus Cluster, along with the processed undeformed and deformed image data sets.

3.1 DVC PREPROCESSING

3.1.1 INCLUSION DETECTION ALGORITHM

Processing the alumina inclusion data sets began by importing the exported image stack (*.tif), from Xradia, into ImageJ to convert its image format. This was done by clicking the *File* Tab > *SaveAs* > *Image Sequence*, selecting the new file format (*.png) and then clicking on the checkbox "Use slice labels as file names". Using ImageJ1, the equatorial plane of the inclusion/s was determined and recorded into an excel input file (*.xlsx). Next, the data were imported into MATLAB where an existing routine was used to approximately locate the center coordinate and radii of the alumina inclusion/s. The gradient field of the image was processed using Circular Hough Transform algorithm to detect circular shapes in a gray scale image and resolved their center positions and radii, as shown in **Figure 3.1**. The center coordinates of the inclusion/s were

then used to remove the rigid body translation on successive image data sets relative to the original dataset by selecting a reference inclusion and considering its center as the common point among all images. This is an easy way to remove rigid translation which would otherwise affect the DVC measurements. A scheme was also developed to approximately account for rigid rotation based on aligning the centerlines of multiple spheres (in experiments where more than one inclusions were present). Furthermore, the center coordinates and radii of the inclusion/s were also used to create the correlation grid, since the information was used to removed correlation points within the inclusion/s. The scheme and process of creating a correlation grid are described in detail in the following sections.

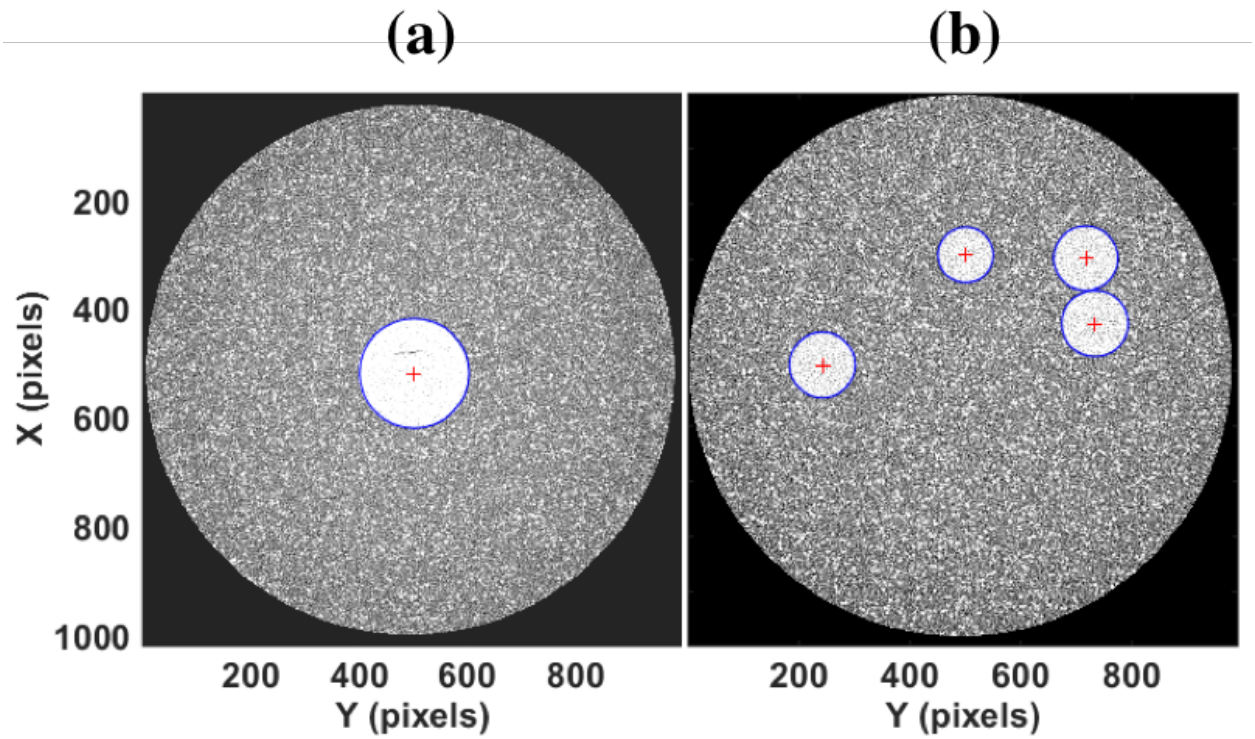

Figure 3.1 Inclusion detection algorithm example of an orthoslice with single inclusion **(a)** and with concentric inclusions **(b)** are plotted in image coordinate frame.

3.1.2 Rigid Body Motion Removal

It is important to remove, to the extent possible, both components of rigid body motion, i.e., translation and rotation, from the image data sets since this simplifies the process of correlation by producing DVC results that are generated from deformation only. For single inclusion experiments, only the translation component of rigid body motion could be removed easily during the preprocessing of data sets. The translation component was removed by shifting the center coordinate of the inclusion in all successive image data sets, to match the center coordinate of the inclusion in the original image set. This was achieved by computing the number of pixels that the deformed image stacks had shifted in the *x, y,* and z directions during each scan and adjusting for that value to return the inclusion center to the same location for each scan. After removing the translation component, the SI data sets were then correlated. An illustration of translating the inclusion in the deformed (dashed sphere) data set, to match the original (solid sphere) data set, is shown in **Figure 3.2 (a),** where (t_x, t_y, t_z) are the translation values. Unfortunately, because of the spherical symmetry of the inclusion it was not possible to perform a similar correction for rigid rotation and thus the results will still contain rigid rotation. Note, however, that (a) because of the spherical symmetry of the problem this rotation will not really affect the physical behavior of the system, and (b) none of the rigid rotation correlated values affect strain which is a quantity depending on deformation only. For an image that does not possess spherical symmetry, such as for example those with irregular shaped embedded inclusions, it is actually possible to also remove rigid rotation in addition to translation as following sections and Chapter 5.

For multiple inclusion data sets, the translation and rotation component of the rigid body motion were removed using the center coordinates of an inclusion selected as the "origin"

inclusion and a second selected as the "marker" inclusion, respectively, both selected arbitrarily. In double inclusion experiments, the origin inclusion was selected as the bottom inclusion and the marker inclusion as the top inclusion. For the randomly distributed inclusion experiment, of which we performed one, the origin inclusion was selected as the 14^{th} inclusion counting from the bottom to the top, and the marker inclusion as the 9^{th} inclusion. Generally, we tried to select inclusions that were somewhat further separated from neighboring inclusions, i.e., more isolated in space, and also were as far apart as possible, though these are not necessarily requirements of the method. Like before, the translation component was removed by fixing the center point of the origin inclusion in successive data sets to be at the location where it was in the original state. The rotation component was (approximately) removed, as shown in **Figure 3.2 (b)**, by aligning the center of the marker inclusion in the deformed state relative to the undeformed state and not the original scan, thus essentially aligning the straight line that connects the origin and marker sphere centers to fall along the same direction in both the undeformed and deformed scans. The reason why the centerline was not aligned relative to the original scan is addressed in Section 3.2. The angle of rotation, α, needed for this alignment was obtained by first computing the vector of the marker inclusion, in the undeformed (d_1) and deformed (d_2) states, with respect to the center of the origin inclusion. The vectors were then projected onto the XY plane to compute the angle between them. The entire deformed (dashed sphere) data set was then rotated to be aligned to the undeformed (solid sphere) state using the computed angle thus removing the rigid rotation from the entire data set, at least approximately (since this method does not compensate for the differing magnitudes in the before and after vectors).

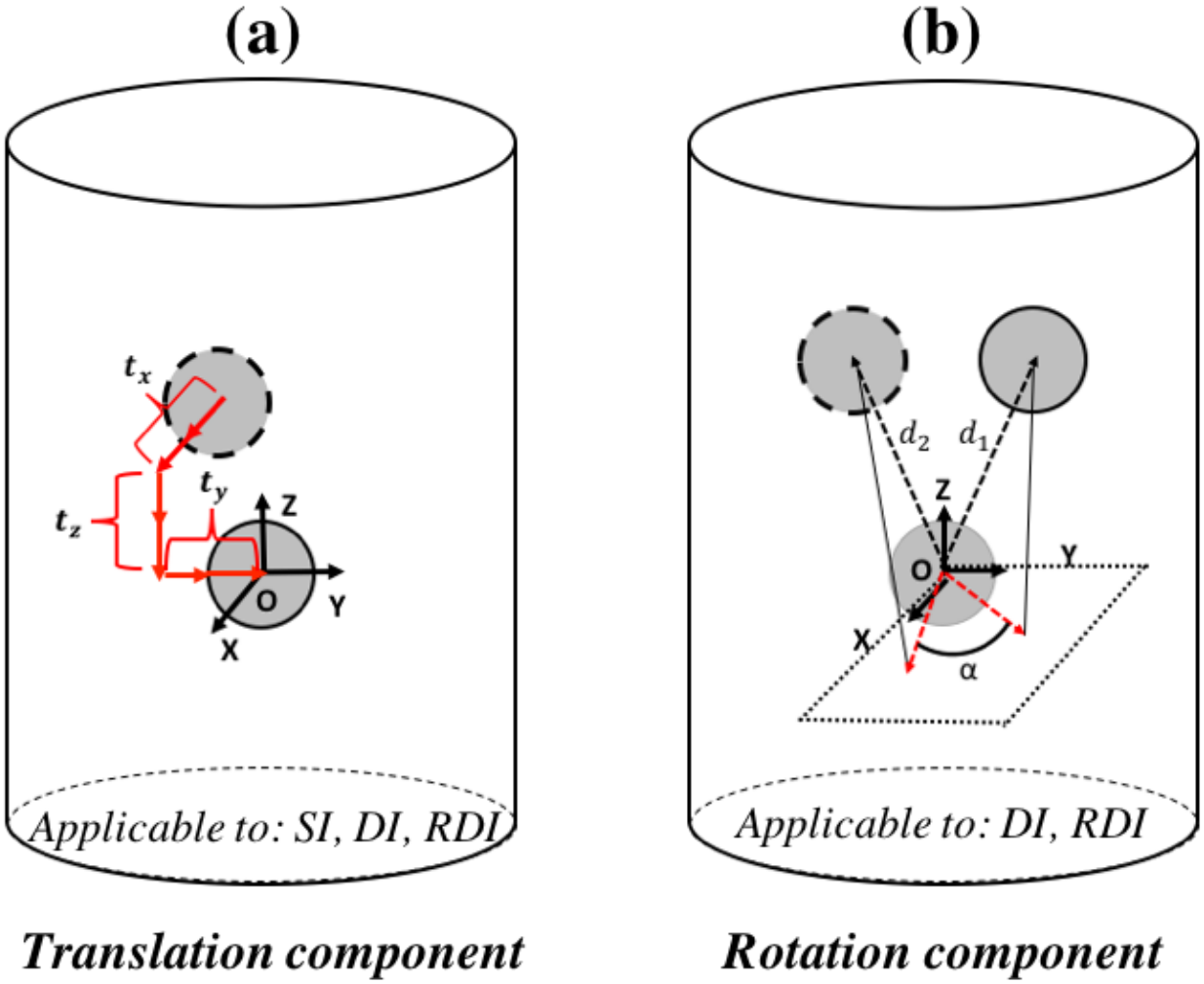

Figure 3.2 Illustration of procedure for removing rigid body motion. Removal of the translation component **(a)** only applicable to SI, DI and RDI datasets, removed by computing the number of pixels that the deformed image stacks had to be shifted in the *x*, *y*, and z directions (t_x, t_y, t_z). Removal of the rotation component **(b)** only applicable to DI and RDI datasets, removed by rotating the deformed data sets by $\boldsymbol{\alpha}$, the angle between the XY projections of the two vectors, d_1 and d_2.

Removing the rigid body motion from irregular inclusion experiments was done using MATLAB and an ImageJ plugin, *Rigid Registration*. Similar to the spherical experiments, first ImageJ was used to determine the scanned equatorial plane. Note the scanned equatorial plane can differ significantly from scan to scan; since it is impossible to obtain exactly the same

imaging FOV in all scans. The information needed to compute the translations (x and *y*) and rotation component were acquired by analyzing the equatorial slices with respect to the original equatorial slice. Image processing functions within MATLAB (*e.g detectSURFFeatures*, *extractFeatures*, *matchFeatures*, and *estimateGeometricTransform*) were used to estimate the number of pixels and the angle of rotation that had to be applied to match the original slice. The values were then recorded on the excel sheet used to remove rigid body motion and to create the correlation grid, and imported in MATLAB to run the preprocessing algorithms. Further work to properly remove rigid body motion in irregular inclusion data sets needs to be done. However, at least in principle, with distinctly shaped irregular rigid inclusions it should be possible to entirely remove both rigid translation and rotation by aligning precisely the shape of the particle among all scans. Since the particle shape is irregular, this alignment in 3D space will be unique, thus providing the rigid translation and rotation corrections needed. Chapter 5 addresses how Amira can be used to determine the affine transformation matrix, that would transform a deformed data set to match the undeformed/original data set.

3.1.3 DVC Correlation Grid

DVC correlations were performed on a user-defined correlation grid of about half the scanned volume of the actual 3D scan. The correlation grid was restricted in this way mainly for faster computation time. The DVC parameters were kept the same for all correlation grids, although they may need to be varied if the internal speckle pattern changes. Here we consistently used the same pattern parameters while preparing the samples (Gonzalez et al. 2016), so we kept the correlation parameters the same throughout. The subsets used for the correlation were 41^3 voxels and the correlation point step size was 21 voxels. All correlation grids consisted of the

same dimensions, a height of 800 voxels (zmin = 100 and zmax = 900), length of 910 voxels (xmin = 30 and xmax = 940) and a width of 910 voxels (ymin = 30 and ymax = 940). When using DIC or DVC, it is common to overlap the subsets by about half the subset size, so a subset size of 41^3 voxels would result in a grid spacing of ~21 voxels in all three orthogonal directions (Forsberg et al 2009, 2010). A benefit of using a custom correlation grid, i.e., one that excludes certain regions of the sample from being correlated, is that it informs the DVC algorithm which regions to avoid, specifically regions that do not contain a speckle pattern (e.g., the alumina inclusion) or regions where the pattern may be damaged or missing (e.g., near voids). In alumina inclusion experiments, ImageJ, Excel, and MATLAB were used to generate custom correlation grids, while for the irregular inclusion experiments Amira and MATLAB were utilized. The development of the correlation grids began by constructing a rectangular grid (**Figure 3.3 (a)** and **(b)**), using the *meshgrid* function in MATLAB, and then customizing it into a cylindrical shape.

In the single inclusion correlation grid, correlation points that fell within the spherical inclusion and outside the field of view (FOV) were removed. The radii and center coordinate of the alumina inclusion, in the reference or original state, were used to generate the correlation grid using an in-house MATLAB algorithm. First the correlation grid details, i.e., minimum and maximum values of x, y, z, subset, step size, and FOV radius, relative to the center of inclusion, were obtained from the excel input file. Next a rectangular grid, [*X*, *Y, Z*] with dimensions of M x N x P, was created using the *meshgrid* function in MATLAB. To remove nodal points, the grid arrays were reshaped into vectors (1 x M*N*P) and then using nested loops and logic statements the custom correlation grid was obtained by removing points outside the FOV (**Figure 3.3 (c)** and **(d)**) and within the inclusion (**Figure 3.3 (e)** and **(f)**). The single inclusion DVC correlation grid remained the same throughout all the DVC correlations.

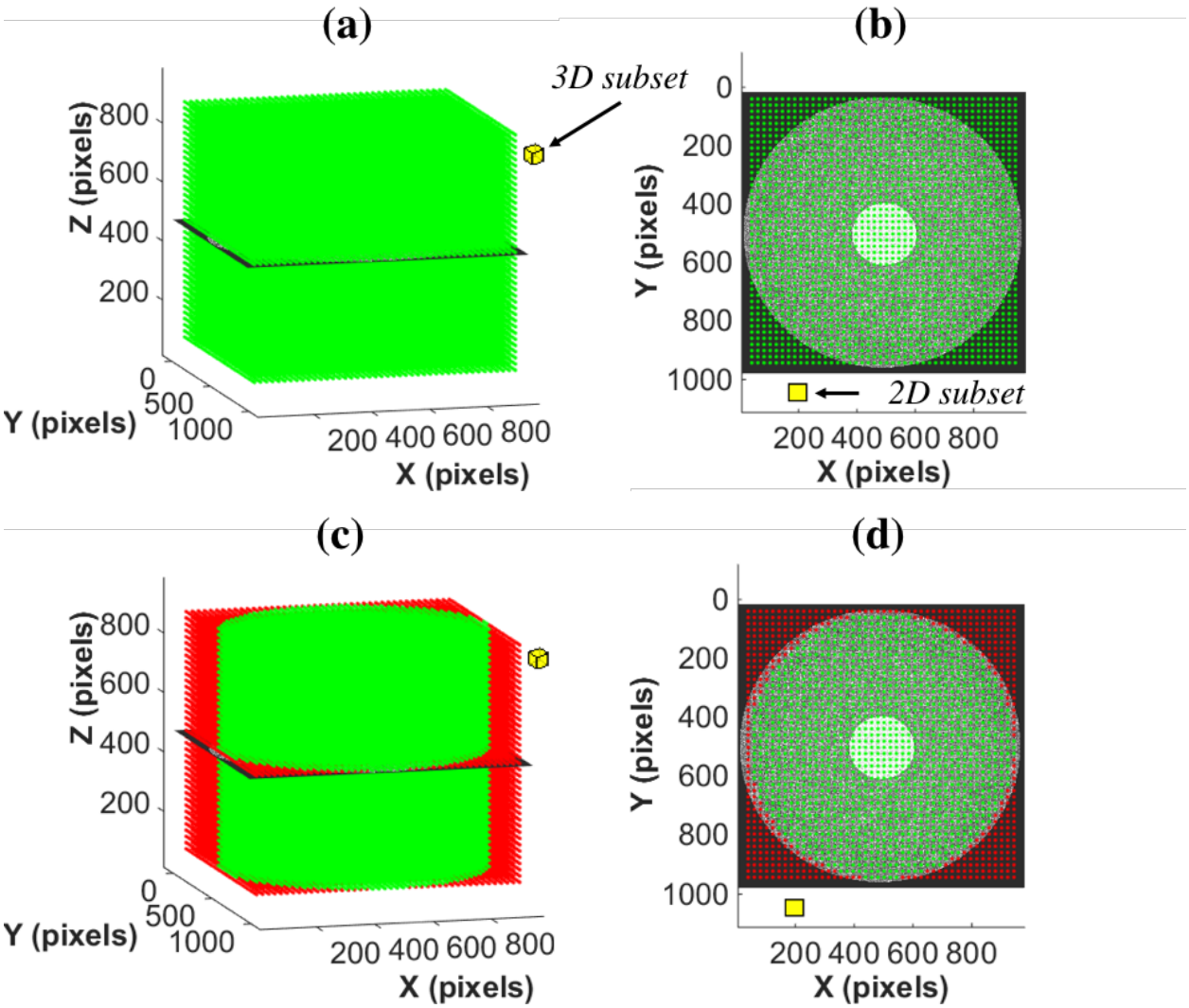

Figure 3.3 General method of creating a custom correlation grid for Digital Volume Correlation. A rectangular grid is defined using the step size and min and max values of x, y, and z **(a)** and **(b)**. Nodal points outside the field of view **(c)** and **(d)** and inside the inclusion are removed. The points removed from the correlation grid are shown in red and the points the remain to be correlated are shown in green. The final set of correlation points for the single inclusion geometry are shown in **(e)** and **(f)**.

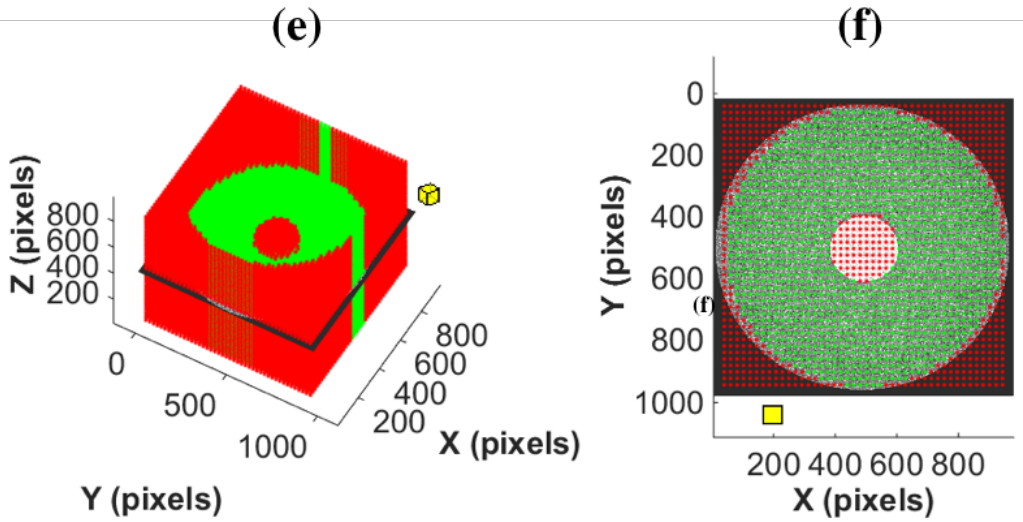

Figure 3.3 (cont.)

For samples with double inclusions, nodal points outside the FOV and within the origin inclusion (bottom sphere) **Figure 3.4 (a)** and marker inclusion (top sphere), in the undeformed **(b)** and deformed **(c)** configuration were removed. After creating the rectangular grid, the grid arrays were reshaped into vectors and then the distances between all correlation points and the center of the top inclusion, in the undeformed and deformed state, were computed. After removing nodal points outside the FOV as before, the correlation points that resulted in a distance less than or equal to the diameter of the top inclusion were removed from the correlation grid. The scanning of the double inclusion composite was done in a way in which the top inclusion moves towards the bottom inclusion, since the alignment of the scan was done relative to the bottom inclusion. Note, the alignment of the scan can be done relative to the center point between the two inclusions. As a result, the two inclusions will then appear to converge towards the same point in space. Furthermore, since the global position of the marker inclusion is different in each loading step, the correlation grid differs in each correlation. Recall that the origin inclusion is fixed in all deformed datasets relative to the original dataset.

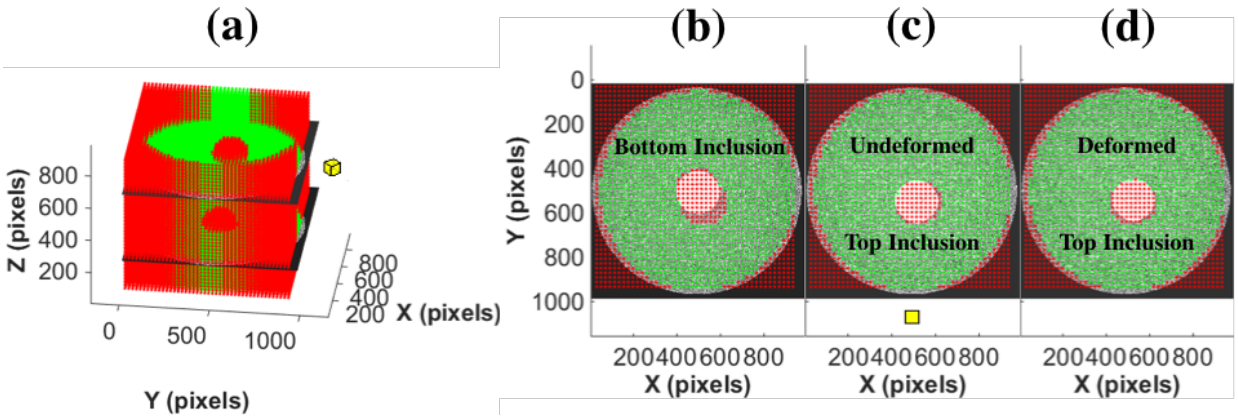

Figure 3.4 Resultant correlation grid for double inclusion configuration. Three-dimensional view of the nodal points removed (in red) **(a)**. Planar view of the nodal points removed from bottom inclusion **(b)** and the top inclusion, in the undeformed **(c)** and deformed **(d)** state.

The randomly distributed inclusion sample consisted of a complex three-dimensional microstructure, 20 alumina inclusion randomly positioned in space. Like the single inclusion correlation grid, only the nodal points within the origin inclusion, in this case the 14th inclusion, were removed. DVC was able to correlate the data despite not removing nodal points within the remaining 19 inclusion. The reason why DVC was able to correlate the data sets is discussed in the latter Section 3.2. It should be noted that removing the nodal points within the remaining inclusions could have been done by implementing 20 logic if conditions (one for each inclusion), but would have been quite cumbersome. Therefore, the correlations performed on the randomly distributed inclusion data sets are potentially more error prone. The correlation FOV (green doughnut shape), in **Figure 3.5 (a)** and **(b)** is limited, compared to the FOV in the single inclusion and double inclusion correlation grid. In retrospect, the correlation FOV could have been established relative to the center coordinate point of the image slice. Similar to **Figure 2.14**, **Figure 3.5**, displays the correlation grid in the reference configuration. As previously mentioned, using if statements with logic statements becomes an inefficient method to create complex correlation grids. The "tracking of inclusions and removal of nodal points" method is not useful

for complex microstructures, complex either due to the number of inclusions or due to irregular inclusion features. The last section illustrates different techniques that were used to create correlation grids for more complex microstructures. Chapter 5 discusses how the techniques can be applied to the randomly distributed inclusion experiment as part of future work (since this has not been fully explored here).

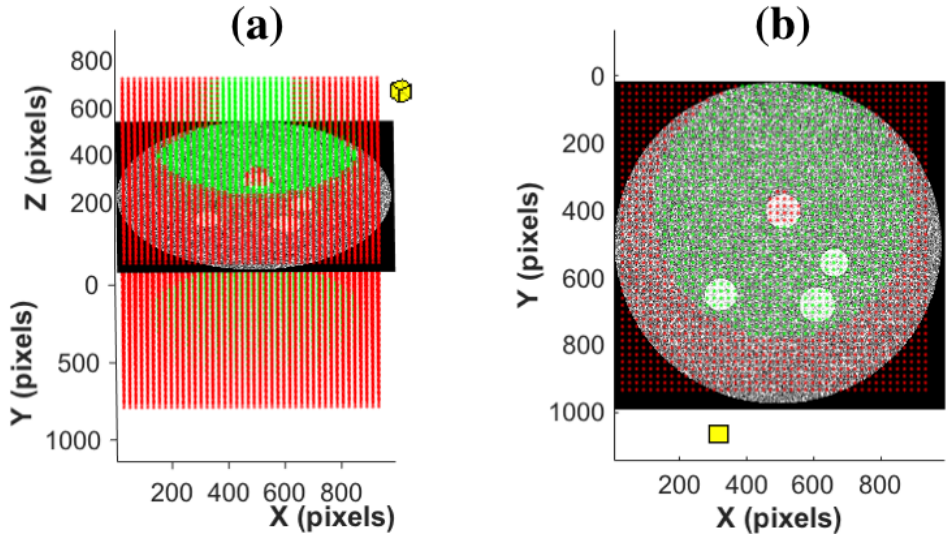

Figure 3.5 Correlation grid, relative to the 14th inclusion, for randomly distributed inclusions configuration. Three-dimensional view of the nodal points removed (in red) **(a)**. Planar view of the nodal points removed from origin inclusion **(b)**.

To create an irregular inclusion correlation grid, the original scan Amira file (*.txm-exc-ooc) was loaded into Amira. Within the Segmentation Editor, the *threshold* segmentation tool, with a data range between ~9000 and ~12000, was used to select the inclusion voxels (**Figure 3.6 (a)** and **(b)**). After adding the selected voxels to the desired material label, the material was then processed by smoothing it, removing islands and filling the holes. The processing of the segmented voxels was done by clicking on the material and then clicking on the *Segmentation* Tab > *Smooth labels*/ *Remove Islands*/ *Fill holes*. First, smoothing was done on *all slices* with 6 being the size parameter (**Figure 3.6 (c)** and **(d)**). Second, the removal of islands was done on *all*

slices, with 2000 as the size parameter and 0.25 as the fraction parameter (**Figure 3.6 (e)** and **(f)**). Lastly, the holes were filled in order to represent the inclusion as a solid, since it was somewhat porous.

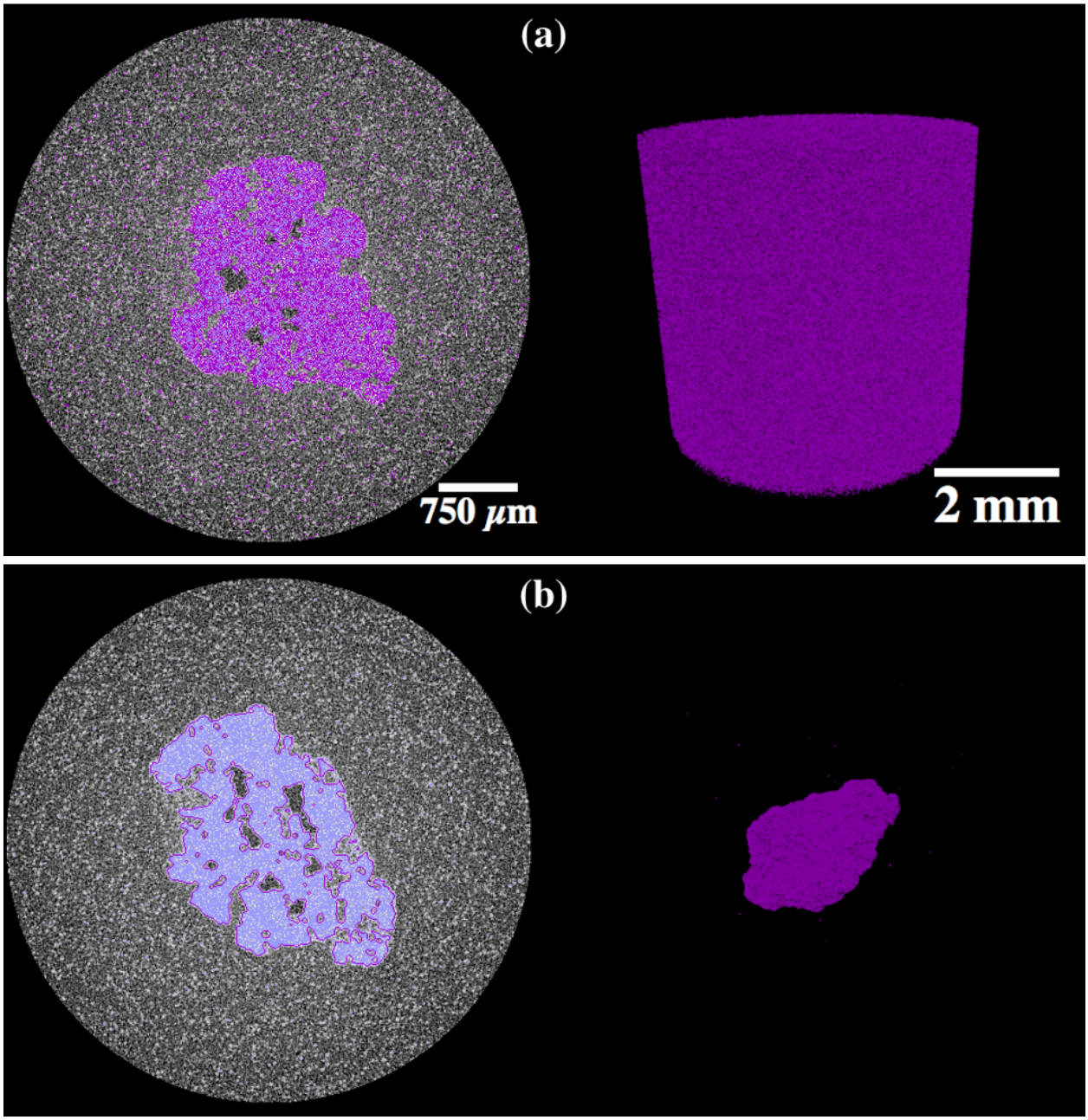

Figure 3.6 Image segmentation and mesh development procedure for an inclusion. Voxels between a data range are selected and added to the material label **(a)** and **(b)**. Selected voxels are smoothed which eliminates large islands **(c)** and **(d)**. The smaller islands are removed and the segmented surface is filled to be depicted as a solid **(e)** and **(f)**.

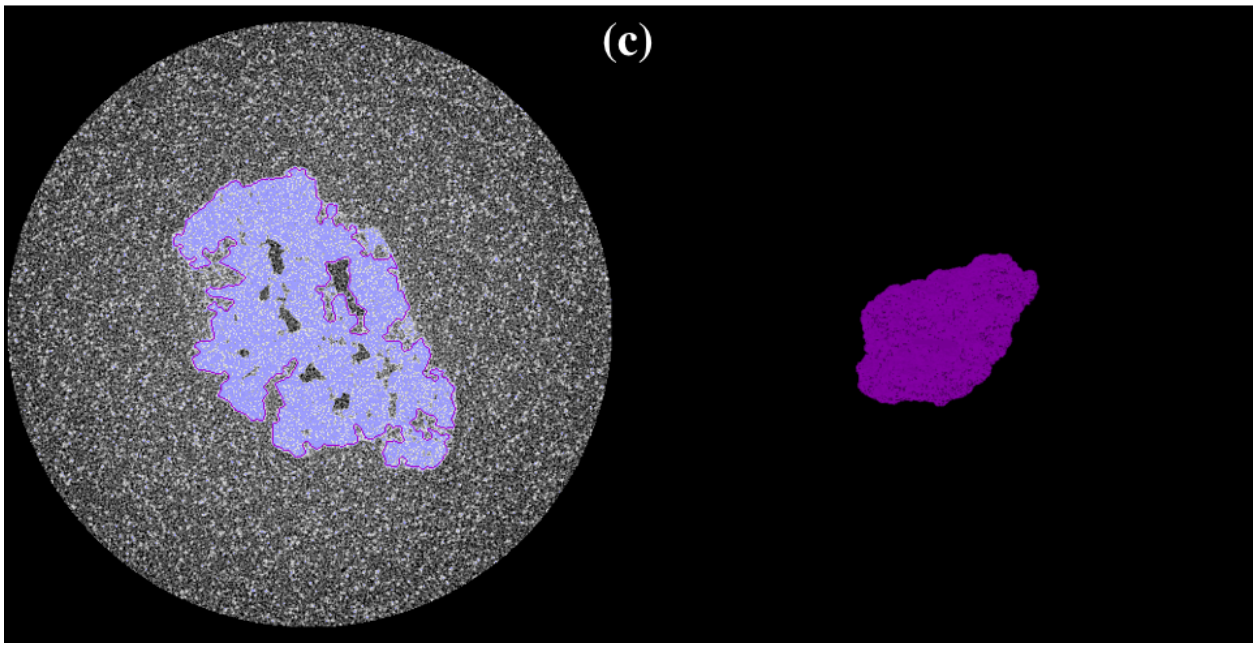

Figure 3.6 (cont.)

Once the contours of the segmented irregular inclusion were smoothed and filled, a meshed surface was generated by attaching a *SurfaceGen* module to data file (*.Labels.am). Prior to generating the surface, the Amira file (*.txm-exc-ooc) was rotated to match MATLAB's coordinate frame. Using the *Transformation Editor* > *Dialog* within the Properties window, an *Absolute* transformation was applied, first 270° about the positive z-axis (0,0,1) and then 270° about the negative z-axis (0,0,-1). Within the *SurfaceGen* module, a surface mesh was generated, using the default properties of the module, by clicking on the *Apply* button. The generated mesh consisted of approximately 2 million vertices. In order to reduce the data set, the surface was simplified. With the surface file (*.surf) selected, the *Simplifier Editor*, within the Properties window, was used to simplify the meshed surface to contain no more than 18000 (default value) vertices by selecting the *Simplify Now* button. Subsequently, the meshed surface was tested for flaws by selecting the *Surface Editor* within the Properties window. Next, by going to the *Surface* Tab > *Tests* > *Intersection/ Orientation/ Aspect Ration/… Tetra Quality*, each test was

chosen and if necessary auto-fix features (*Surface* Tab > *Edits*) were used. After simplifying, testing and fixing the meshed surface (*. surf), it was saved as an ASCII file (*.stl) by right clicking on the surface file within the Object Pool window.

The ASCII file was then imported into MATLAB, where an algorithm first normalized the surface by the voxel dimension (# μm/pixel) (**Figure 3.7 (a)**), then voxelised the surface and lastly created the correlation grid for DVC. To voxelise the surface a MATLAB function, *VOXELISE*, was used (Patil et al. 2005). As before, first a rectangular grid was created. The unique values, X_u (1xM), Y_u (1xN) and Z_u (1xP), of the grid arrays and the meshed surface were inputted into the *VOXELISE* function. The function outputted a multidimensional logic array (M x N x P), points inside the volume had a value of 1 and points outside the volume had a value of 0 (**Figure 3.7 (b)**). Again, the grid arrays, along with the multidimensional logic array, were reshaped into vectors and using nested loops and logic statements the correlation grid for an irregular inclusion was developed (**Figure 3.7 (c)**).

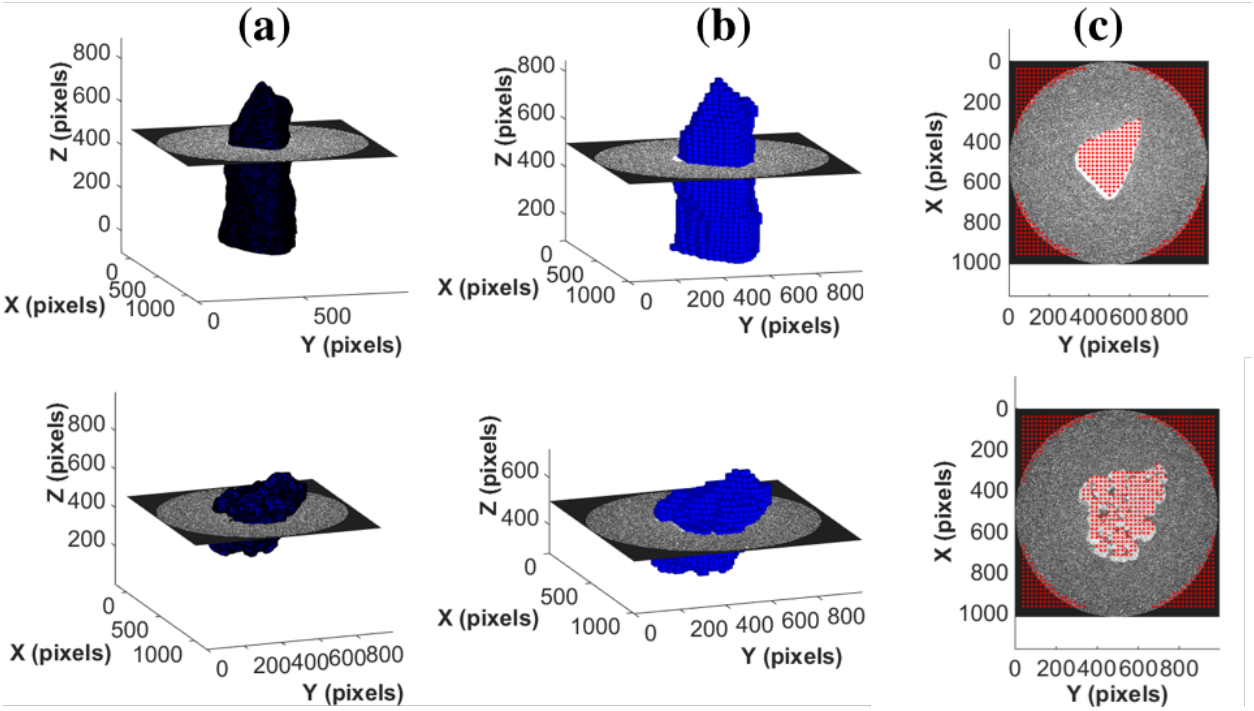

Figure 3.7 Development of correlation grid from a 3D surface. The meshed surface is first normalized by the voxel dimension **(a).** The triangular elements are transposed onto a Cartesian coordinate system **(b)**. The voxelised surface is used to develop the correlation grid for DVC **(c)**.

3.2 Correlation Results

Generally, in deformation metrologies such as DIC or DVC the deformed datasets are always correlated with respect to the reference undeformed, or original, data set. This can be done accurately for displacements where the speckle pattern remains within the FOV for both deformed and undeformed images. Here, correlating the deformed data sets with the original dataset only worked well for far field applied displacements less than 1.5 mm. Any DVC correlations beyond this amount resulted in erroneous correlation points greater than 70% of the total correlation points. To overcome this limitation, incremental correlations (I_i) were performed to correlate in a step-by-step progression. In other words, correlating the n^{th} step with step *n-1* (I_1 = step 1 with step 0 (original), I_2 = step 2 with step 1, I_3 = step 3 with step 2,

etc.) where n = 1,2,3, etc. By conducting incremental correlations, the correlated displacements were kept small in each case. The incremental DVC results can then be summed together to develop additive results (A_i), i.e., $A_1 = I_1, A_2 = I_1 + I_2, A_3 = I_1 + I_2 + I_3$, etc. until the desired total displacement loading step. Recall that only the translation component of rigid body motion (RBM) was removed for single inclusion data sets.

An advantage of studying the single inclusion configuration is that the DVC method can be validated using a closed-form solution. The relevant theoretical solution was formulated by Goodier and establishes the deformation field around a rigid inclusion in an infinite medium under uniaxial tension (Goodier et al. 1933). The Goodier solution was used as a tool to validate the DVC algorithm and to remove rigid body motion from the single inclusion DVC correlation results. The validation of DVC and formulation details, with regards to the Goodier solution, are discussed in Section 4.1. To remove the rotation component, from the single inclusion DVC correlation results, a least-square fit was applied to the raw displacement fields, prior to summing the steps. Using the Goodier displacement equations (Equation 4.1), the least-square fit was applied at *low loads* displacement fields, i.e., loading steps prior to interfacial failure. For correlations with more than one inclusion both components of RBM, translation and rotation, were removed as described in Section 3.1. The additive w^{DVC} displacement field for an SI (step 3 of **Figure 3.9**), DI (step 3 of **Figure 3.16**) and RDI (step 3 of **Figure 3.20**), are shown in **Figure 3.8** in the form of a 3D quiver plot. The plot displays displacement vectors, (*u, v, w*) at each correlation point (*x, y, z*), which are color-coded relative to their magnitude and direction. The 3D quiver plots illustrate the general behavior for all additive displacement step fields. In order to visualized the vector field effectively, only one-half of the correlation points are displayed. The compressive loading of all samples was applied in the +z-direction.

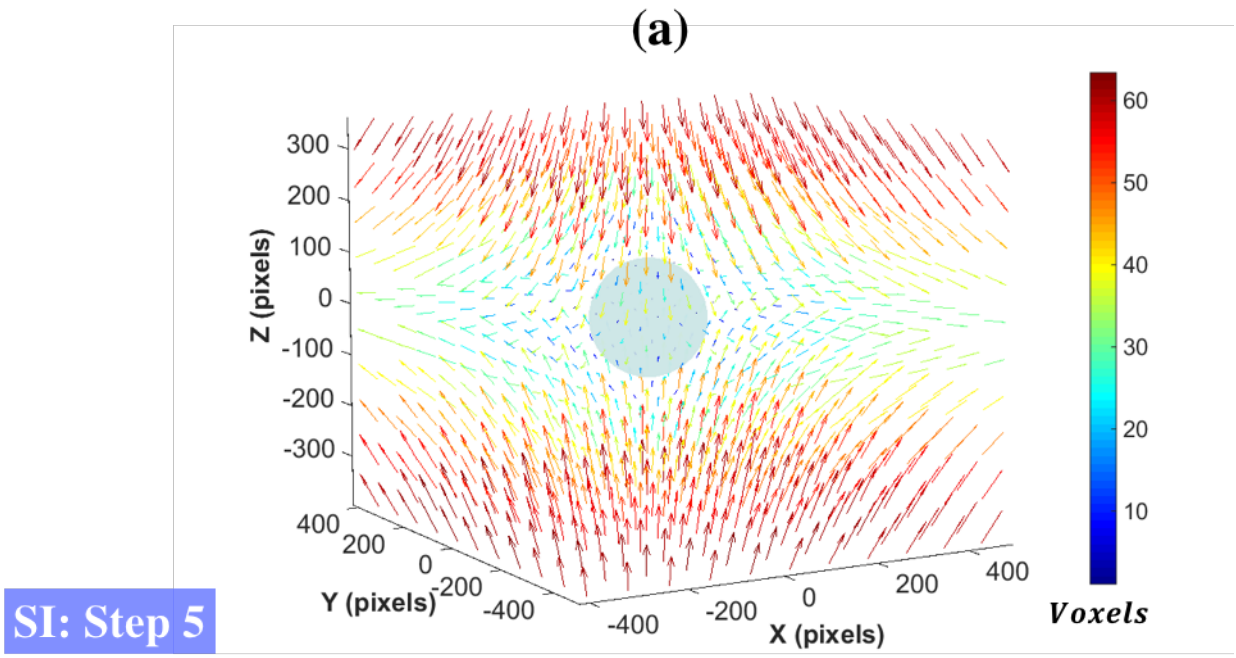

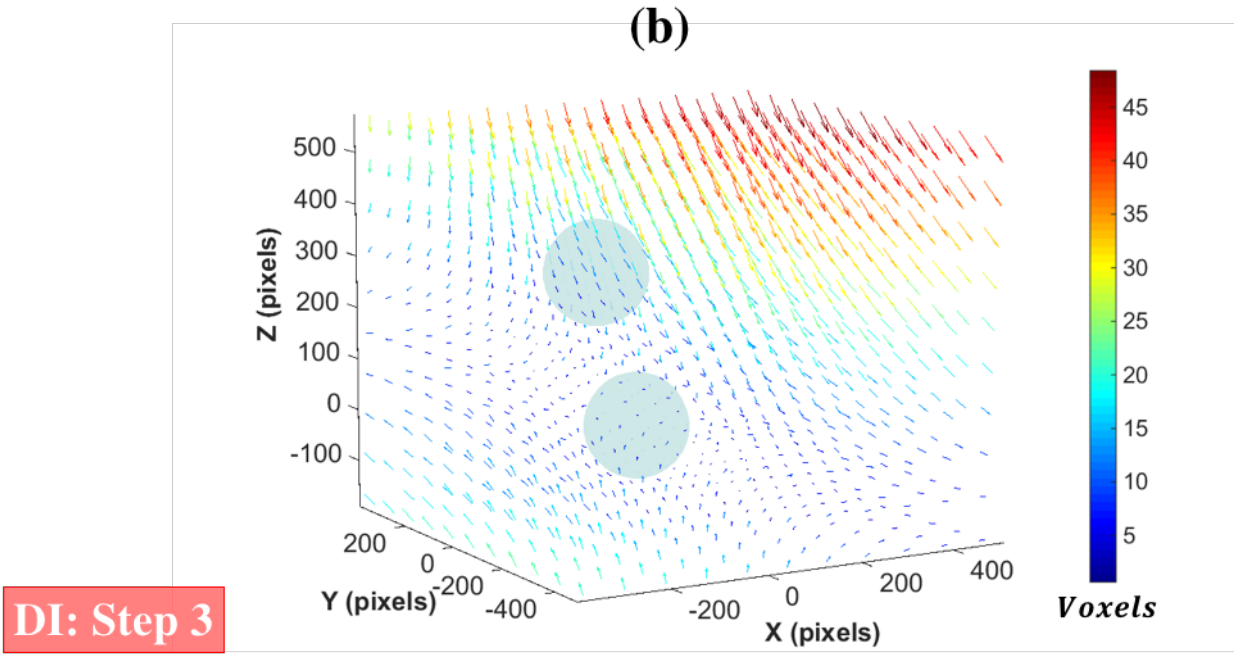

Figure 3.8 Three-dimensional displacement vector field plots of DVC results shown as a 3D quiver plot for single inclusion (black) **(a)** double inclusion (red) **(b)** and randomly distributed inclusions (magenta) (origin inclusion in black and marker inclusion in magenta) **(c)**. Approximately ½ of the total correlation points are shown for clarity. No arrow magnification

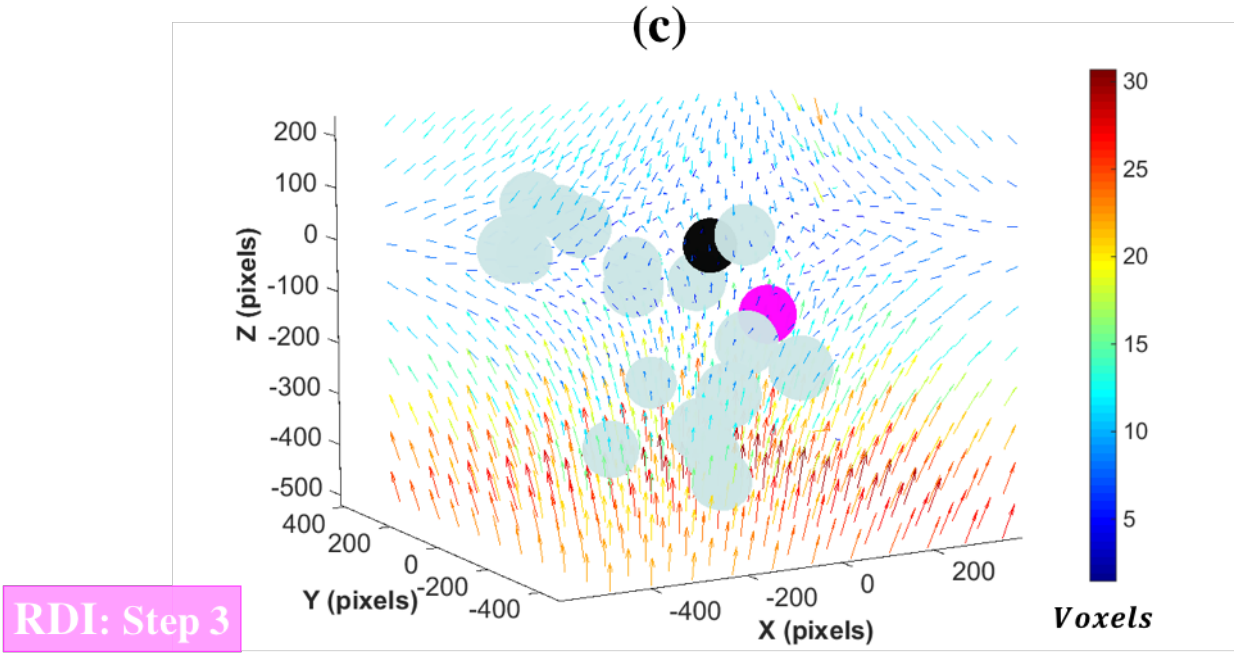

Figure 3.8 (cont.)

3.2.1 Single Inclusion (SI)

The Deben CT500 *in situ* compression stage was used with a displacement rate of 0.5 mm/min to load the SI samples. In this experiment, there were a total of five applied loading steps in increments of 750 μm of cross head displacement up to a total compression of 3.75 mm, as shown in **Figure 3.9 (b)**. The original, or reference, 3D scan was taken at the unloaded state, followed by 3D scans after each applied displacement. The far field applied nominal stress vs strain profile of the SI test (computed as force over cross-sectional area and total change of length/length respectively) is shown in **Figure 3.9 (a)** with each step where a 3D scan was performed labeled as '0', '1', '2', '3', '4', or '5'. After the final loading step of 3.75 mm, the sample was unloaded. The arrows along the curve show the loading profile (upward arrows) followed by the unloading profile (downward arrows). The single inclusion curve (blue) agrees with the single inclusion average established in Chapter 2. A negligible amount of load

relaxation took place during each scan (a scan lasted approximately 45 mins) and is seen as the small load drop at each scan time.

The images below the plots, **Figure 3.9 (c)**, are the cropped 2D *x-y* equatorial plane slices that correspond to a loading/scan step. The images up to step 3 (2.25 mm) appear unchanged but at step 4 (3.0 mm), partial debonding occurred at the interface of the sphere marked with small red arrows. The debonding region, dark in color compared to the matrix (elastomer with embedded marker particles), grew along the direction of the large red arrows, around the entire equatorial plane of the sphere between 3.0 mm (partial debonding at step 4 in) and 3.75 mm (complete debonding at step 5). Here, it was observed that debonding first occurred sometime after 2.25 mm of applied displacement, or ~17% nominal applied strain. Note, the process of debonding may have begun earlier then 2.5 mm of compression (step 3) but was not detectable at the length scale visualized here. A 3D volume rendering of SI, at step 5, in shown next to the 2D slices. Chapter 4 discusses, qualitative and quantitative analysis, of the opening in the single inclusion, that were conducted using ImageJ and Amira.

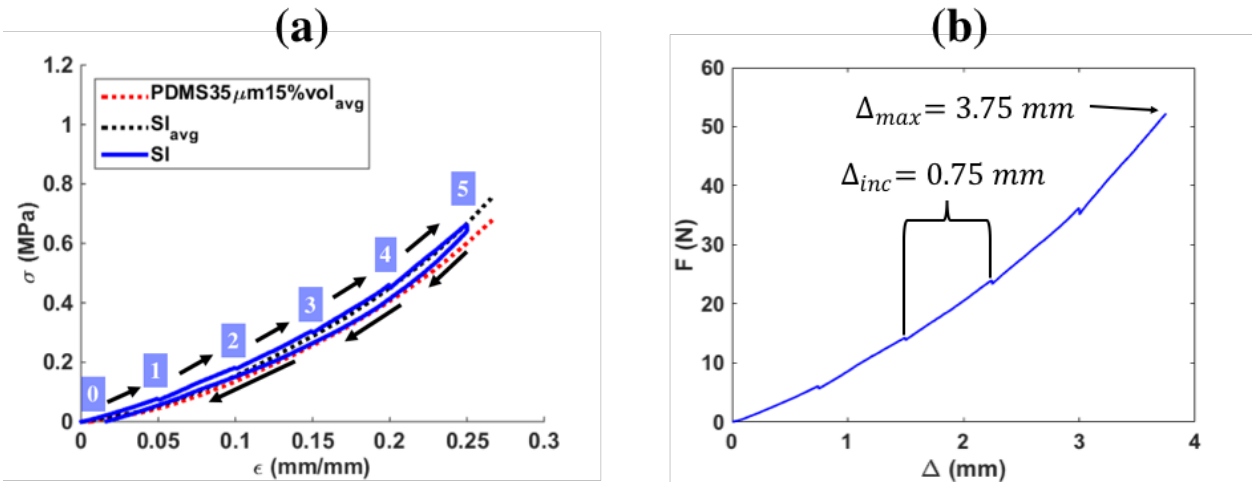

Figure 3.9 (a) PDMS with 35μm glass particles 15%vol (red dashes), single inclusion average (black dashes), single inclusion experiment (blue) stress vs strain curve. **(b)** Loading profile and loading steps between scans. **(c)** The spherical inclusion cropped 2D slices at the sphere equator are displayed with respect to each loading step. Small and larger red arrows denote the observations of partial and complete debonding, respectively.

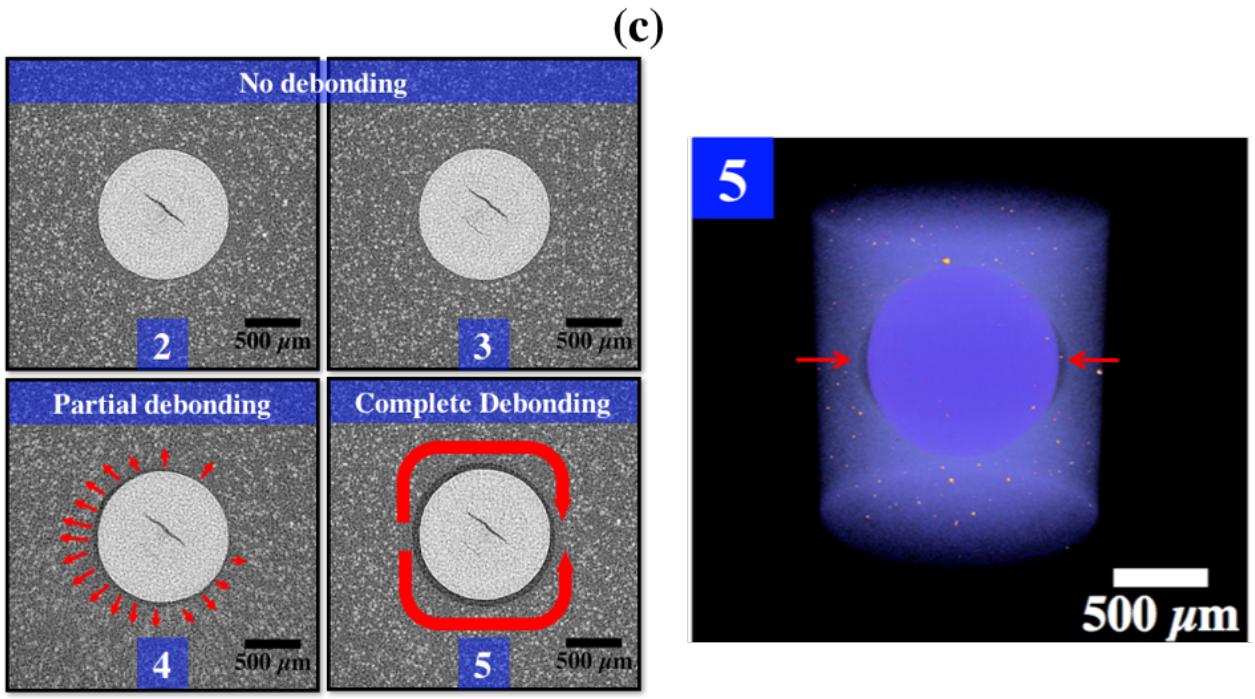

Figure 3.9 (cont.)

The total number of correlation points evaluated here were 56,053. The elastic response occurred in the first three incremental DVC correlations and about ~ 5% or less of the total number of correlation points were subjected to localized smoothing as described in (Gates and Gonzalez et al 2015, Garcia et al. 2010). The elastic response was verified by comparison to the Goodier (1923) solution, which is described in Section 4.1. In addition, the elastic response occurred prior to step 3 and failure was seen at loading steps 4 and 5. Less than 30% of the total correlation points failed to converge due to the large displacements and interfacial failure, which will be discussed in the next chapter. Recall, the additive displacement fields are obtained from summing the incremental DVC correlations. An example of incremental displacement and strain fields at no, partial, and complete equatorial debonding are shown in **Figure 3.10 (a)** and **(b)**. The incremental *w* displacement fields show similar overall behavior regardless of no, partial, or complete debonding. However, the incremental strains fields illustrate the reduction of the low

strain concentration coalesced across the sphere as failure evolves. (Note the bands may be artifacts from DVC). The additive displacement field for the *w* displacement from step 1 to step 5 are shown in **Figure 3.11 (a)** as volumetric contour slices. In addition, the additive displacement field for the *v* displacement at step 6 is illustrated in **Figure 3.11 (b)**. Step 1 underwent displacements in the range between -10 to 10 voxels, step 2 between -20 to 20 voxels, step 3 between -35 to 35, step 4 between -50 to 50 and at step 5 displacements that exceeded -60 to 60 voxels.

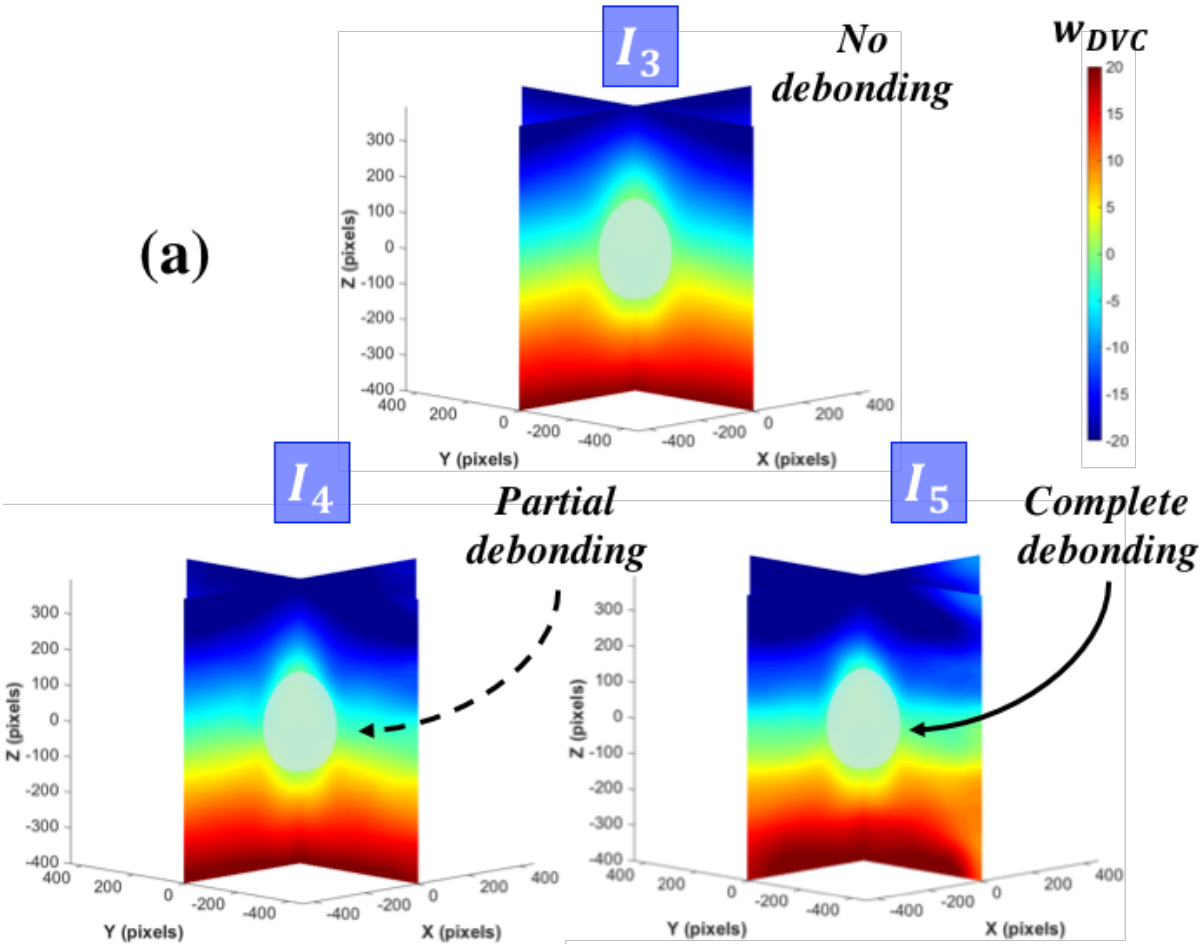

Figure 3.10 Incremental correlated (I_i) w^{DVC} displacements as volumetric contour slices in XZ and YZ, showing internal deformation field around the spherical inclusion displacement loading step 2 **(a)** and 4 **(b)**. Failure occurred between step 4 and step 3. Displacement scale: -20 to 20 voxels. Strain scale: -0.15 to 0

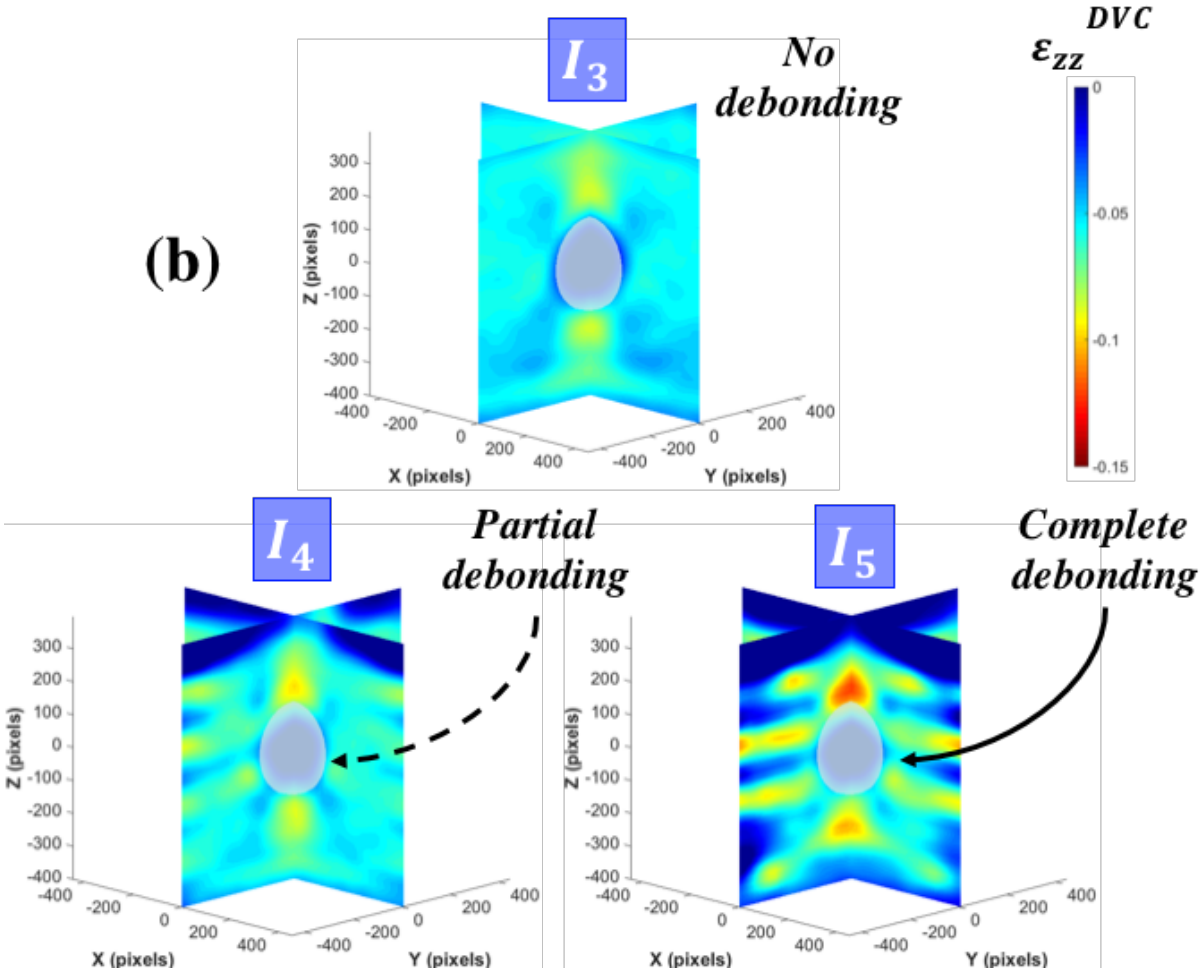

Figure 3.10 (cont.)

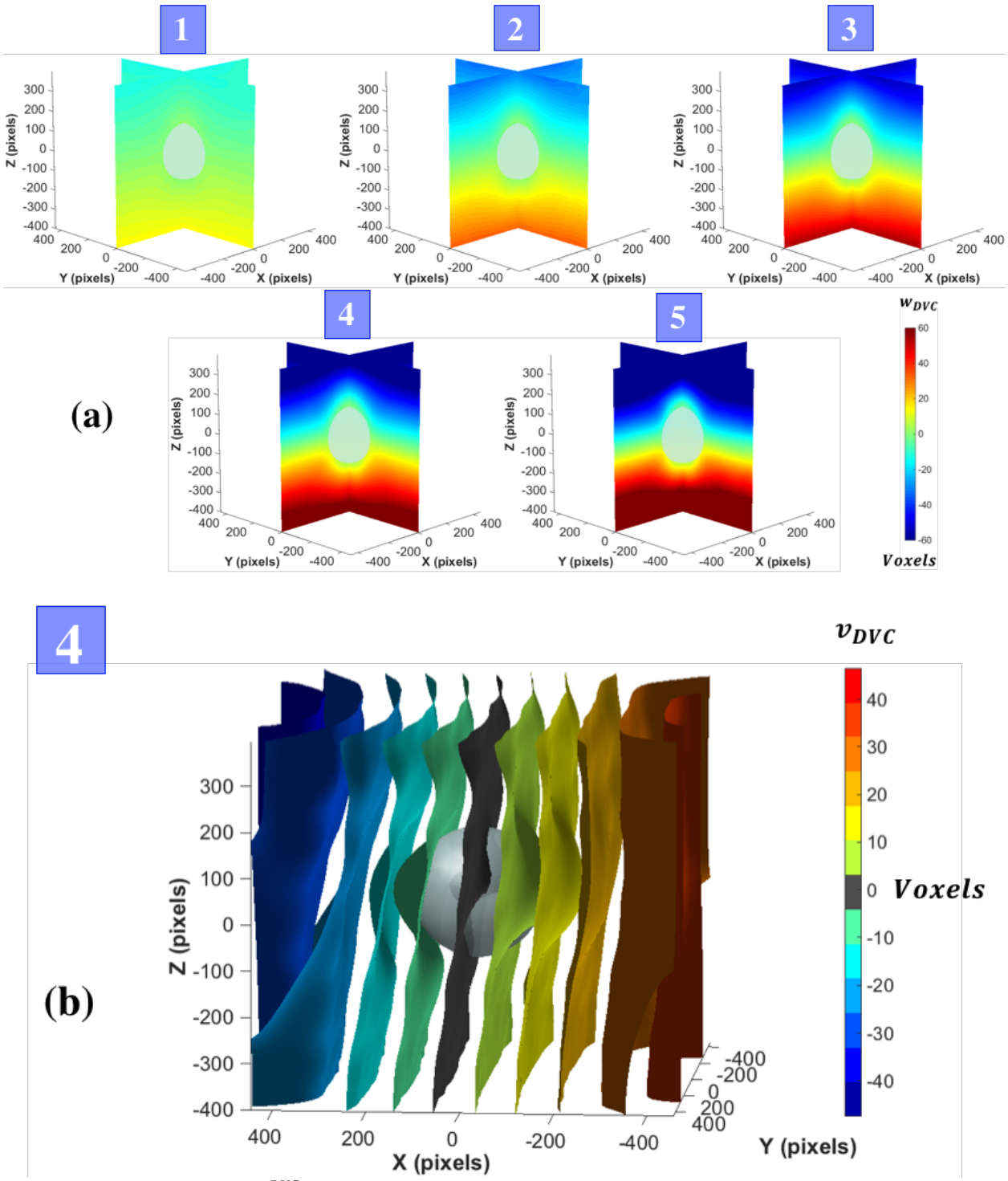

Figure 3.11 Additive w^{DVC} displacements as volumetric contour slices **(a)**, in XZ and YZ, showing internal deformation field around the spherical inclusion at each displacement step (1-5). Failure occurred step 4, and evolved until step 5. Displacement scale: -60 to 60 voxels. Additive v^{DVC} displacements at step 4 as isosurfaces **(b)**, in YZ for constant X values. Displacement scale: -40 to 40 voxels.

To further understand the elastic and failure response, the additive strain fields, ε_{zz}^{DVC}, in the z direction are shown in **Figure 3.12**. The additive strain fields are plotted as volumetric contour slices in the *x*-*z* and *y*-*z* planes at the sphere center and place on a scale of strains from 0 to -0.5 (units: voxel/voxel). At the first loading step, regions with concentrated strains began to develop ranging between 0 to 0.1, or 0 to 10%, with lower strains coalesced along the diagonal directions. As the applied displacement increased from 1.25 mm (step 2) to 2.0 mm (step 3), higher strain concentrations of 15% to 20% emerged at the top and bottom of the sphere. At step 3, the diagonal low strain regions are more distinct and visible. Upon (partial) debonding, at step 4, the strain concentrations above and below the sphere increase to ~33%. While, near the equatorial plane three bands of ~22% strain began to form. As the loading progressed, the strain bands increased and became more visible along the loading axis with strain concentrations as high as 40%. It should be noted that the strain bands may be artifacts of DVC that arise from smoothing the displacements to get strain, hence often the displacement measurements are considered more reliable. Moreover, at step 5 the highest concentrations of strain, from ~45% to 50%, developed at the top and bottom of the sphere. Until step 3, the strain behavior shown depicted the theoretical reported value in literature (Gates et al. 2010, Gates 2011, Goodier et al. 1933). Furthermore, at step 4 and 5, DVC acquired in detail the strain behavior when failure first occurs and as it evolves.

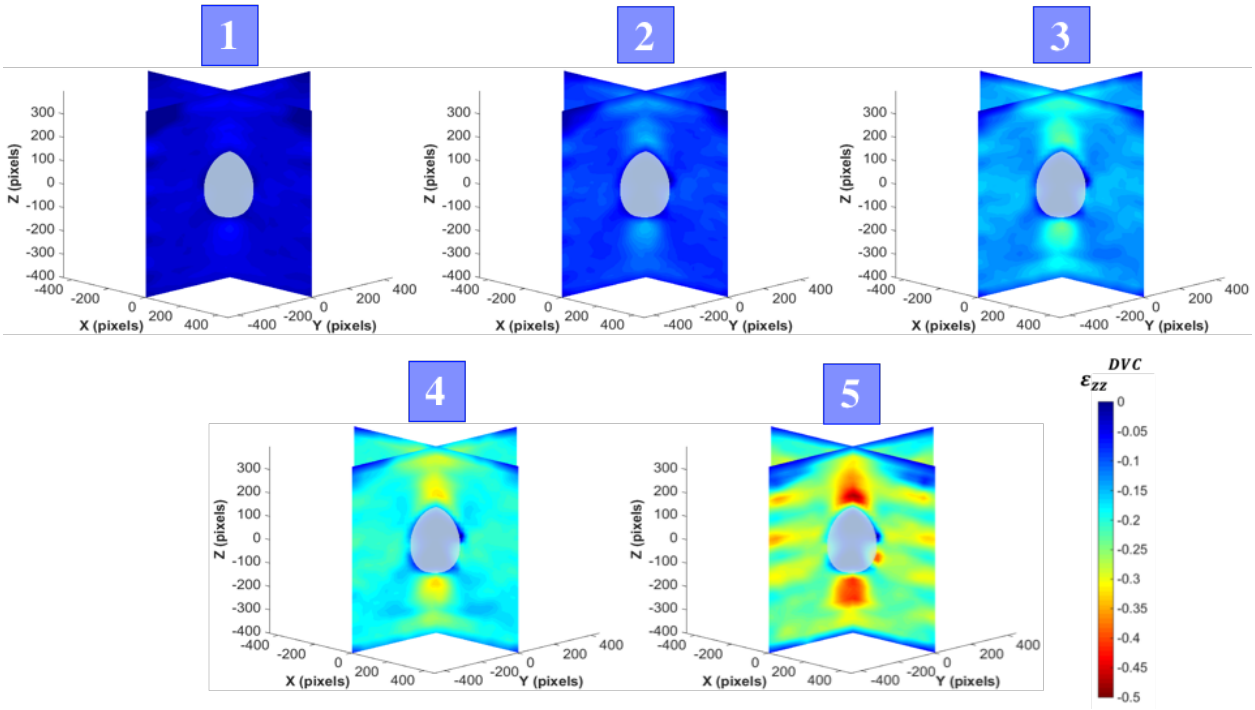

Figure 3.12 Additive ε_{zz}^{DVC} strain fields (in z-direction) as volumetric contour slices, for single inclusion experiment in XZ and YZ planes, at each displacement step (1-5). Failure occurred at step 4, and evolved until step 5. Strain scale: -0.5 to 0.

To determine the effect of the interface on the material response, the surface of an alumina bead was roughened using the technique described in Chapter 2. The applied displacement increment was reduced from 750 μm to 500 μm and the displacement range increased, from 3.75 mm to ~4.3 mm. As a result, there were a total of 10 loading steps. Also, the distance between the source and detector was set to 90 mm and 24 mm, respectively, which resulted in a pixel size of 5.3 μm. **Figure 3.13** compares the far fields stress vs strain curves of the single inclusion (black) and single roughen inclusion (blue) **(a)** and the force-displacement curve on the right **(b)**. By altering the interfacial strength, the material exhibited a stiffer response after a certain loading (about 10% nominal strain) which is attributed to the delay or restriction of debonding resulting from a tougher interface in the roughened sphere case. This is also the load where failure was seen, i.e., sometime between scan 3 and scan 4 in **Figure 3.9**.

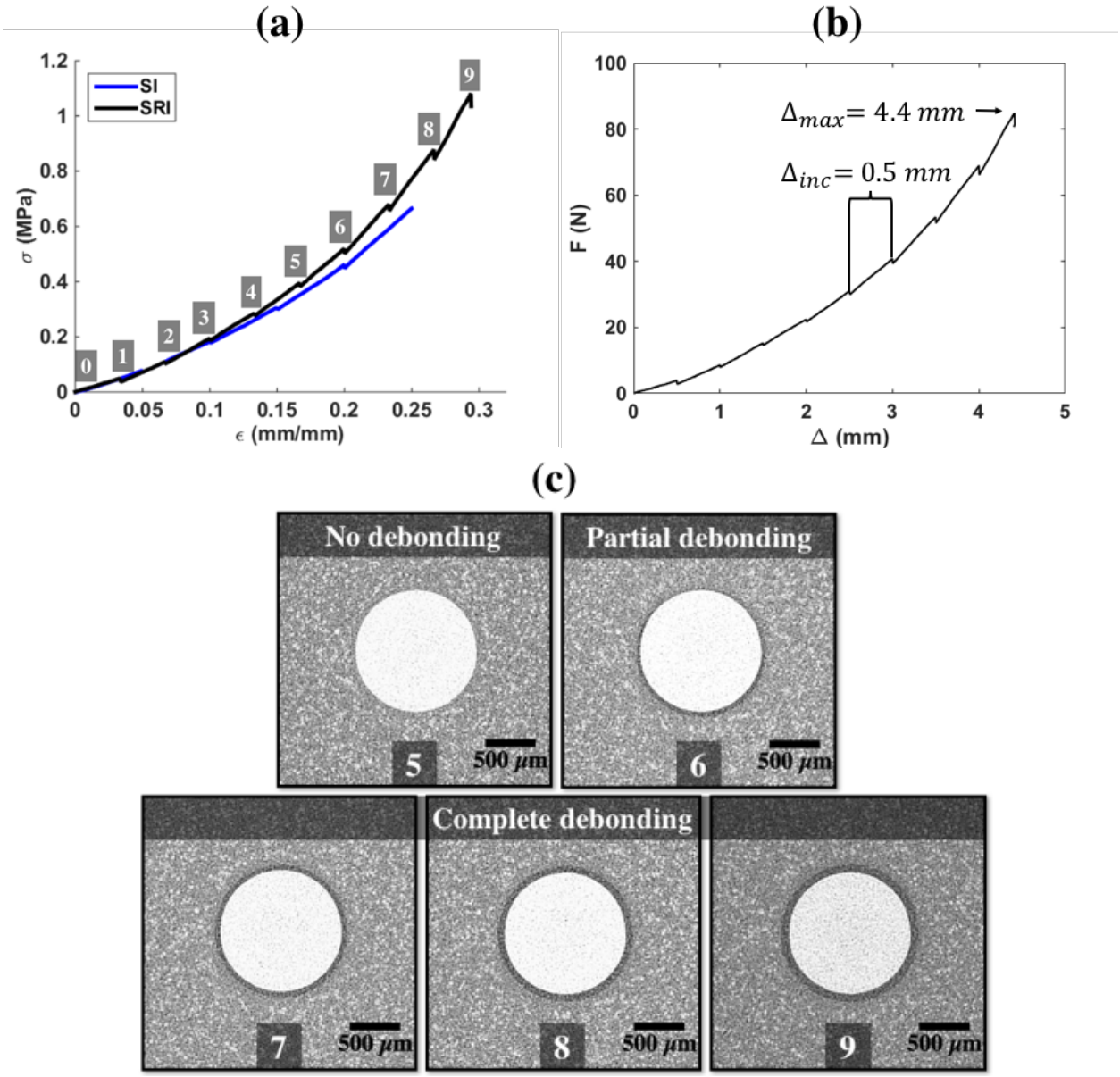

Figure 3.13 (a) Single inclusion (blue) and single roughen inclusion (black) stress vs strain curve. **(b)** Loading profile and loading steps between scans. **(c)** The spherical inclusion cropped 2D slices at the sphere equator are displayed with respect to each loading step at no, partial and complete debonding.

The cropped 2D *x*-*y* plane slices shown above are labeled with respect to their loading step. Up until 2.5 mm of compression (step 5), the slices appear unchanged but at step 6, partial debonding occurred at the interface of the sphere. Here, failure arose somewhere between step 5

(2.5 mm) and 6 (3.0 mm). Note, it is not definite that the roughened inclusion debonded after the as-received alumina inclusion, since the single inclusion could have debonded someplace between 2.5 mm and 3.0 mm (like the roughened inclusion) and not between 2.25 mm and 2.5 mm of compression. The opening in the roughened inclusion slices was distinct by step 6. Like the single inclusion opening after partial failure, the opening grew outwardly and along the equatorial circumference of the inclusion. Here, interfacial failure was captured in 4 scans, one with partial debonding and three with complete debonding. The opening, again dark in color compared to the matrix, reached its maximum deflection/height at 4.4 mm (step 9) of compression. A quantitative comparison of the openings, from the above experiments, was done in ImageJ and Excel. Chapter 4 discusses the effect on the growth and expansion of the opening by the roughened inclusion.

By reducing the displacement increment during loading in this case, a more detail description of the material response, during and after failure, was obtained. The total number of correlations points considered for the roughened sphere case were 55,475. Less than 2% of correlation points failed to converge when failure first occurred (step 5) and as it continued develop. The additive displacement fields from step 1 to step 9 are shown in **Figure 3.14**. The general internal response of the roughened inclusion is similar to that exhibited by the single inclusion in **Figure 3.10**. The additive strain fields as failure progresses are shown in **Figure 3.15**.

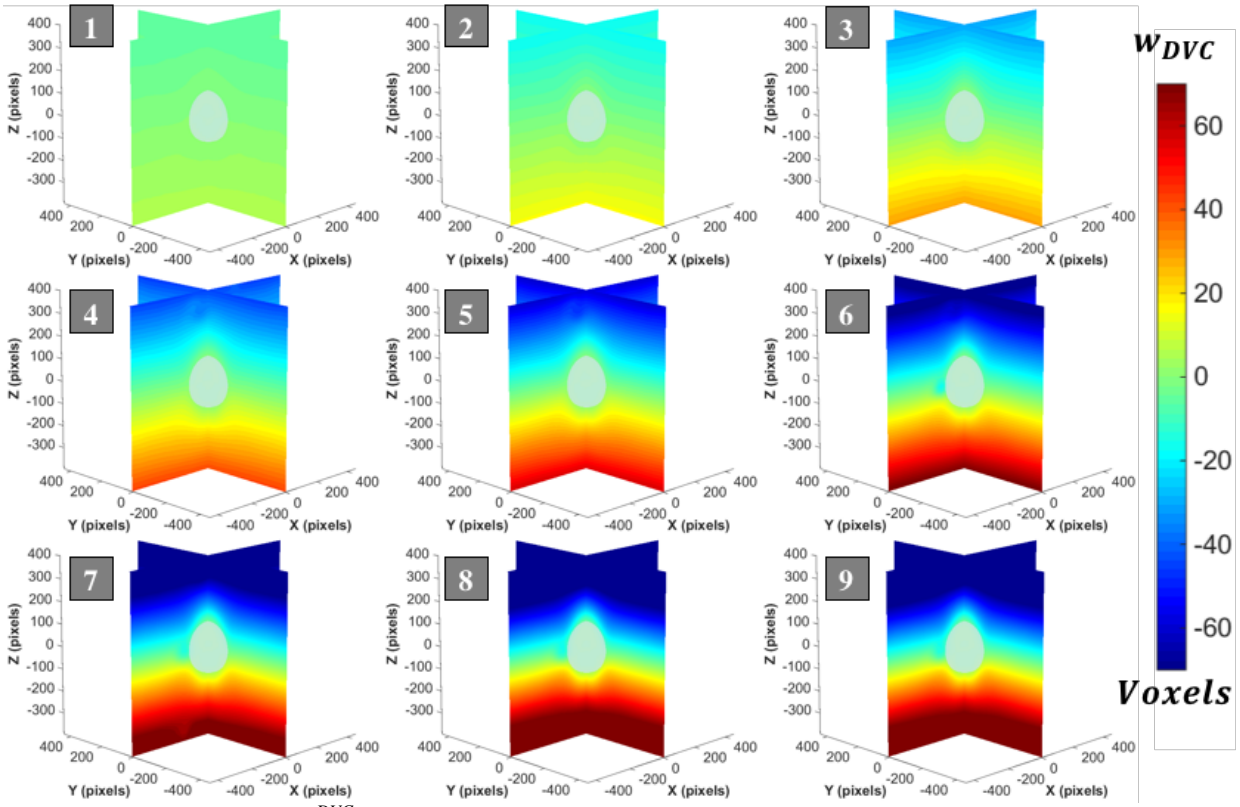

Figure 3.14 Additive w^{DVC} displacements as volumetric contour slices, in XZ and YZ, showing internal deformation field around the spherical inclusion at each displacement step (1-9). Failure occurred at step 5, and evolved until step 9. Displacement scale: -70 to 70 voxels.

The elastic response in terms of strain, ε_{zz}, prior to debonding of the roughened inclusion experiment, step 1 to step 4 shown in **Figure 3.15 (a)**, is identical to the SI elastic response, displayed in step 1 and step 2 of **Figure 3.10**. As before, regions with concentrated strains began to develop at the top and bottom of the inclusion ranging between 0 to 20%, with lower strains coalesced along the diagonal directions. As the applied displacement increased from 2.5 mm (step 4) to 3.0 mm (step 5), the coalesced diagonal strain concentrations diminished and the strain concentrations at the top and bottom of the inclusion grew significantly. After the start of failure, step 6, the strain concentrations above and below the sphere increase to ~33%. Like the SI strain results, the highest strain concentrations occurred at the top and bottom of the sphere. By reducing the displacement increment the evolution, step 5 to step 9, of the high strain regions

became more apparent. The equivalent strain field is shown only for step 4, in **Figure 3.15 (b)**.

Note that in this finer loading step experiment the strain bands at later stages are less prominent.

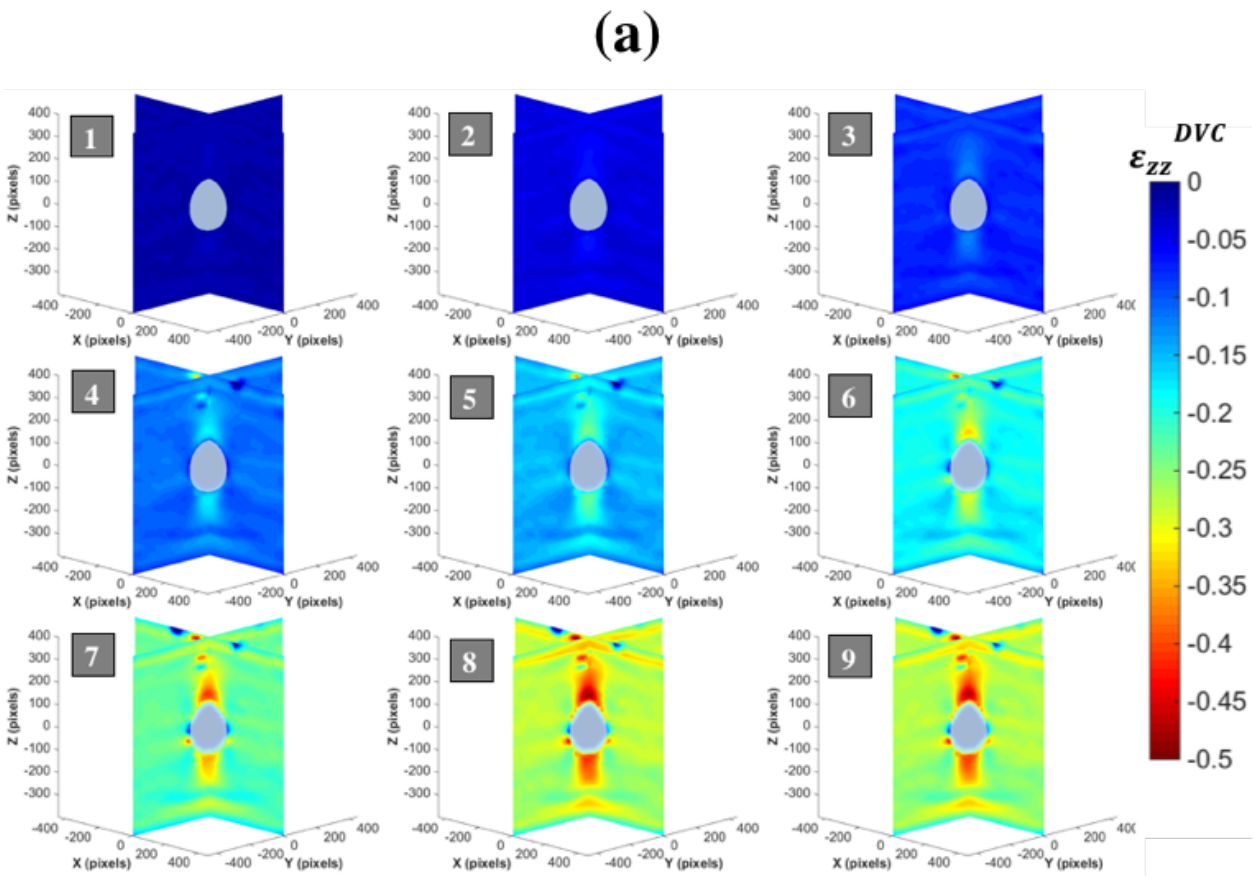

Figure 3.15 Additive ε_{zz}^{DVC} **(a)** and ε_{qq} **(b)** strain fields illustrated as volumetric contour slices, for single roughen inclusion experiment in XZ and YZ planes. The strain fields in the z-direction are shown for each displacement step (1-9) with a strain scale of -0.5 to 0. Failure occurred between step 5 and step 4. The equivalent strain field is shown only for step 4 with a strain scale of 0 to 0.2.

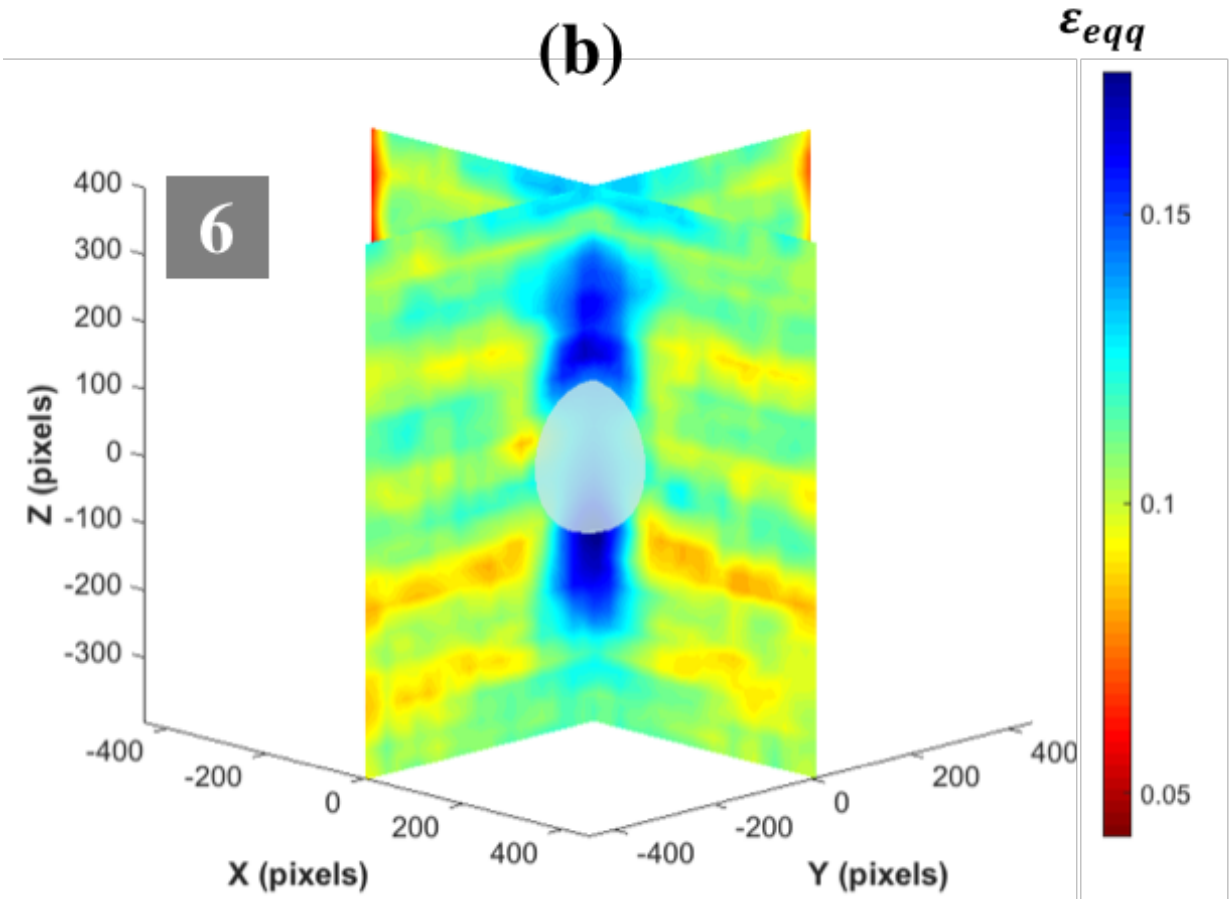

Figure 3.15 (cont.)

3.2.2 Double Inclusion (DI)

To simulate the particle interactions that occur within a particulate composite, a double inclusion sample was manufactured using the procedure outlined in Chapter 2. Again, the Deben CT500 *in situ* compression stage was used with a displacement rate and loading increments of 0.5 mm/min and 0.5 mm, respectively. The maximum amount of applied displacement was 4.3 mm and occurred at the 9^{h} loading step. **Figure 3.16** illustrates that the double inclusion sample was stiffer than both the single roughen inclusion sample and single inclusion sample. The

expected stiffening behavior occurred because of the addition of the second macro-size alumina inclusion which increases the effective elastic stiffness.

The cropped 2D *x-y* plane slices shown above are labeled with their loading step. Up until 2.5 mm of compression (step 5), the slices were absent of the dark region between the matrix and inclusions. However, at step 6 partial debonding occurred at the interface of both spheres. As in SRI, failure arose somewhere between steps 5 (2.5 mm) and 6 (3.0 mm). As in the single inclusion, the opening, after partial failure, grew outwardly and along the equatorial circumference of the inclusions. It should be noted that the top inclusion contains a small defect on the bottom surface of the equatorial plane, seen in **Figure 3.16 (c)**. The top inclusion is not a symmetrical sphere, it contains a small dimple, which affects the shape of the opening. Affecting the outline of the opening was further investigated later by embedding macro-sized irregularly shaped rocks. The interfacial failure was captured in 4 scans and appeared larger around the top inclusion, throughout all compression steps 5 to 9. Section 4.2 discusses a quantitative comparison of both openings, that was conducted using ImageJ and Excel.

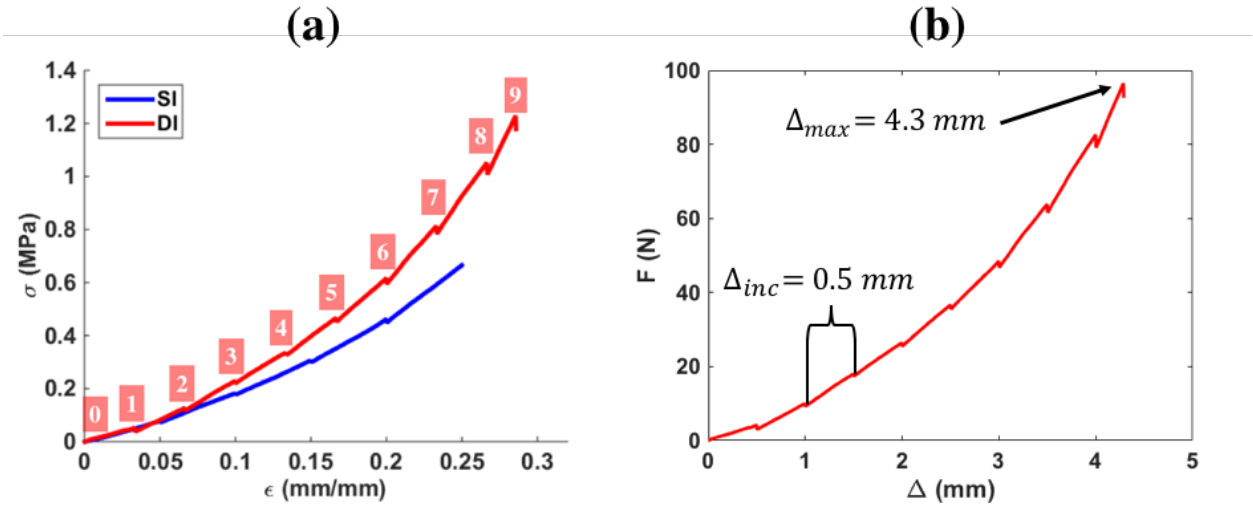

Figure 3.16 Double inclusion (red) and single inclusion (blue) stress vs strain comparison **(a)**. The force vs. applied compression for DI **(b)**. The cropped 2D slices at the sphere equator are displayed for both the bottom and top inclusion, with respect to each loading step at no, partial and complete debonding.

(c)

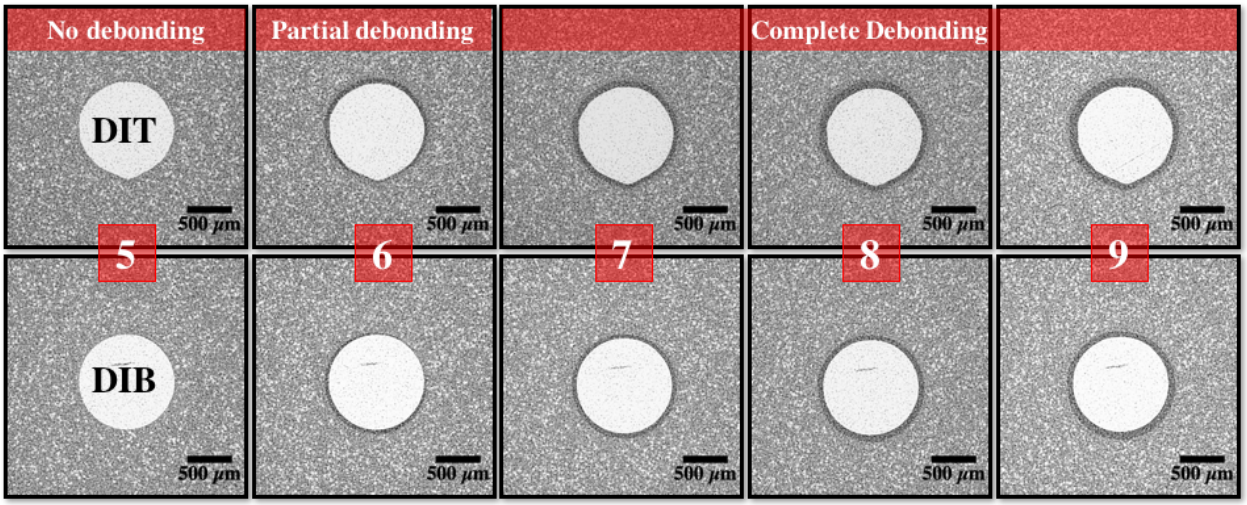

Figure 3.16 (cont.)

A detailed perspective of the displacement and strain fields of the material ligament (i.e., region between the two inclusions), where most of the interaction effects are expected, was obtained by increasing the imaging FOV. To image both inclusions within the same FOV, the source and detector distances were set to 90 mm and 25 mm, respectively, resulting in a pixel size of 5.25 μm. The original and deformed scans were aligned in a way in which only the top inclusion appeared to move; the bottom inclusion was considered the fixed reference. Note, the "fixed reference" can also be set at the midpoint between the inclusions. If this is done the time lapse deformation will illustrate two inclusions converging towards the same point. The measured deformations are plotted relative to the center of the bottom inclusion. The total number of correlation points evaluated were 55,696, less than 3.5% failed to converge. About ~10% of the total number of correlated points were subjective to localized smoothing. Failure appeared at 3.0 mm (step 5) of compression, along the equatorial planes of both inclusions. The additive displacement fields from step 1 to step 9 are shown in **Figure 3.17** as volumetric

contour slices. The largest displacements occurred above the top inclusion. However, the magnitude of displacement decreased to 0 voxels towards the equatorial plane of the bottom inclusion. The top inclusion travelled ~40 voxels when failure first appeared, step 5. By the last loading step, the top inclusion had translated more than 70 voxels along the negative z-direction.

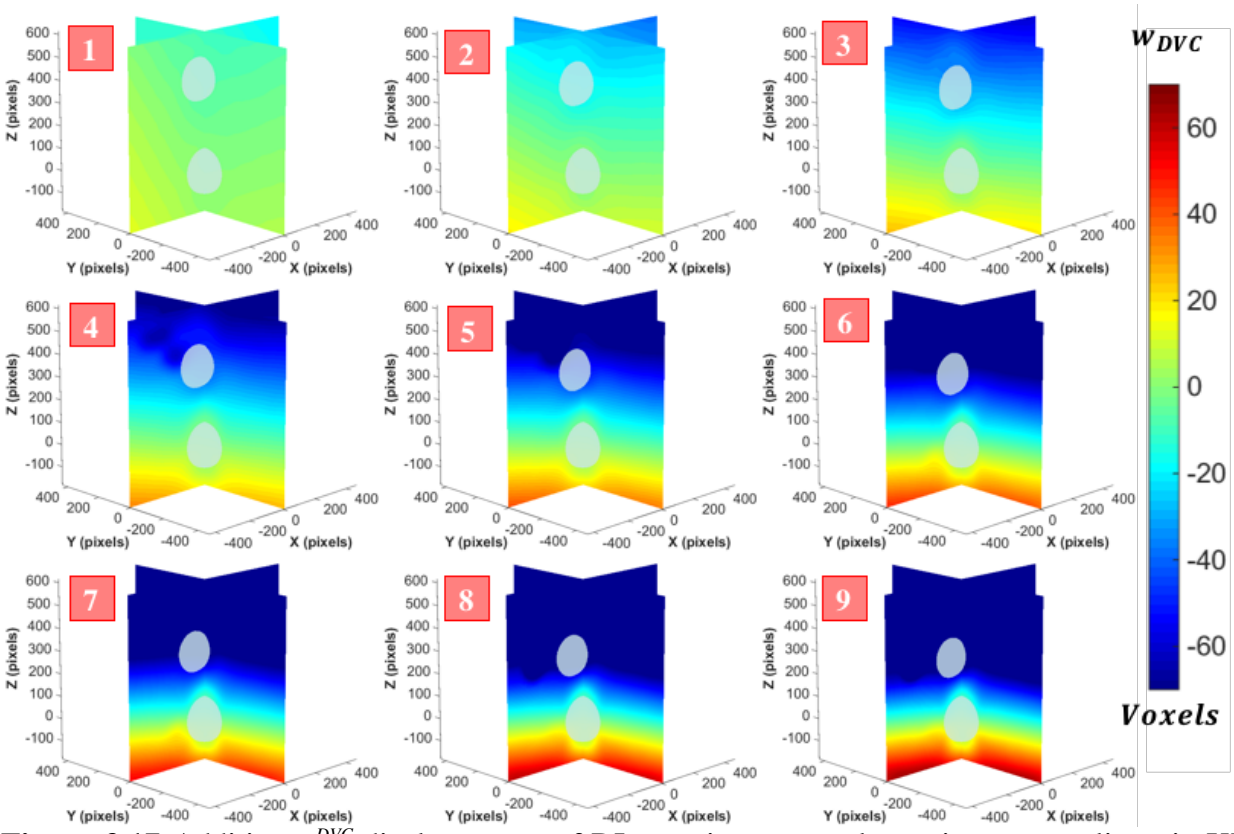

Figure 3.17 Additive w^{DVC} displacements of DI experiment as volumetric contour slices, in XZ and YZ planes. Interaction deformation field, of two-spherical inclusion, is plotted relative to the center of the bottom inclusion. Failure occurred someplace between steps 4 and 5. Displacement scale: -70 to 70 voxels.

The incremental strain fields for loading steps 3, 4 and 5 are shown in **Figure 3.18**. The results illustrated, show the interaction of the strain fields for the particular case (clearly visible in the strain contours connecting the two spheres starting at load level 4. The strain fields illustrate small alterations the strain concentrations around the inclusion relative to failure. In addition, the (additive) strain field evolution with load is shown in **Figure 3.19**. However, the

early DVC strain results seen in **Figure 3.18** and **3.19** can clearly be interpreted as the superposition of two single inclusion strain fields. Thus, the elastic response obtained from single inclusion experiments can be seen from step 1 to step 2 surrounding each individual sphere in **Figure 3.19**. In step 3, the strain concentration between the inclusions began to interact, at ~10% nominal applied strain. Partial debonding arose, at both inclusions, sometime after ~12% nominal applied strain. Both inclusions contained the diagonally coalesced concentration of strain, which is most evident at step 4. By the end of the elastic response, step 4, a large region with a strain concentration of ~17% developed between the inclusions. The region was created because during step 1 to step 3, a small concentration of strain developed, at the bottom of the top inclusion and the top of the bottom inclusion, and connected at step 4. When failure first occurs, at loading step 5, the strain concentration between the inclusions increases to ~30%. Note that at this stage the distance between the spheres, which started out at 2.7 mm (or ~3D, where D is the sphere diameter), has decreased to 1.9 mm or 2D. Similar to the single inclusion strain fields, both the top and bottom inclusion developed strain bands perpendicular to the loading axis. However, these large strain effects may be artifacts of the DVC. Strain concentration between the inclusions continued to increase as failure progressed. At step 9, regions with greater than 45% of strain occurred between the inclusion and above the top inclusion and below the bottom inclusion. The strain concentration within the surrounding matrix varied between ~30% to 42%. Chapter 5 discusses ideas such as the implementation of quadratic shape function, to minimize the observed artificial artifacts.

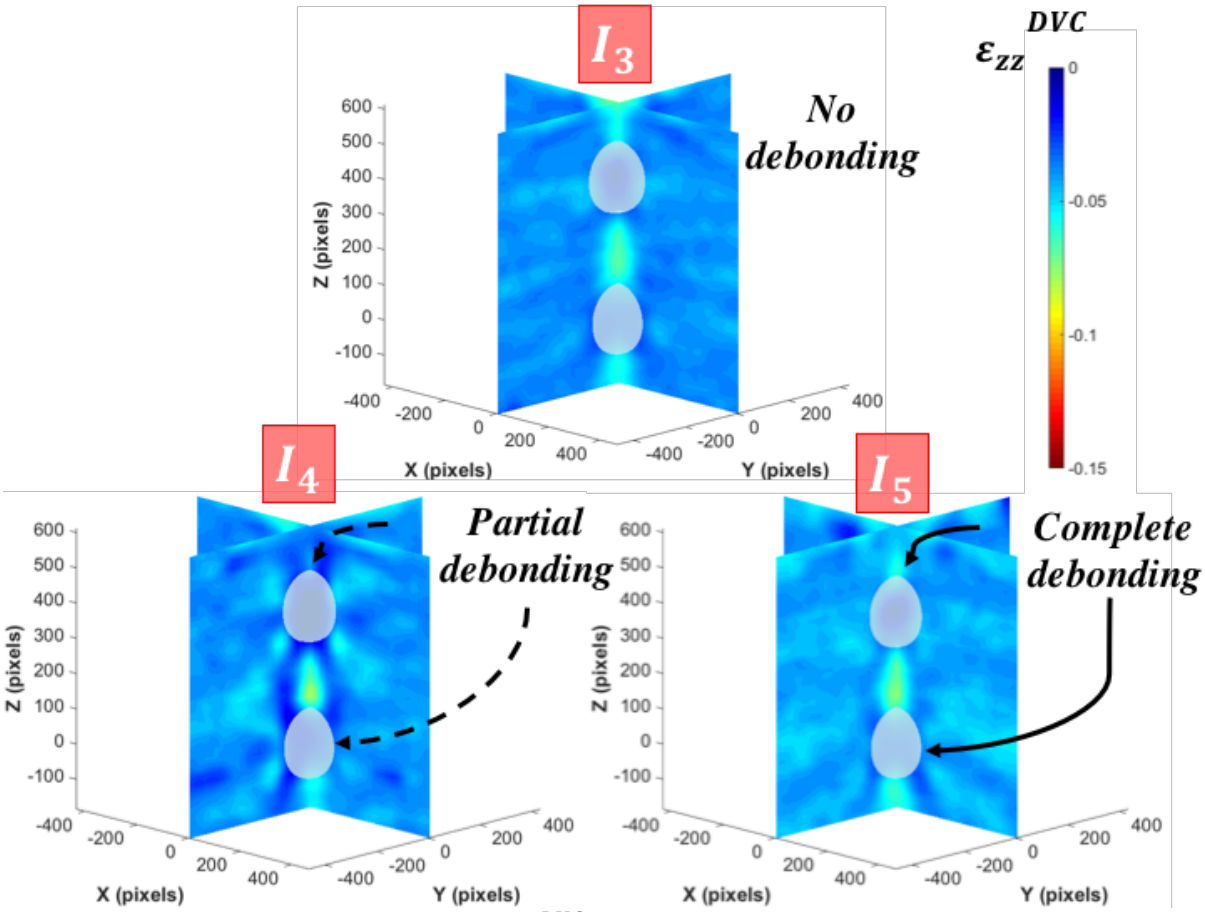

Figure 3. 18 Incremental correlated (I_i) ε_{zz}^{DVC} strain field as volumetric contour slices in XZ and YZ, showing internal deformation field around the spherical inclusions at loading step 3, step 4 and step 5. Failure occurred between step 4 and step 3. Strain scale: -0.15 to 0.

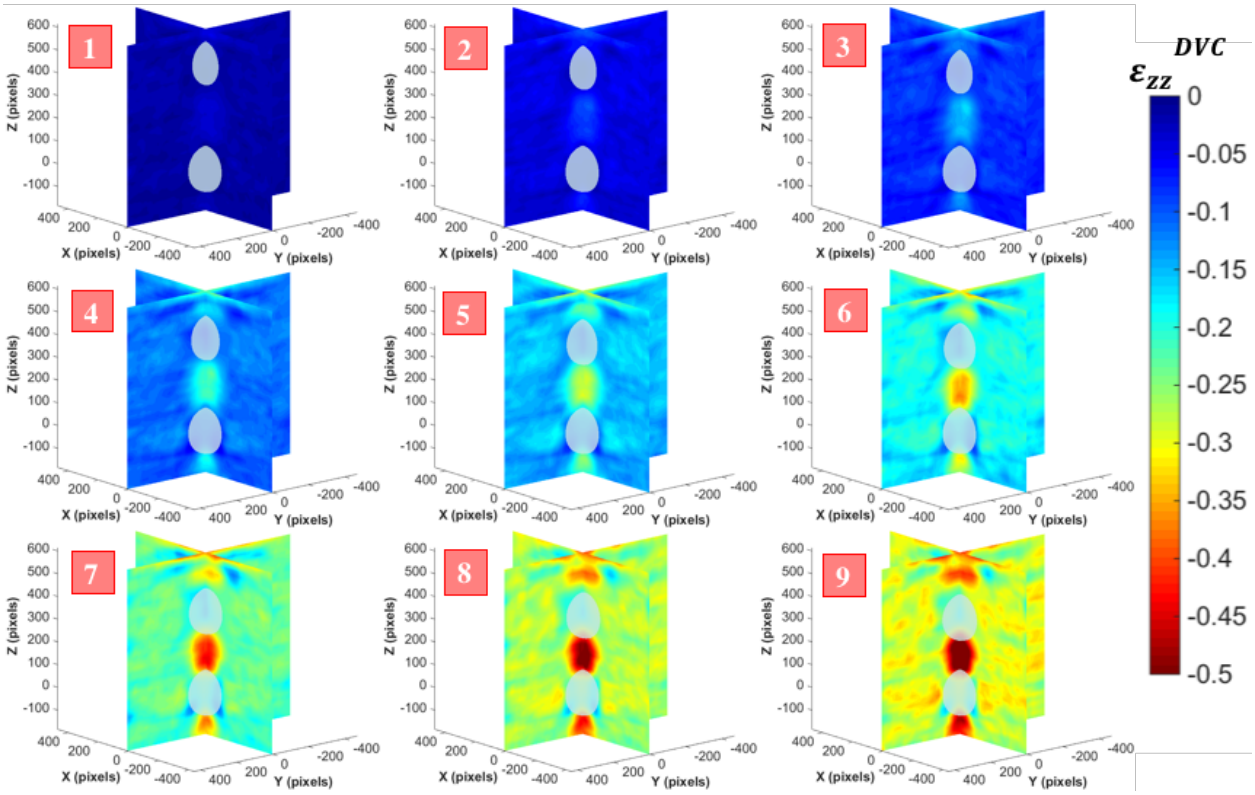

Figure 3. 19 Additive ε_{zz}^{DVC} strain fields (in z-direction), as volumetric contour slices, for double inclusion experiment in XZ and YZ planes, at each displacement step (1-9). Failure occurred between steps 5 and 4. Strain scale: -0.5 to 0.

3.2.3 Randomly Distributed Inclusions (RDI)

The previous results give an illustration of what occurs when two particles interact while being compressed. To study the interactions between more than two particles, a randomly distributed inclusion sample was manufactured and loaded with a displacement rate of 0.5 mm/min. In order to image the entire distribution of inclusions, the source and detector distance of the microCT were set to 90 mm and 44 mm, respectively, which resulted in a pixel size of 4.5 μm. The loading displacement increment was kept constant, 0.5 mm, until step 9. After this loading step, the displacement increment was reduced to 0.2 mm up to an overall maximum applied displacement of 4.7 mm. The reason for the reduction in applied displacement increment

was because the polymer composite became incompressible, i.e., the compression stage reached its load limit (maxed out).

As before, the original or reference scan was taken first at no load. Then a scan was taken after each applied displacement increment while the displacement loading was maintained constant, which resulted in a small amount of stress relaxation while the scanning was taking place. The far field applied stress vs. strain of the RDI compression test (shown in magenta) is compared to the SI and DI curves in **Figure 3.20 (a)**, with numbers again indicating the loading increments where 3D scans were performed. Even though the randomly distributed inclusion has a higher ceramic mass volume fraction than both SI and DI samples it actually showed a more compliant response than the DI sample and was comparable to the SI case. The reason for this is because the RDI sample was cured in a different manner to the other two (on a hot plate as opposed to a convection oven) as detailed in Section 2.1. This resulted in significantly different PDMS matrix properties.

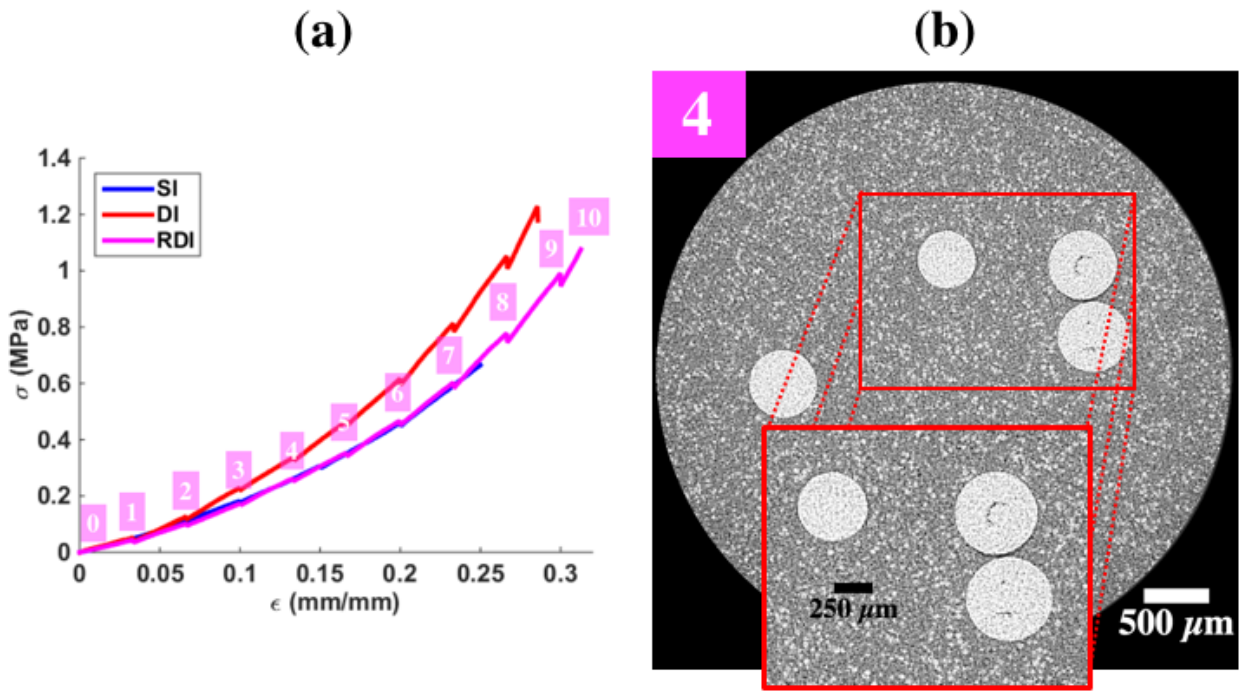

Figure 3.20 Randomly distributed inclusions (magenta) double inclusion (red) and single inclusion (blue) stress vs strain comparison **(a)**. Orthoslice visualization of failure between two inclusion at step 4 **(b)**.

When performing DVC on the RDI sample it should be noted that only the correlation grid points within the 14th inclusion (origin inclusion) were removed and the same correlation grid was used in all the incremental correlations, meaning that some subsets correlated across the inclusions (except the origin inclusion). Nonetheless, DVC was still able to map the deformations between the undeformed and deformed data sets, despite not removing the nodal points within the remaining inclusions. The likely reason why DVC was able to perform the correlations is because the size of the volumetric subset is more comparable to the size of the randomly distributed inclusion. Recall, the inclusions are smaller within the imaging FOV because it was adjusted to capture all 20 inclusions. Therefore, each individual inclusion was smaller in size when compared to the fixed subset size of 41^3, refer to **Figure 3.5**.

The total number of correlation points evaluated in the RDI sample were 41,043 and only less than 11% failed to converge. The total number of correlated points subjected to localized smoothing was between ~8% to ~30% and varied at each incremental correlation. Interfacial failure did not emerge around the 20 inclusions at once. It first arose at 2.5 mm of compression (step 4) in the area between the 9^{th} and 10^{th} inclusions which are very close to each other. Note at step 0, the inclusions were touching. **Figure 3.20 (b)** illustrates that interactions between the 9^{th} and 10^{th} inclusion resulted in two interfacial debondings. Visualizing the equatorial plane of the 20 inclusions at different loading steps is an inefficient way of qualitatively examining the complex failure response in 3D. Section 4.2 details a technique to visualize all openings simultaneously in the complex failure of RDI. The additive displacement fields from step 1 to step 9 are shown in **Figure 3.21** as volumetric contour slices. The displacements exceeded 80 voxels of translation and occurred at the bottom.

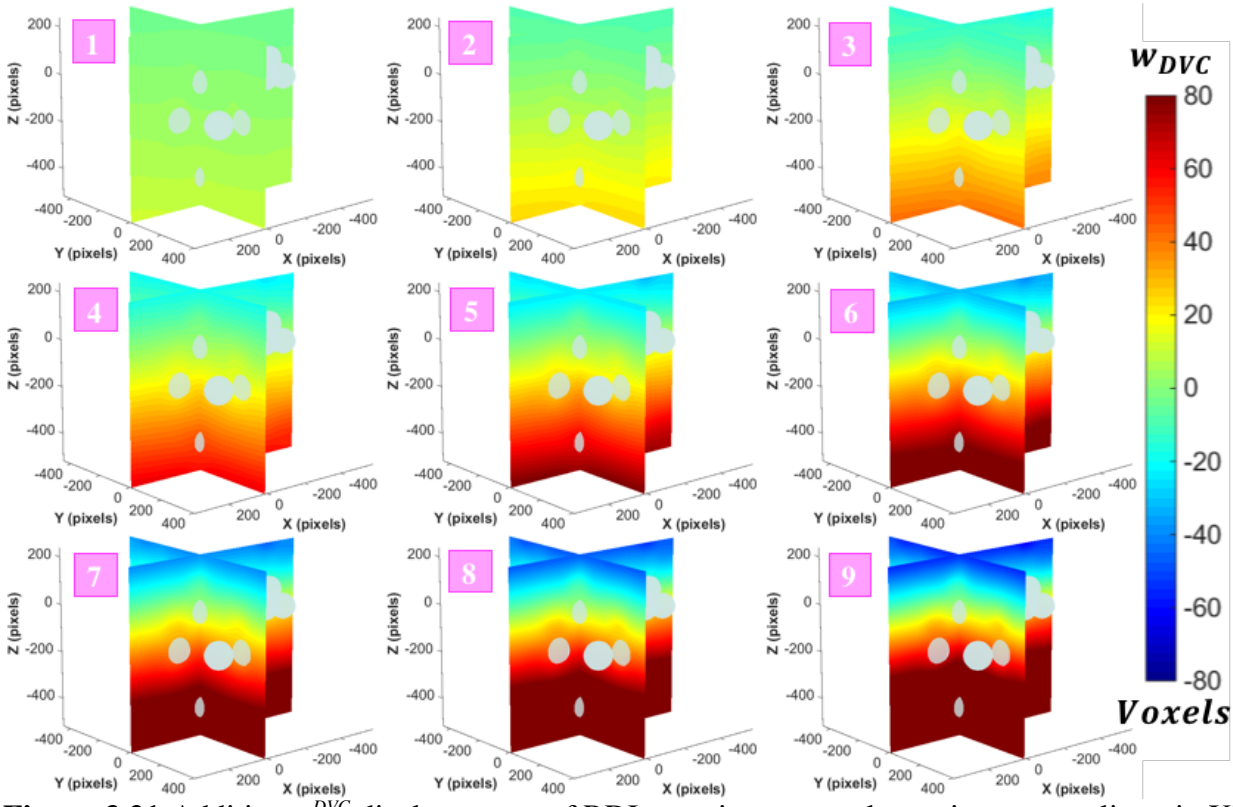

Figure 3.21 Additive w^{DVC} displacements of RDI experiment as volumetric contour slices, in XZ and YZ planes. Failure occurred somewhere between steps 4 and 5. Displacement scale: -80 to 80 voxels.

Although they are quite detailed 3D measurements, the displacement fields, either in the form of a quiver plot (**Figure 3.8**) or as volumetric contour slices (**Figure 3.21**), do not illustrate clearly how the multiple particles interact. Therefore, we also look at the strain field measured in the RDI experiment. The additive strain fields, shown in **Figure 3.22** provide a better description of how the multiple inclusions interact with each other. Similar strain concentrations that developed during the elastic response of the SI (**Figure 3.12**) and DI (**Figure 3.19**), are present from step 2 to step 5. At step 2, the low strain concentration coalesced diagonally across the visible inclusions and by step 5 reached a concentration of ~10%. In step 3, the high strain concentration above and below the inclusions arose and developed a concentration of ~20% by step 5. The individual high strain concentrations, above and below the inclusion, grew enough to

interact with each other at 3.5 mm of compression. By step 9, the interacting strain concentrations accumulated from 35% to 45% strain with a maximum of 50% occurring at the top and bottom of the inclusions.

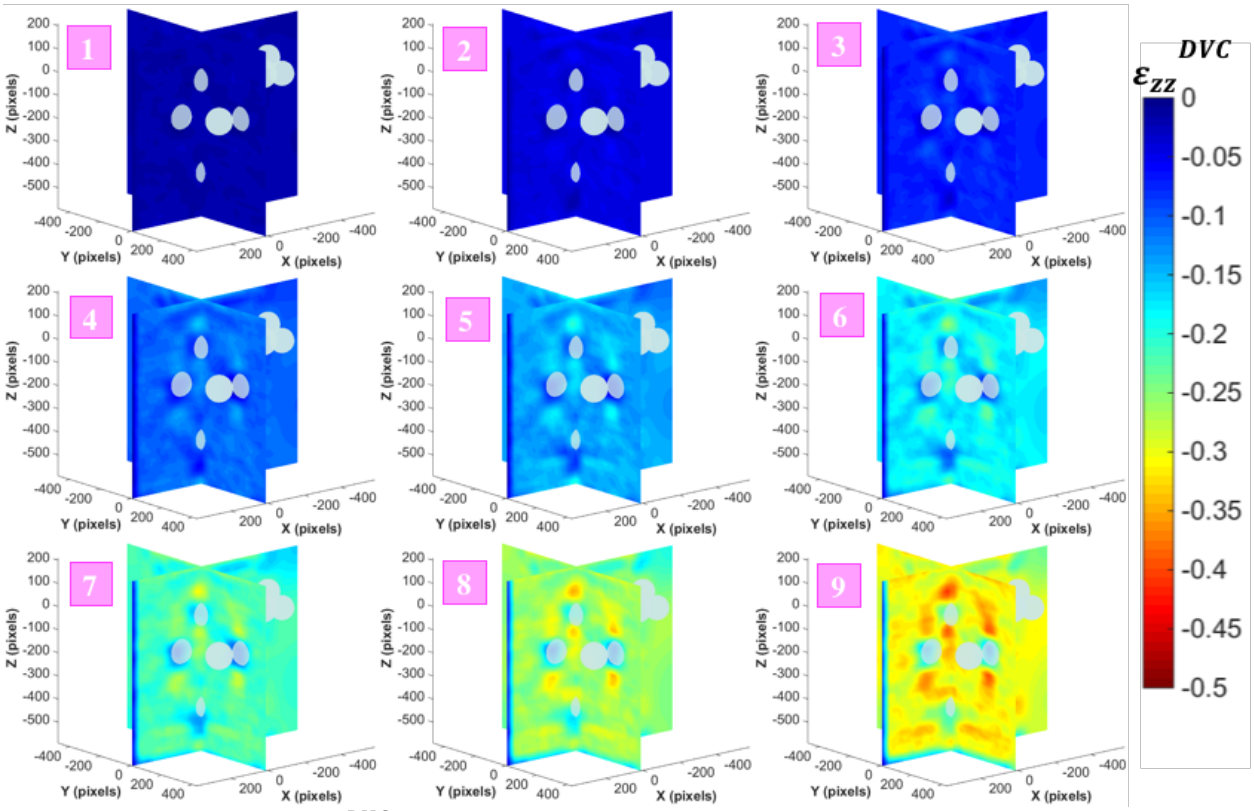

Figure 3. 22 Additive ε_{zz}^{DVC} strain fields (in z-direction), as volumetric contour slices, for randomly distributed inclusions experiment in XZ and YZ planes, at each displacement step (1-9). Failure occurred between steps 4 and 5. Strain scale: -0.5 to 0.

3.2.4 Irregular Inclusion

The use of a sample containing an irregular inclusion was done in order to possibly promote other failure modes to occur, namely particle or matrix cracking. An irregular "sharp" inclusion (VII) made of a rock with flat facets and sharp edges (compared to the spherical inclusion) was aligned almost vertically, i.e., parallel to the loading axis, inside the cylindrical PDMS matrix in hope of inducing possible matrix cracking that would emanated form on the corners or edges of the inclusion. A "rounded" irregular inclusion (RII) of the same rock material

was embedded in the reinforced elastomer to possibly promote failure within the inclusion. Both the vertical irregular inclusion (VII) and the rounded irregular inclusion (RII) were loaded at a displacement rate of 0.5 mm/min and with displacement increments of 0.5 mm. The maximum applied displacement for the VII and RII samples was 4 mm and 4.3 mm, respectively. The nominal stress vs. strain curve for both the vertical irregular inclusion and the rounded inclusion are shown in **Figure 3.23(a)**. The vertical inclusion was stiffer throughout all loading steps. Since, the vertical inclusion was significantly larger, it produced a composite with a higher volume fraction of rock material (assuming the same material properties of the two inclusions).

The cropped 2D *x-y* plane slices shown below are labeled with their loading step and color coded relative to RII (navy) and VII (orange). The porosity of the irregular inclusions is apparent and consistent across their thickness (not shown). The interfacial failure of the irregular inclusions evolved significantly differently than the alumina spherical inclusions. Here, the debonded region was discontinuous, i.e., once a debonded region develop, it did not grow around the equatorial plane of the irregular inclusion. This natural impediment of interfacial failure, is directly related to the surface features of the inclusions. It is difficult to quantitatively study the evolution of the complex failure response in RII and VII. The debonding between the inclusion and the matrix occurs in a particular sequence and at specific locations, indicated by arrows, in **Figure 3.23 (c)** and **(b)**. Chapter 4 discusses the techniques used to visualize the complex failure response of irregular inclusion, an example of RII is shown in **Figure 3.24**.

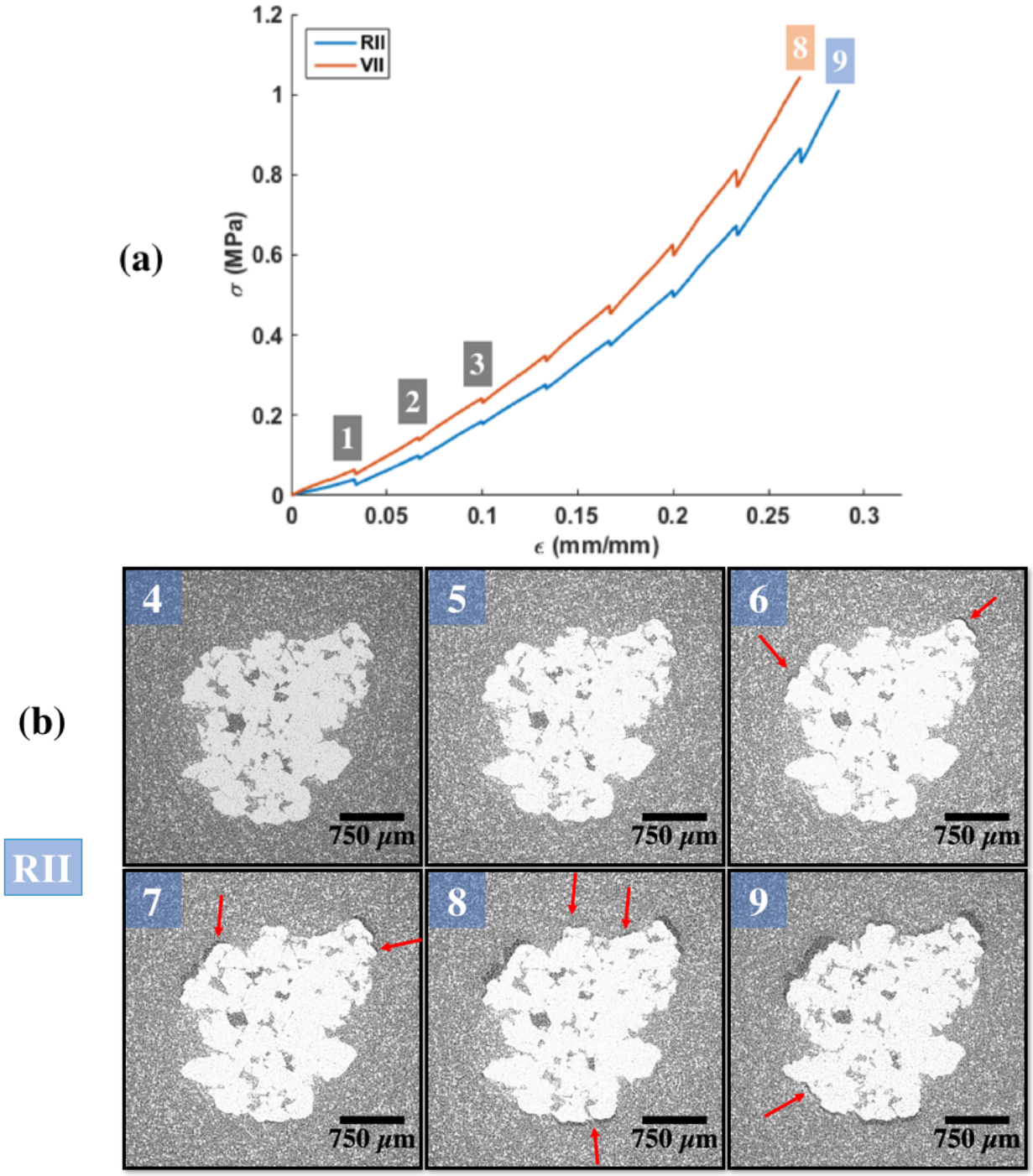

Figure 3.23 Rounded irregular inclusion (navy) and vertical irregular inclusion (orange) stress vs strain comparison **(a)**. The cropped 2D slices at the center are displayed for both the RII and VII, in **(b)** and **(c)**, respectively.

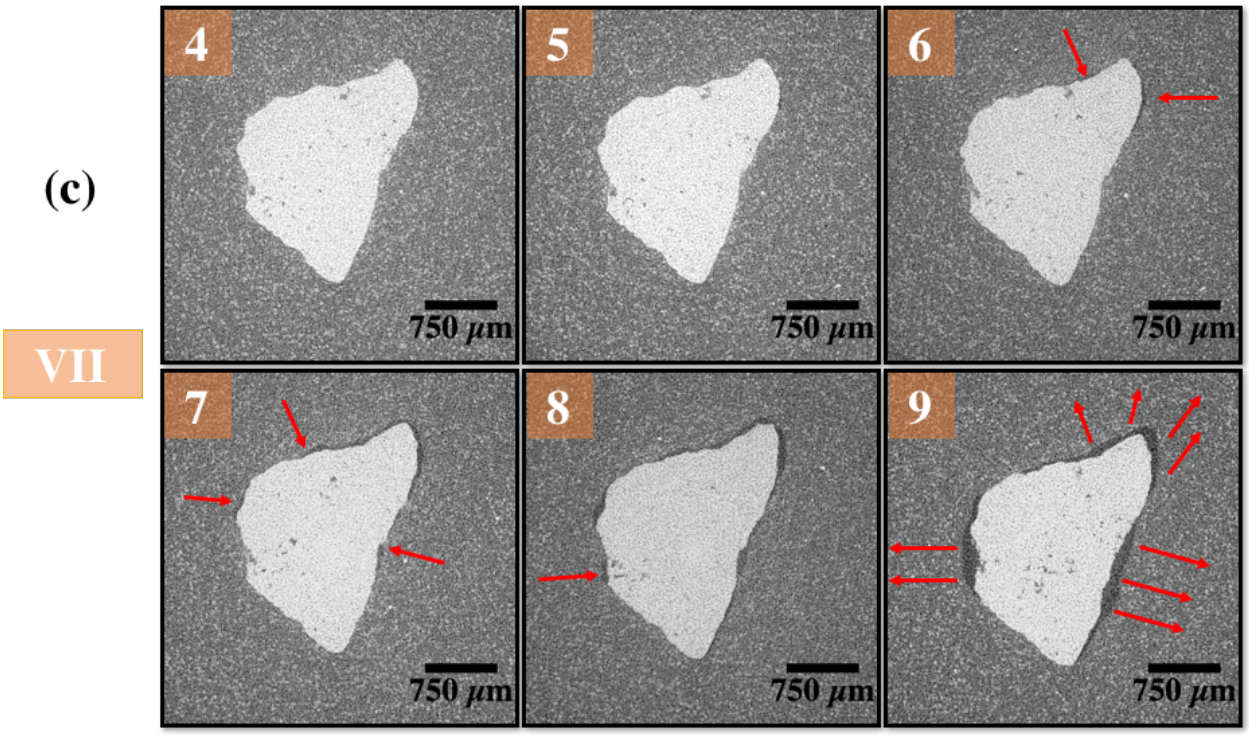

Figure 3.23 (cont.)

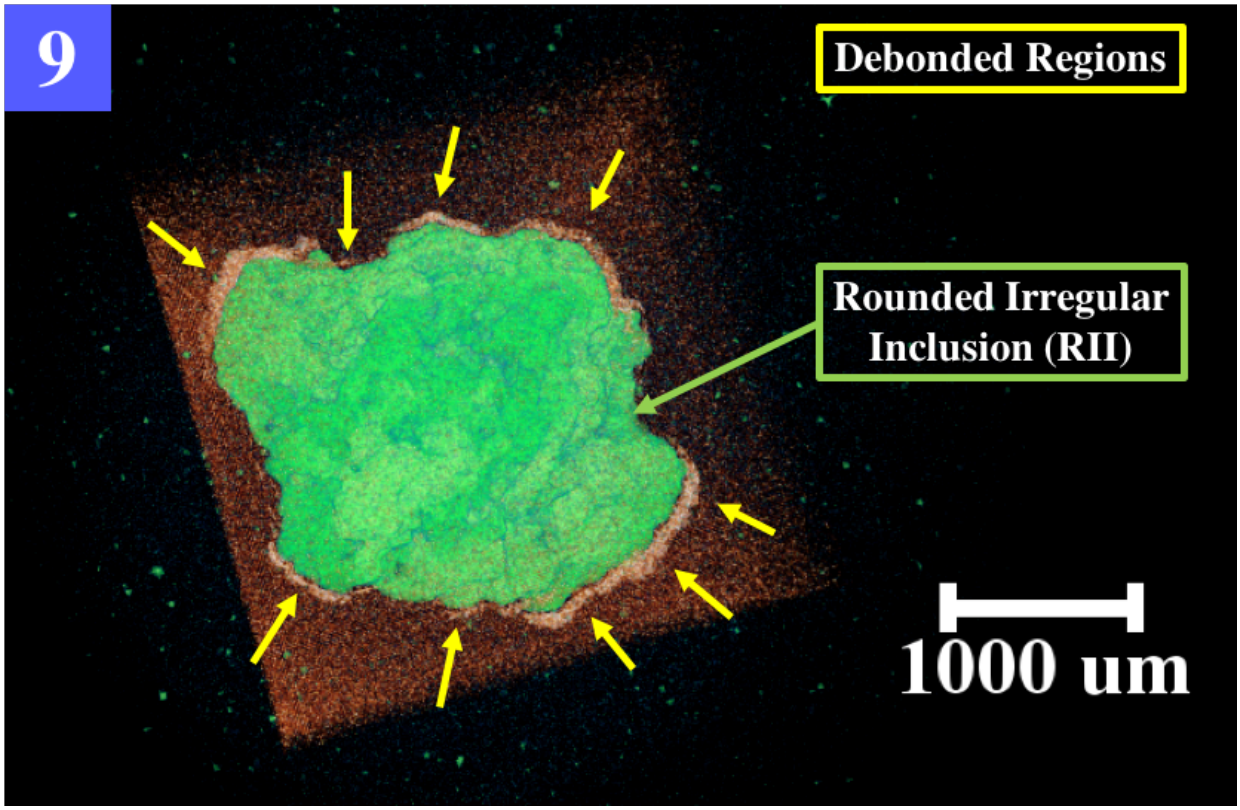

Figure 3.24 Rounded irregular inclusion (RII) complex failure visualization. The asymmetric growth of debonded regions are indicated by the yellow arrows at 4.4 mm of compression. *VolRed* (155 – 120) and *VolGreen* (200-245).

The incremental w^{DVC} displacement field of the vertically irregular inclusion and rounded inclusion are shown in **Figure 3.25** in the form of a quiver plot **(b)** and volumetric contour slices **(c)**. The incremental displacement fields for both the cases were obtained from correlating step 1 with step 2 and step 2 with step 3, respectively. Recall, the removal rigid body motion from the irregular inclusion data sets requires further work. Not being able to minimize the presence of rigid body motion from image data sets, not only increases in computation time, but means DVC measures large artificial deformations, as seen in the displacement vector field of VII, **Figure 3.25 (b).** The incremental correlations were conducted with a *c-target coarse* value of 0.15, instead of 0.1, *c-target coarse* value was increased so that more correlation points would converge. Less than 20% and 3% failed to converge due to larger displacements for the vertical irregular inclusion and rounded inclusion, respectively. Notice that the results are plotted in the image coordinate frame, in other words, the origin is not the center of the inclusion (like SI, DI, and RDI results). To plot the results relative to the center of the inclusion, the meshed surface would have needed to be exported with the center of inclusion being the origin in Amira's coordinate frame. For the correlations to yield proper results, further work to entirely remove both rigid translation and rotation, by aligning precisely the shape of the particle among all data sets, need to be done. Chapter 5 discusses potential ideas for this alignment in 3D space thus providing the rigid translation and rotation corrections needed.

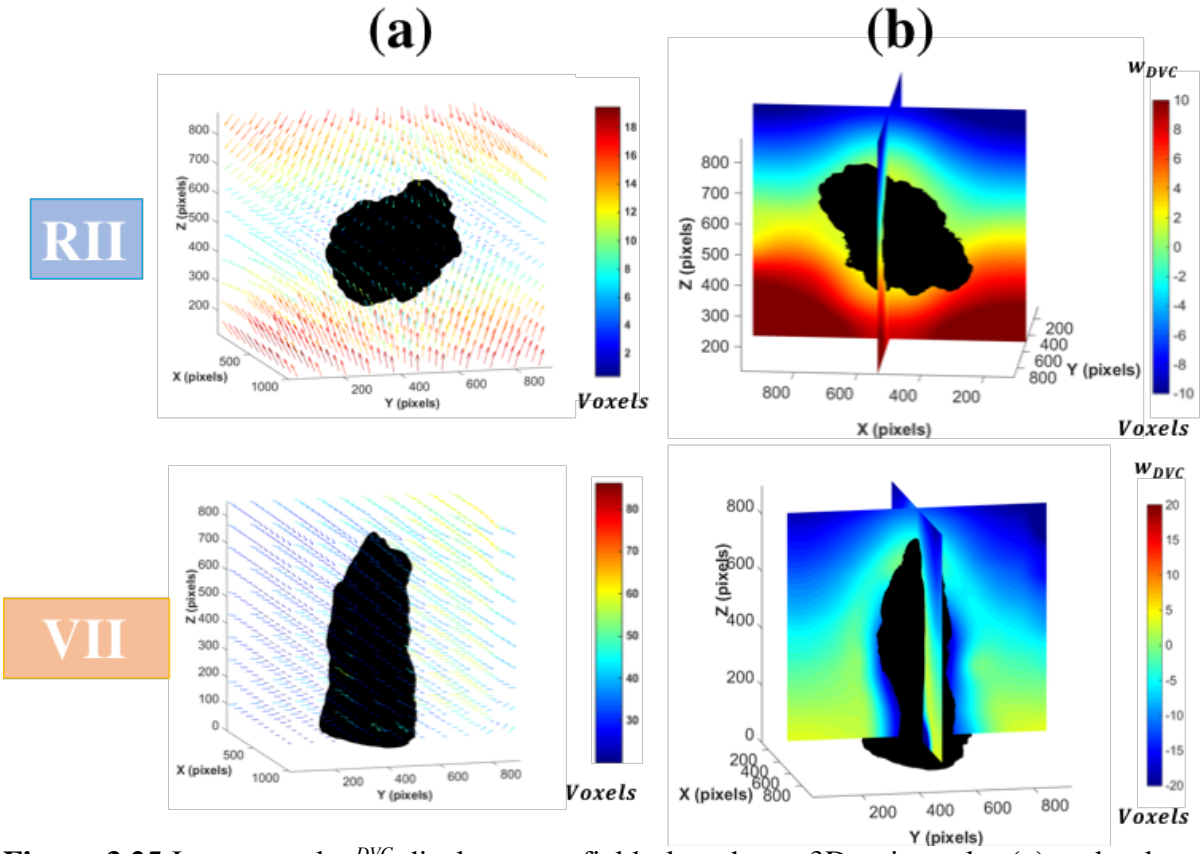

Figure 3.25 Incremental w^{DVC} displacement field plotted as a 3D quiver plot **(a)** and volumetric contour slices **(b)**.

CHAPTER 4: MATERIAL RESPONSE

4.1 ELASTIC RESPONSE

Chapter 3 illustrated the DVC-measured internal deformations taking place during compressive loading in the vicinity of one to several (almost rigid) ceramic inclusions. To validate the DVC method, the single inclusion experimental results were compared to the theoretical displacement field, formulated by Goodier (1933). This theoretical solution provides the displacement field around a rigid spherical inclusion, of radius R, in an infinite linear elastic matrix subjected to a uniaxial far-field tension **T**, as shown schematically in **Figure 4.1**. Although the theoretical solution provides the displacement field around a sphere in an infinite medium, it was used as a starting point to compare with the results obtained from a finite medium, i.e., the cylinder used in our experiments, since the diameter of the cylinder was 10 mm and the inclusions diameter was 1 mm.

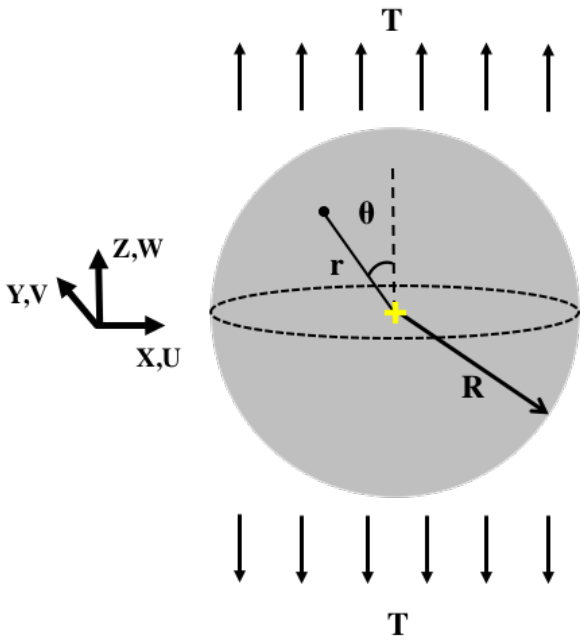

Figure 4.1 Spherical inclusion within a medium under uniaxial tension. For the case of compression, the applied traction, **T**, is set to be negative.

The three-dimensional displacement components in spherical coordinates are (Goodier et al. 1933),

$$
\begin{aligned}
u_r &= -\frac{A}{r^2} - \frac{3B}{r^4} + \left[\frac{(5-4\nu)}{(1-2\nu)}\frac{C}{r^2} - \frac{9B}{r^4}\right]\cos 2\theta \\
&\quad + \frac{Tr}{2E}\left[1-\nu+(1+\nu)\cos 2\theta\right] \\
u_\theta &= -\left[\frac{2C}{r^2} + \frac{6B}{r^4}\right]\sin 2\theta - \frac{Tr}{2E}(1+\nu)\sin 2\theta \\
A &= -\frac{TR^3}{4\mu}\left[\frac{1-\nu}{1+\nu} + \frac{3}{16-20\nu}\right] \\
B &= -\frac{TR^5}{8\mu(8-10\nu)} \\
C &= -\frac{5TR^3(1-2\nu)}{8\mu(8-10\nu)}
\end{aligned}
\tag{4.1}
$$

where r is the distance from the center of the sphere to an arbitrary point, θ is the angle from the positive z-axis, tension T is applied parallel to the z-axis, and ν is the Poisson's ratio, E the Young's modulus and μ the shear modulus of the surrounding matrix. For the Poisson's ratio value, an *in-situ* compression test was performed on a PDMS35 μm-15%vol. sample, with a spatial resolution of 4 μm/pixel. A brief description of the experiment and findings are described below (Gonzalez and Lambros 2016). A displacement rate of 0.5 mm/min was used there for two different applied displacements, 0.8 mm and 1.5 mm. DVC correlations were evaluated with the same subset and step size as the prior correlations here. The measured displacements from the DVC algorithm were used in a least-square fit to obtain 3D strains. Using the 3D strains, which were uniform throughout the uniaxially loaded sample, the Poisson's ratio was measured from the average axial (ε_z) and transverse (ε_x) strains as $\nu = -\varepsilon_x/\varepsilon_z$. A measured ratio of 0.5 was determined compared to the literature value of for PDMS of $\nu = 0.49$ (Lotters et al. 1997). Note however that the value obtained in Gonzalez and Lambros (2016) is for the PDMS marker

particle mixture rather than pure PDMS. In this work, we will take the Poisson's ratio value as 0.49. Subsequently, the applied traction, **T**, can be determined from the stress-strain data from the experiment (see **Figure 3.9**).

The Young's modulus value to be used for the "matrix" in Equation 4.1 needs to also incorporate the reinforcement effects on PDMS of the embedded 35 μm-15%vol. particles. This value was also experimentally determined but from the samples tested in Chapter 2. **Figure 2.10 (a)** shows the far-field stress-strain response of 5 samples along with the average curve of all 35 μm-15%vol. samples tested from which the average Young's modulus was computed to be 2.09 MPa – larger than the Young's modulus determined for PDMS of 1.8 MPa (Choi et al. 2003). With this value, and those discussed earlier, the theoretical displacement field prediction can be generated using Equation 4.1 for each (r, θ) coordinate point from the set of DVC correlation points so that a direct comparison can be made between DVC-measured displacements and theory.

The Goodier solution detailed above does not account for interfacial failure. This means that the theoretical solution can at best be only valid for loads prior to the onset of debonding, termed forthwith *low loads*. **Figure 4.2** shows a comparison between the incremental w^{DVC} displacements (solid lines) with the theoretical one (dashed lines) at **(a)** step 2 and **(b)** step 4 at the spherical center in *x-z* plane (step numbers correspond to the loads shown in **Figure 3.9**). Recall, 2.5 mm (step 2) of compression was applied without debonding being observed, while at step 4 partial debonding developed. As seen in Figure 4.2, the experimental vs. theoretical contours match more closely for step 2 than for step 4, with a significant deviation between the two seen at step 4 at the location where the partial interfacial failure was observed (upper half of the inclusion as seen in **Figure 4.2**).

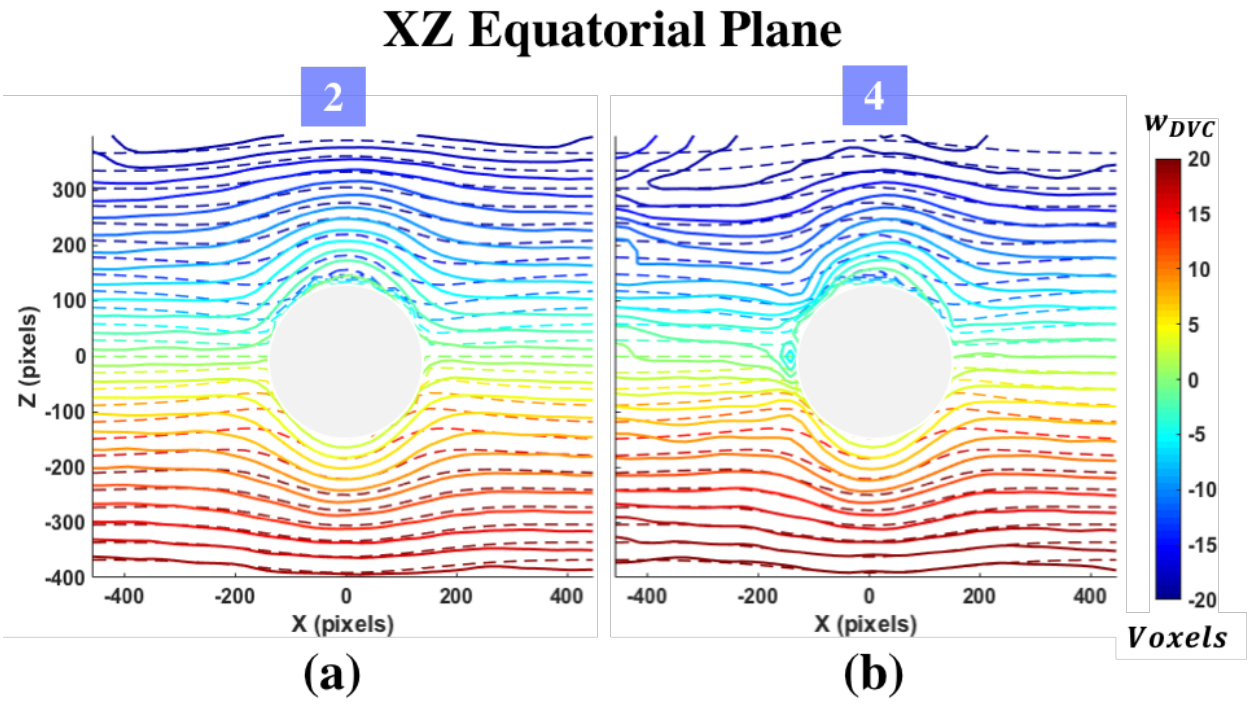

Figure 4.2 Comparison of raw incremental w^{DVC} displacement fields (solid lines) vs. the Goodier solution (dashed lines) for **(a)** step 2 and **(b)** step 4, when partial debonding occurred.

The comparison above was made using the incremental values. However, it can also be made using additive results, which is described below. The raw additive w^{DVC} displacement fields from step 2 (solid lines) are compared with Goodier's solution (dashed lines) in **Figure 4.3**. The left plot **(a)** illustrates the displacement at the sphere center in *x-z* plane. The comparison illustrates that the experimental displacements agree well within the *2R* areas, with less than a 10% error. While the right plot **(b),** is the displacement field 268 voxels away from the sphere center, outside of the {*-2R, 2R*} domain. Here, the experimental displacements match better, with a discrepancy of ~4% and are close to a uniform field.

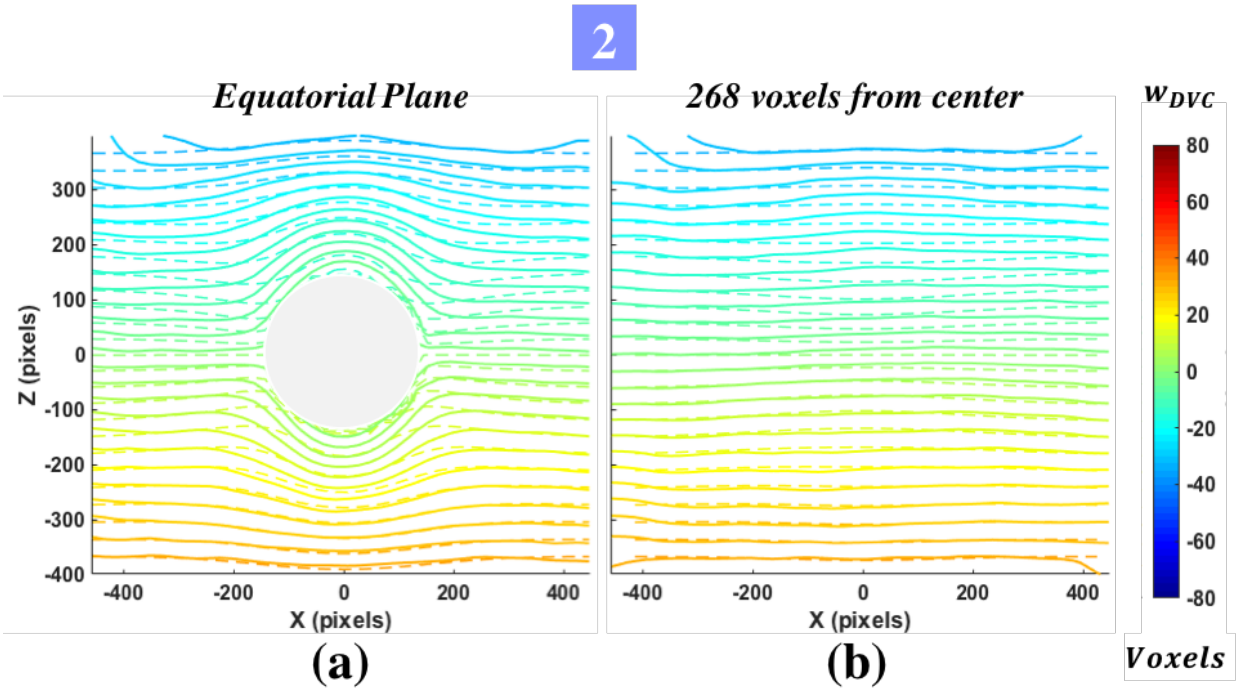

Figure 4.3 Comparison of raw additive w^{DVC} displacement fields (solid lines) for step 3 vs. the Goodier solution (dashed lines) at **(a)** the sphere center and **(b)** 268 voxels away from the sphere center.

Notice that as you get close to the sphere, the experimental results deviate more from the theoretical ones. This behavior was observed in prior work by (Gates et al. 2015), where a subset of 41^3 within the domain was used (as here) and the displacements better matched the theoretical contours when a smoothing scheme was applied to the entire displacement field (not done here). By implementing a global type of spline smoothing to the displacements the results can better match the theoretical. An alternative to improve the agreement near the sphere without additional smoothing is to use subset refinement to yield better results within the {*-2R*, *2R*} region. Subset refinement is a method in which smaller subset sizes are used in regions of high strain gradients, (i.e., near the sphere) and larger subsets are used away from regions, to reduce computation time. Results of subset refinement using 41^3 subsets far for the inclusion and 21^3 nearer the inclusion can be found in Gates et al. (2015). No subset refinement was done here.

4.2 Failure Response

The failure process that developed in the randomly distributed inclusions and irregular inclusion experiments were more complicated. In the randomly distributed inclusions, 20 debonded regions developed during failure (i.e., all inclusions debonded at some point during loading). Furthermore, the jagged surface features of the irregular inclusion created asymmetrical openings at failure. For simpler failure responses, as those occurring in the single and double inclusion experiments, the debonded regions were manually quantified using ImageJ, Excel and Amira. The complex failure responses were only qualitatively visualized using Amira.

4.2.1 Evolution of debonded region

To study the evolution of the opening/debonded region, ImageJ was used to measure the debond axial height in pixels, from the SI data sets in which failure occurred. Axial height is defined here as the opening in the horizontal plane visible in each of the extracted cross-sectional slices, as depicted in right plot of **Figure 4.4** with 4 small red regions. The left plots, is a schematic illustrating how the debond opening measurements were taken, starting at the inclusion's equatorial plane (right plot) and ending at the tip of the opening, in the direction of the loading axis, $\mathbf{z}$. The axial opening measurements, $\boldsymbol{\delta_a}$, along with the slice locations, $\boldsymbol{z_i}$ (where i = 0, 1, …, n; i = 0 is the equatorial plane and i = n is the tip of the opening), were recorded into an excel sheet. The slice locations were then normalized (by the amount slices that made up the inclusion) and then converted to arc lengths (yellow), $\boldsymbol{s}$. The axial height measurements of the opening (red) were converted from pixels to microns (μm) by using the spatial resolution of the scan.

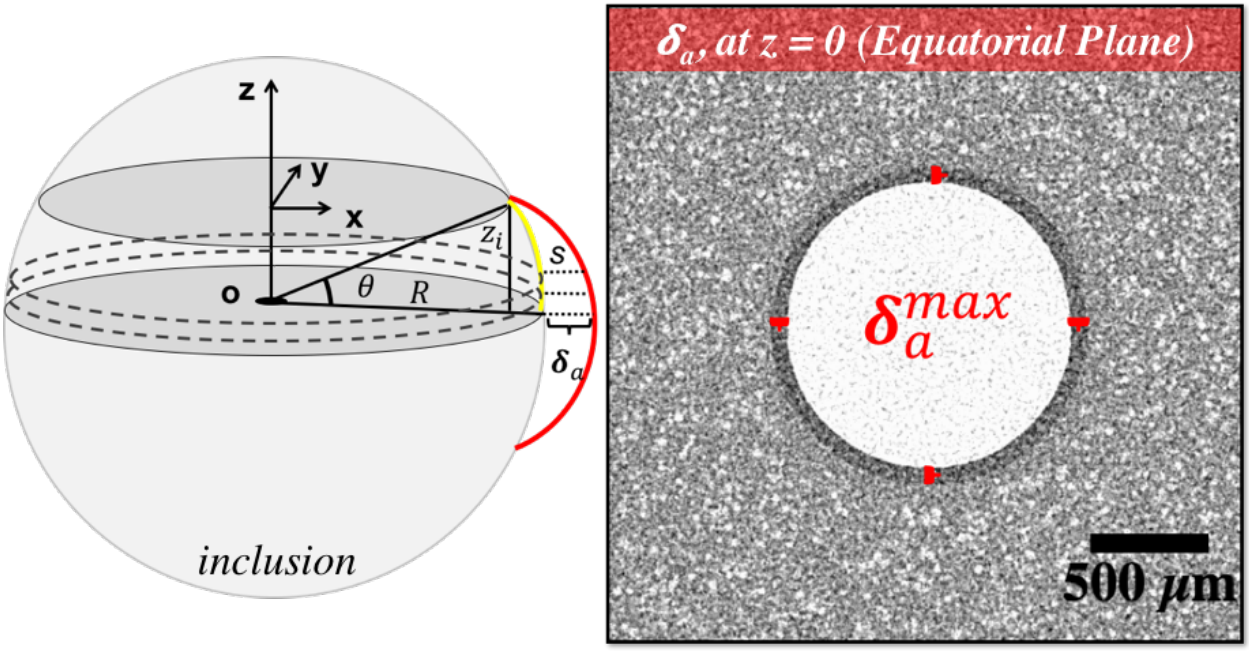

Figure 4.4 Schematic of axial height ($\boldsymbol{\delta_a}$) measurements of the debonded region in orange, starting at the normalized z slice ($\boldsymbol{z_i}$), to tip of the opening ($\boldsymbol{z_n}$) and arc length ($\boldsymbol{s}$) in yellow, relative to center of the spherical inclusion, **o**.

The scan resolutions of the single inclusion and single roughened inclusion experiments were 7.98 μm/pixel and 5.30 μm/pixel, respectively. In both experiments failure was first seen at 3.0 mm of compression, step 3 for single inclusion and step 6 for single roughened inclusion. Although failure was first observed at the same applied displacement despite roughening the inclusion, when the opening of the single smooth inclusion is compared to the evolution of the opening in the roughened inclusion, we see that roughening the inclusion did affect the debonding evolution, likely a result of the expected increase in interface toughness with increased roughness. **Figure 4.5**, illustrates the axial height of the opening along the circumference of the inclusion for the single smooth inclusion (blue) and single roughened inclusion (black) at various applied displacements.

Unfortunately, the evolution of the single inclusion opening was not captured as a function of load because only one scan was conducted at complete equatorial debonding. In

contrast the evolution of the single roughened inclusion was captured, since 3 scans were taken at complete debonding. Full equatorial debonding occurred at 3.5 mm (circle marker) and 3.75 mm (triangle marker) of cross head displacement, for the single roughen inclusion and single inclusion, respectively. At complete debonding, the tip of the opening, in the single inclusion at 3.75 mm, had traveled ~50% more along the circumference in contrast to the tip in the roughened inclusion at 3.5 mm. Hence, increasing the surface roughness by 60%, the growth of the opening was impeded though an increase in interfacial toughness.

The reduction of the opening is apparent throughout all the applied displacements during full equatorial debonding. At a maximum applied compression of 4.4 mm in the single roughened inclusion, the debonded region travelled less than the opening in the single inclusion, at 3.75 mm of compression. In addition, the growth of the single roughened inclusion opening along the circumference and perpendicular to the loading axis did not increase significantly, as shown in **Figure 4.5**. It is evident that overall, the opening in the single inclusion traveled more along the circumference of the inclusion. Again, the maximum deflection of the blue curve, which occurs at the equatorial plane ($s = 0$), is nearly equivalent to the maximum deflection in the single roughen inclusion at 4.4 mm of compression. The above signifies that the increase in surface roughness: (1) improved the shearing characteristics of the interface since the opening travelled less in the roughen inclusion, in all loading steps and (2) restricted the growth of the opening. The two-dimensional visualization of the openings of the SI and SIR are shown in Section 3.2.

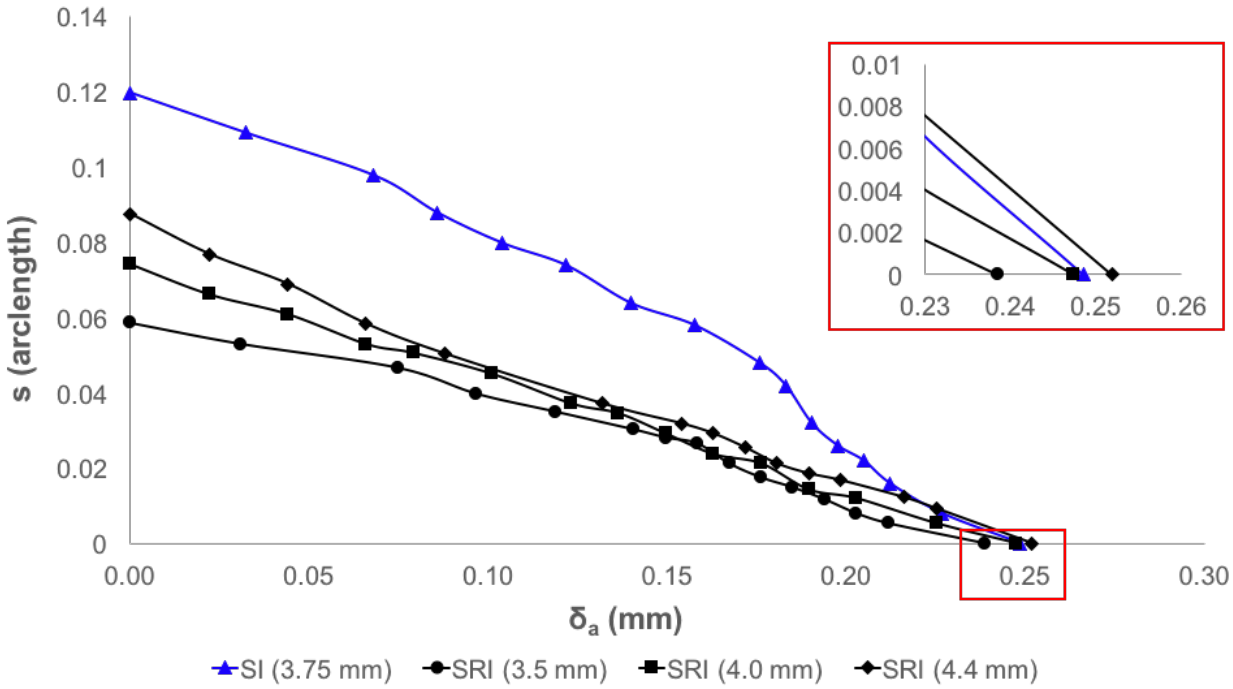

Figure 4.5 Axial height measurements, along the circumference of the inclusion, of single inclusion (SI, blue) and single roughened inclusion (SRI, black), at various applied compressions.

The scan resolution for the double inclusion was 5.26 μm/pixel. Both inclusions experience partial debonding at 3.0 mm of compression (step 5) and full equatorial failure at 3.5 mm of compression (step 6). Embedding two inclusions within the reinforced elastomer, resulted in a stiffer composite, compared to the composite with one inclusion. Similar to the single roughened inclusion, full equatorial debonding occurred at 3.5 mm. **Figure 4.6** illustrates the evolution of the opening, for both the top (dash curves) and bottom (solid curves) inclusion, at 3.5 mm (circle marker), 4.0 mm (square marker), and 4.3 mm (diamond marker) of compression. The red dashed curves convey that overall, the opening in the top inclusion traveled more along the circumference of the inclusion and perpendicular to the loading axis, when compared to the opening at the bottom inclusion, although the curves overall look similar. Comparing the bottom

inclusion (DIB) and top inclusion (DIT) curves to the single inclusion (blue curve in **Figure 4.6**), the maximum axial height was still larger in the single inclusion opening.

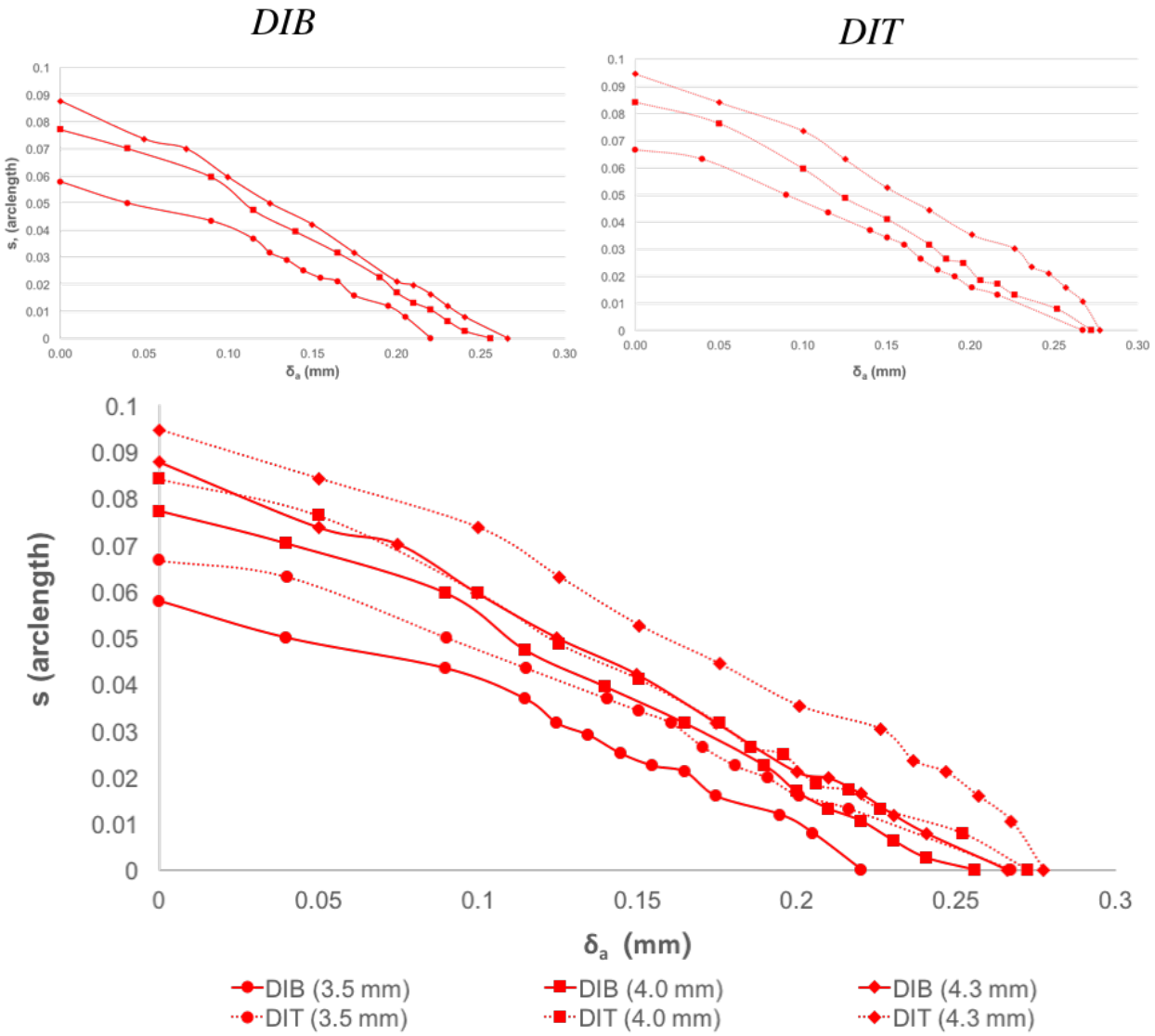

Figure 4.6 Axial height measurement of double inclusion for both the bottom inclusion in solid curves (DIB) and top inclusion in dashed curves (DIT).

The measurements of the opening during the single inclusion, single roughened inclusion and double inclusion experiments, were obtained manually using ImageJ, and provide a snapshot of the evolution of failure along a planar perspective (i.e., on a limited number of meridian planes only). By using Amira, a 3D perspective of the debonding over the entire single inclusion

at 3.75 mm of compression experiment was produced. Like in the case of the irregular meshed surface discussed in Section 3.1 a triangular 3D mesh was generated, but it was done using different segmentation tools. Within the Segmentation Editor, image segmentation tools, such as *magic wand* and *lasso*, were used to select (**Figure 4.7 (a)**) and create planar (2D) selections (**Figure 4.7 (b)**) of the debonded region, at every other slice above and below the equatorial plane until the debond tip was reached. The outside perimeter of opening was manually traced, using *lasso* with the *auto-trace* feature. Subsequently, the selected voxels were added to the material label. Next, the *magic wand* segmentation tool was used to first select the voxels within the inclusion and then subtract the voxels from the previous selection. The 2D segmented regions were then interpolated to create a 3D volume of the debonded region (**Figure 4.7(c)**). After processing the 3D volume (e.g. smoothing, removal of islands and fill holes), the construction of a triangular mesh (**Figure 4.7 (d)**) was done by attaching and applying a *SurfaceGen* module to label file. As before, the meshed surface was tested for flaws within the Properties window and fixed if necessary. Thus far, all the analysis and work presented of Amira, was done using Amira 5.1. The latter work, was performed using Amira 6 since it was capable of analyzing multiple surface relative to each other.

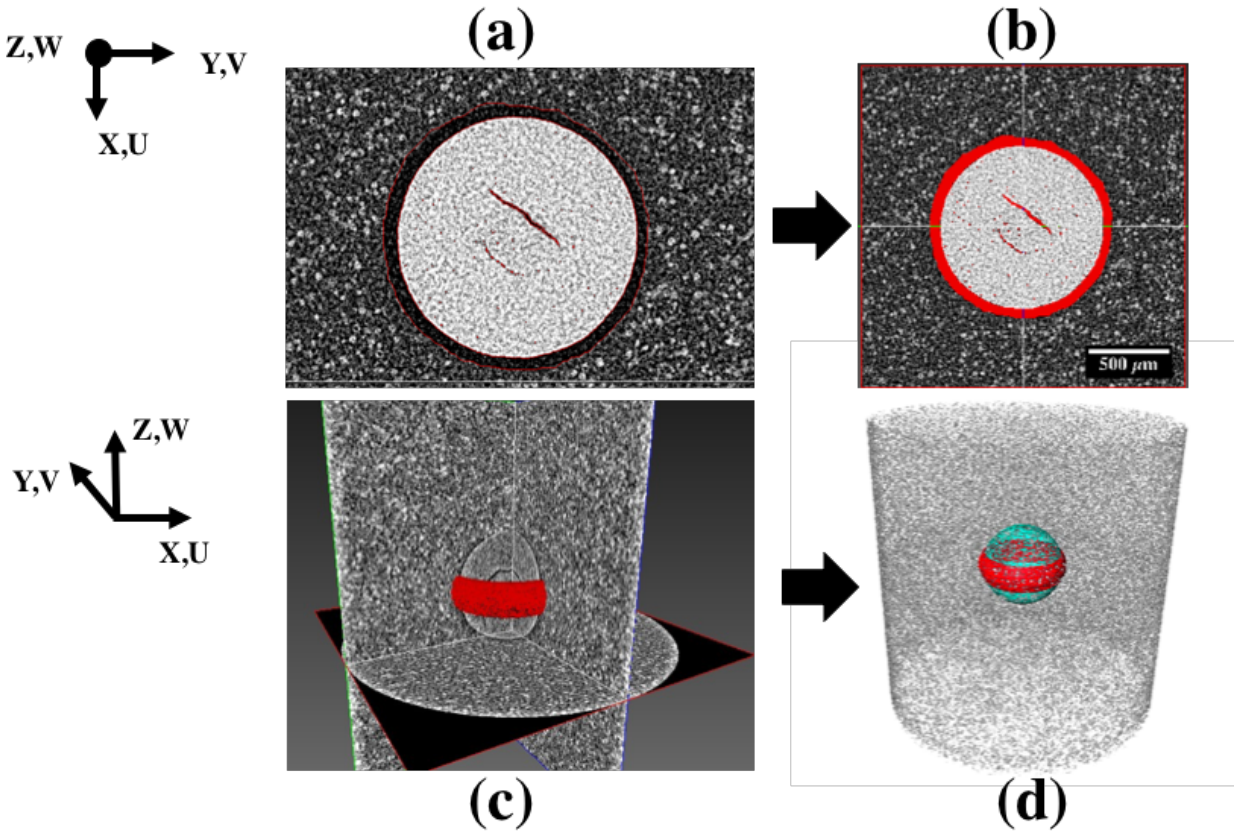

Figure 4.7 Image segmentation and mesh development procedure for a debonded region. Segmentation tools are used to select the debonded region **(a)**. 2D planar sections are developed **(b)** and then interpolated to obtain a 3D surface **(c)**. A triangular 3D mesh is extracted from the surface **(d)**.

Figure 4.7 (d) displays two distinct segmented surfaces, the alumina inclusion and the debonded region. The meshed cyan surface of an alumina inclusion was produced in the same manner as the irregular meshed inclusion surfaces, outlined in Section 3.1. Using Amira, a 3D *distance map* analysis was performed on the opening, relative to the surface of the meshed cyan surface. In other words, the deflection of the opening is measured normal to the surface of the segmented inclusion, as opposed to axially as was done manually in ImageJ. **Figure 4.8** illustrates the segmented surface of the inclusion (in red) and the debonded regions, which are color-coded relative to the distance of the voxel from the surface. The 3D distance map analysis

yielded a maximum deflection of ~136 μm, which is about 10 microns more than the manual measurement obtained through ImageJ (~120 μm). This 3D analysis on the single inclusion failure response becomes more taxing as the occurrences interfacial failure increases with the addition of further inclusions. For example, conducting a distance map analysis on one double inclusion data set would be extremely cumbersome since over 1000 image slices would have to be manually traced to generate the debonded regions in both inclusions. Therefore, experiments (randomly distributed inclusions, irregular inclusion and PDMS300I) with complex failure responses were only qualitative visualized.

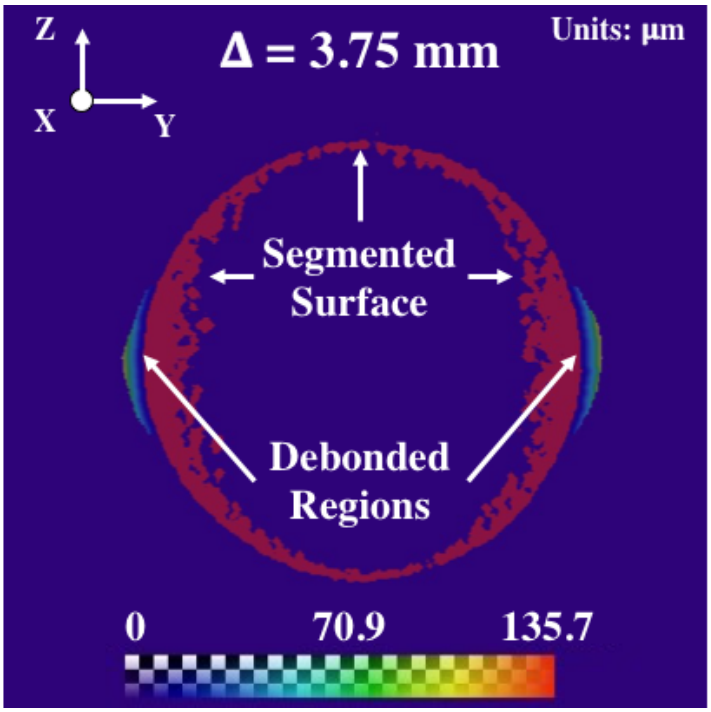

Figure 4.8 Distance map analysis, in Amira 6, of opening relative to the surface of the alumina inclusion (red). The maximum height of the debonded region was ~136 μm.

4.2.2 Visualization of Failure for More Complex Inclusion Geometries

To at least qualitatively visualize the more complicated failure responses, two 8-bit (0–255) images stacks (*.tif) (as oppose to an Amira file) of the same loading step were analyzed within the same Amira file. The visualization method is explained below using an RDI sample.

Again, two image stacks corresponding to the same scan, were uploaded to Amira using the same loading policy as before. One image stack was altered in ImageJ, its background was set to white (**Figure 4.9 (a)**), and was used to create a volume rendering of the debonded regions and the matrix. The background was changed from black to white, so that the debonded region can become visible after reversing the data range (255–0) of the volume rendering. Then, the original image stack (**Figure 4.9 (b)**) was used to create another volume rendering, containing only the inclusions. Finally, **Figure 4.9 (c)** depicts the combination of the two volume renderings for the randomly distributed inclusion experiment at 4.7 mm of compression. The procedure detailed above, can be applied to the irregular inclusion datasets to visualize the complexity of the opening.

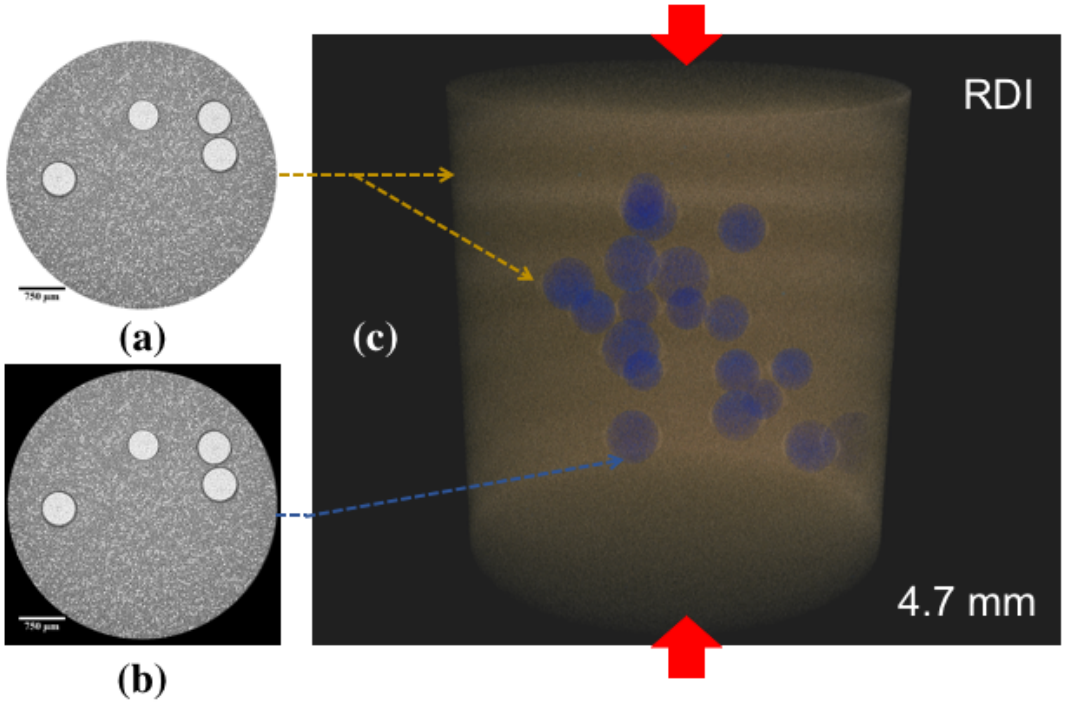

Figure 4.9 RDI debonded regions visualization in Amira 5 at 4.7 mm of compression. An altered image stack, with a white back ground **(a)**, creates a volume rendering of debonded regions and matrix. The original image stack **(b)** creates a volume rendering of the inclusions. Then both volume renderings are combined **(c)**.

CHAPTER 5: CONCLUSION AND RECOMMENDED FUTURE WORK

This work presented an experimental investigation of the internal deformation and failure response of model polymer particulate composites under a uniaxial applied compression. X-ray microCT imaging and digital volume correlation (DVC) were used in conjunction to qualitatively and quantitatively study deformation and the evolution of failure (interface debonding) in 3D. In-house algorithms were developed to preprocess the microCT data sets and create custom correlation grids for DVC. Amira was used to visualize and extract data from the CT scans. Image segmentation was performed to generate meshed surfaces, which were either used to create complex custom correlation grids or to analyze the failure response and quantify the debonded region. The DVC measurement technique enabled the computation of three-dimensional strain fields surrounding the inclusion(s) within the composite material under loading.

The conclusions of this work are discussed below in two sections. The first section covers the DVC measured deformations (Chapter 3) and a quantitative/qualitative perspective on the evolution of failure (Chapter 4). The second section covers recent work accomplished with suggestions for future work in this field.

5.1 INTERNAL DEFORMATION AND FAILURE RESPONSE FOR DIFFERENT MICROSTRUCTURE CONFIGURATIONS

The overarching goal of this work was to quantitatively measure and qualitatively study the evolution of 3D deformation and failure in model polymer composite materials with a highly-controlled microstructure. The first objective of this work was to determine the 3D displacement and strain fields induced by an externally applied load. This was accomplished by employing 3D

X-ray microCT imaging of in-house manufactured model composites loaded by an *in-situ* compression stage at a constant displacement rate of 0.5 mm/min, and using DVC to process the resulting CT scans. The internal displacement and strain fields were studied for a series of different well-controlled microstructure configurations: single inclusion (SI), double inclusion (DI), small number of randomly distribution of inclusions (RDI), rounded irregular inclusion (RII) and vertical irregular inclusion (VII). The second objective was to study the evolution of failure in 3D. For simple microstructures, such as those in the SI and DI samples, interface debonding was resolved both qualitatively and quantitatively. The more complex failure modes of samples such the RDI, RII and VII, were only qualitative analyzed and visualized. The generated failure responses are directly related to the complexity of the microstructure, either depending on the number of reinforcing particles (e.g., RDI) or the irregular shape of the particles (e.g., RII and VII). Data sets were manipulated within ImageJ and then analyzed in Amira to produce volume renderings of the complex failure response (Section 4.2).

The first objective of this work integrated the use of the DVC technique with X-ray microCT to develop 3D interior strain and displacement measurements (Section 3.2). The objective there was to experimentally resolve the accuracy of the DVC technique and demonstrate the strain development resulting in different microstructural configurations and by different applied loads. From this work, it is concluded that:

i. Deformation around a single inclusion in a polymer composite was studied and yielded displacement errors less than 4% of elastic theory in regions greater than $2R$ (R, sphere radius) and less than 10% error when nearer the sphere. Interfacial failure arose after about ~17% nominal applied strain for the as-received alumina inclusion

in the PDMS matrix. Resultant strain fields of partial and complete debonding were captured showing 40% strain concentration surrounding the inclusion

ii. Increasing the surface roughness of a spherical alumina inclusion did not significantly alter the displacement or strain fields developed throughout the polymer composite. However, as expected, interfacial debonding occurred at a higher load level, namely after ~20% applied strain. Note, however, that we did not perform a sufficient number of experiments to definitively statistically establish through the microCT scans that the roughened inclusion debonded at a load higher than that for the single inclusion. Since the SI could have debonded at some applied displacement between 2.5 mm and 3.0 mm (like the roughened inclusion) and not between 2.25 mm and 2.5 mm of compression. More experiments would be needed to conclusively establish this fact, which however is expected since an increased roughness would increase interfacial strength.

iii. Particle interactions were studied relative to two precisely positioned inclusions (manufactured using the procedure outlined in Chapter 2). At lower applied loading levels, the elastic strain response of both inclusions, bottom (DIB) and top (DIT), is essentially the superposition two SI elastic response. At ~10% nominal applied strain, step 3, the strain concentrations above and below each inclusion interacted with each other producing a more complex strain field in the ligament between the two inclusions. Note that at this stage the distance between the spheres, which started out at 2.7 mm (or ~6*R*), had decreased to 1.9 mm or 4*R*. Partial debonding arose, at both inclusions, sometime after ~12% nominal applied strain. At partial debonding, a large region with a strain concentration of ~17% developed between the two inclusions.

The strain concentration between DIB and DIT increased to ~30% at complete debonding.

iv. A more complicated microstructure of 20 particles randomly positioned within the matrix was also investigated. The sample with randomly distributed inclusions (RDI) was cured using a different method than the DI and SI samples. As a result, the stiffness of the RDI sample cannot be compared with that of the SI and DI samples. The measured 3D displacements fields in the RDI sample are quite detailed, both in the form of a quiver plot or as volumetric contour slices. Yet, they do not illustrate clearly how the multiple particles interact since it is more difficult to obtain DVC measurements between particles. The strain field measured in the RDI experiment showed similar strain concentrations to that developed during the elastic response of the SI and DI samples. In step 3 of this experiment (**Figure 3.21**), higher strain concentrations above and below the inclusions arose which developed into a concentration of ~20% by step 5. Interfacial failure did not occur around all 20 inclusion at once. Failure first arose at 2.5 mm of compression (step 4) in the area between the 9^{th} and 10^{th} inclusion in the interior of the sample, these two being the only inclusions that were in contact. By step 9, the interacting strain concentrations accumulated from 35% to 45% strain with a maximum of 50% occurring at the top and bottom of the inclusions.

v. DVC was also applied to polymer composites with irregularly shaped inclusions. Amira was used to create a detailed three-dimensional meshed surface of the inclusion, which was then used to help create a non-uniform correlation grid for DVC. Incremental displacement and strain fields for RII and VII were obtained.

Further work is needed to entirely remove both rigid translation and rotation, by aligning precisely the shape of the particle (assumed rigid since it is so much stiffer than the matrix) among all data sets for the correlations to yield proper results. The next section discusses potential ideas for this alignment in 3D space. However, in principle it is an efficient and easy way to eliminate rigid body motion from the DVC results.

The second objective of the work quantitatively analyzed evolution of the failure that occurred at the particle/matrix interface for different microstructural configurations. The following observations can be concluded:

i. SI interfacial failure developed after 2.25 mm of applied displacement, or ~17% nominal applied strain. Full (all around) equatorial debonding occurred by 3.75 mm of compression. By analyzing the cross-sectional CT slices, in ImageJ and Excel (Section 4.1) it was determined that a maximum interfacial opening ~120 μm occurred at the equator plane. However, a distance map analysis (conducted in Amira 6) of the debonded region, relative to the surface of the inclusion, i.e., measurements normal to the inclusion, yielded a maximum deflection of ~136 μm. Unfortunately, the evolution of interfacial failure was not captured here as only one scan was conducted at complete debonding.

ii. SRI interfacial failure in the roughened inclusion case arose after ~20% applied strain. Here the evolution of the debonded region was better captured since 3 scans were performed after full equatorial debonding. Despite being compressed 0.65 mm more than the SI case, the opening in SRI travelled less along the surface of the sphere, in contrast to the SI sample which had debonded to a larger latitude for

smaller load. This shows an increased strength of the particle/matrix interface for the roughened case.

iii. Embedding two inclusions within the reinforced elastomer, resulted in two distinct debondings, without any cracking between inclusions being observed. Like the SRI case, full equatorial debonding occurred at about 3.5 mm of compression. The debonding in the top inclusion propagated more along the circumference of the inclusion and perpendicular to the loading axis, when compared to the opening at the bottom inclusion. The single inclusion debonding was larger in magnitude than both the bottom inclusion (DIB) and top inclusion (DIT) by ~33% and ~21%, respectively.

5.2 SUGGESTED FUTURE WORK BASED ON PRELIMINARY EXPERIMENTATION

The resultant internal deformations from a complex microstructure (such as that in RDI, RII, and VII) were illustrated in Chapter 3. Although, the 3D measurements were quite detailed, the correlations conducted on the RDI sample only removed the nodal points within the (selected) origin inclusion; similar to what was done in the SI correlation grid. Nonetheless, DVC was still able to map the deformations between the undeformed and deformed data sets, despite us not having removing the nodal (correlation) points within the remaining inclusions. It is preferable that incremental correlations should be conducted with a new correlation grid based on a meshed surface of the 20 alumina inclusions. Like the correlation grids from the irregular inclusion (Section 3.1), the vertices of the triangular elements are used to generate the new correlation grid. With the new correlation grid, the effect of removing the nodal correlation points, within all 20 inclusions, could be investigated. Another idea to explore is, whether it is necessary to remove the nodal points within the microstructure in both undeformed and deformed configurations (like in DI correlation grids), vs. only the deformed one. This could be

investigated using the DI experiment. The double inclusion data sets could be correlated with correlation grids that do or do not contain the nodal points in the deformed state. Furthermore, for large particle volume fractions, the deformations become more complicated. As a result, conducting using quadratic shape function, as oppose to linear shape functions, may diminish the observed artifacts measured by DVC. Exploring these various ways of determining the correlation grid becomes increasingly important as the reinforcement volume fraction increases. For larger particle volume fractions, less marker particles are available to perform the correlation, making DVC increasingly more difficult for large volume fraction composites. The techniques suggested here may help alleviate this issue (to a certain extent).

Chapter 3 illustrated preliminary incremental correlations of an irregularly shaped microstructure. To increase the percentage of converged correlation points (with a suitable c-target value, typically 0.05 or 0.1), Amira should be utilized to approximate the geometric affine transformation needed to align the deformed data set to the undeformed data set as best as possible, and in the process, remove rigid body motion (assuming a rigid particle). Within Amira, an *AlignSurfaces* module can be used to align two similar meshed surfaces. The applied transformation can be viewed in the Dialog window, within the Transformation Editor. The estimated transformation can then be interpreted and imported into MATLAB, to apply an affine transformation to the deformed data set. The RDI data sets can be used to validate/troubleshoot the 3D alignment technique, which aligns deformed data sets relative meshed microstructure features.

Lastly, to induce different failure mechanisms, such as matrix tearing or particle failure, different types of inclusion or matrices could be investigated. For example, to generate particle failure a more brittle inclusion, such as macro-size salt particles, could be embedded within a

reinforced elastomer, using the "cutting and placing" technique detailed in Chapter 2. Alternatively, a matrix more brittle than PDMS could be used, e.g. a geopolymer (Kriven et al. 2007), to induce matrix, rather than particle, cracking.

REFERENCES

Bay BK, Smith TS, Fyhrie DP, Saad M, "Digital volume correlation: three-dimensional strain mapping using X-ray tomography", Exp Mech, Vol. 39, pp 217–226, 1999.

Bay, B.K., *Methods and applications of digital volume correlation*. The Journal of Strain Analysis for Engineering Design, 2008. 43(8): p. 745-760.

Benoit, A., S. Guerard, B. Gillet, G. Guillot, F. Hild, D. Mitton, J.N. Perie, and S. Roux, 3D analysis from micro-MRI during in situ compression on cancellous bone. J Biomech, 2009. 42(14): p. 2381-6.

Buffiere, J.Y., E. Maire, J. Adrien, J.P. Masse, and E. Boller, *In Situ Experiments with X ray Tomography: an Attractive Tool for Experimental Mechanics*. Experimental Mechanics, 2010. 50(3): p. 289-305.

Choi,K and J. Rogers, *A Photocurable Polyd(dimethysiloxane) Chemistry Designed for Soft Lithographic Molding and Printing in the Nanometer Regime*. Journal of American Chemical Society 2003. 125(14):p. 4060-4061.

Feldkamp, L.A., L.C. Davis, and J.W. Kress, *Practical cone-beam algorithm*. J. Optical Society of America, 1984. 1(6): p. 612-619

Forsberg, F. and C.R. Siviour, 3D deformation and strain analysis in compacted sugar using x-ray microtomography and digital volume correlation. Measurement Science and Technology, 2009. 20(9): p. 095703.

Forsberg, F., M. Sjodahl, R. Mooser, E. Hack, and P. Wyss*, Full three-dimensional strain measurements on wood exposed to three-point bending: Analysis by use of digital volume correlation applied to synchrotron radiation micro-computed tomography image data*. Strain, 2010. 46: p. 47-60.

Franck C, Hong S, Maskarinec S, Tirrell D, Ravichandran G, *Three-dimensional full-field measurements of large deformations in soft materials using confocal microscopy and digital volume correlation*, Exp Mech, Vol. 47, pp. 427–438, 2007.

Garcia, D., *Robust smoothing of gridded data in one and higher dimensions with missing values*. Computational Statistics & Data Analysis, 2010. 54(4): p. 1167-1178.

Gates M., Gonzalez J., Lambros J. and Heath M.T. (2015), "Subset Refinement for Digital Volume Correlation: Numerical and Experimental Applications", Experimental Mechanics, (2015) Vol. 55, pp. 245–259, doi: 10.1007/s11340-014- 9881-3.

Gates M., Heath M.T. and Lambros J. (2015), *High Performance Hybrid CPU and GPU Parallel Algorithm for Digital Volume Correlation*, International Journal of High Performance Computing Applications, Vol. 29, No. 1, pp. 92-106, doi: 10.1177/1094342013518807.

Gates, M., *High Performance Digital Volume Correlation*. PhD Thesis, 2011.

Gates, M., J. Lambros, and M.T. Heath, *Towards High Performance Digital Volume Correlation*. Experimental Mechanics, 2010. 51(4): p. 491-507.

Germaneau, A., P. Doumalin, and J.-C. Dupré, Comparison between X-ray micro-computed tomography and optical scanning tomography for full 3D strain measurement by digital

volume correlation. NDT & E International, 2008. 41(6): p. 407-415.

Germaneau, A., P. Doumalin, and J.C. Dupre, *3D Strain Field Measurement by Correlation of Volume Images Using Scattered Light: Recording of Images and Choice of Marks*. Strain, 2007. 43: p. 207-218.

Gonzalez J. and Lambros J. (2016), *A parametric study on the influence of internal speckle patterning for digital volume correlation in x-ray tomography applications*, Experimental Techniques, Vol. 40, No. 5, pp. 1447–1459, doi:10.1007/s40799-016- 0145-2.

Goodier, J.N., *Concentration of stress around spherical and cylindrical inclusions and flaws*. Journal of Applied Mechanics 1933. 55(7): p. 39-44.

H.A. Bruck, S.R. McNeill, M.A. Sutton, W.H. Peters III, *Digital Image Correlation Using Newton-Rapson Method of Partial Differential Correction*, Experimental Mechanics, Vol 29, No 3 September 1989.

Hild, F., S. Roux, D. Bernard, G. Hauss, and M. Rebai, *On the use of 3D images and 3D displacement measurements for the analysis of damage mechanisms in concrete-like materials*. VIII International Conference on Fracture Mechanics of Concrete and Concrete Structures, 2013.

Jiroušek, O., I. Jandejsek, and D. Vavřík, Evaluation of strain field in microstructures using micro-CT and digital volume correlation. Journal of Instrumentation, 2011. 6(01): p. C01039-C01039.

Lenoir N, Bornert M, Desrues J, Bésuelle P, Viggiani G, "*Volumetric digital image correlation applied to X-ray microtomography images from triaxial compression tests on argillaceous rock*", Strain, Vol. 43, pp.193–205, 2007.

Limodin, N., J. Réthoré, J. Adrien, J.Y. Buffière, F. Hild, and S. Roux, *Analysis and Artifact Correction for Volume Correlation Measurements Using Tomographic Images from a Laboratory X-ray Source*. Experimental Mechanics, 2010. 51(6): p. 959-970.

Limodin, N., J. Réthoré, J. Adrien, J.Y. Buffière, F. Hild, and S. Roux, Analysis and Artifact Correction for Volume Correlation Measurements Using Tomographic Images from a Laboratory X-ray Source. Experimental Mechanics, 2010. 51(6): p. 959-970.

Liu L, Morgan EF, *Accuracy and precision of digital volume correlation in quantifying displacements and strains in trabecular bone*, J Biomech, Vol. 40, pp. 3516–3520, 2007.

Lotters, J.C W. Oithius, P.H Veltink, and P. Bergveld, The mechanical porperties of the rubber elastic polymer polydimethysiloxane for sensor applications. Journal of Micromechanics and Microengineering, 1997. 7:p 145-147.

Patil S and Ravi B. Voxel-based representation, display and thickness analysis of intricate shapes. Ninth International Conference on Computer Aided Design and Computer Graphics (CAD/CG 2005)

Roux S, Hild F, Viot P, Bernard D, *Three-dimensional image correlation from X-ray computed tomography of solid foam*, Composites Part A, Vol. 39, pp. 1253–1265, 2008.

Sutton, M.A., J.-J. Orteu, and H. Schreir, *Image Correlation for Shape, Motion and*

Deformation Measurements: Basic Concepts, Theory and Applications. 2009: Springer

Sutton, M.A., W.J. Wolters, W.H. Peters III, W.F. Ranson, and S.R. McNeill, *Determination of displacements using an improved digital image correlation method*. Image and Vision Computing, 1983. 1(3): p. 133-139.

T.C. Chu , W.F. Ranson, M.A. Sutton, W.H Peters, *Application of Digital Image-Correlation Techniques to Experimental Mechanics*, Experimental Mechanics, Vol 25, No 3, September 1985.

Verhulp, E., B. van Rietbergen, and R. Huiskes, *A three-dimensional digital image correlation technique for strain measurements in microstructures*. J Biomech, 2004.

W. M. Kriven, J. L. Bell, S. W. Mallicoat and M. Gordon, contributed chapter to Proc. of Int. Worshop on Geopolymer Binders-Interdependence of Composition, *Intrinsic Microstructure and Properties of Metakaolin-Based Geoolymers*. Structure and Properties, Weimar, Germany, 71-86, 2007.

Zauel, R., *Comparison of the Linear Finite Element Prediction of Deformation and Strain of Human Cancellous Bone to 3D Digital Volume Correlation Measurements*. Journal of Biomechanical Engineering, 2005. 128(1): p. 1.